




# A review of piezoelectric materials for nanogenerator applications

Srujan Sapkal<sup>1</sup>, Balasubramanian Kandasubramanian<sup>2</sup>, and Himanshu Sekhar Panda<sup>1,\*</sup> 

<sup>1</sup>Sustainable Energy Laboratory, Department of Metallurgical and Materials Engineering, Defence Institute of Advanced Technology, Pune 411025, India

<sup>2</sup>Structural Composite Fabrication Laboratory, Department of Metallurgical and Materials Engineering, Defence Institute of Advanced Technology, Pune 411025, India

**Received:** 18 August 2022

**Accepted:** 12 October 2022

**Published online:**  
11 November 2022

© The Author(s), under exclusive licence to Springer Science+Business Media, LLC, part of Springer Nature 2022

## ABSTRACT

The invention of flexible piezoelectric nanogenerators in today's nanotechnology era attracted the attention of researchers on nano-energy harvesting systems. Since then, extensive research has been ongoing in piezoelectric composites for energy generation because of their potential to replace conventional energy sources. The latest advances in synthetic materials enhanced the piezoelectric properties of composites and proved their potential to become self-sustainable nanotechnology for green energy applications. In this review, a brief introduction to the field of piezoelectricity is provided, followed by a thorough analysis of the novel advances in materials, namely polymers, ceramics, and composites, with their synthesis and fabrication technologies. Finally, the state-of-the-art uses of these materials in self-charging, implantable, and wearable devices as nanogenerators are extensively discussed.

## 1 Introduction

Curie brothers discovered the piezoelectricity phenomenon by observing the electric charge generation in piezoelectric materials at specific locations when subjected to mechanical stress [1]. In today's era of the global energy crisis, piezoelectric materials provide an alternative solution as a renewable source for energy harvesting. Piezoelectric transduction is a promising energy generation technology when compared with triboelectric, pyroelectric, and other transduction mechanisms owing to its massive

electromechanical conversion constant [2]. In 2001, Glynne-Jones and team [3] proposed a "mechanical vibrations-powered microgenerator", and then in 2006, Wang and Song [4] manufactured the zinc oxide (ZnO)-based nanogenerator, which created a significant impact on the piezoelectric community. Piezoelectric nanogenerators gained a vital position in the energy sector because of their superiority over conventional energy technologies. Among non-renewable energy sources, batteries perform an essential role as a power supply component but using them in electronic devices can be cost-inefficient

Address correspondence to E-mail: himanshusp@diat.ac.in

because of replacement, maintenance, and other issues such as charging and short life span. Due to the drawbacks of conventional energy devices, substantial efforts are going into the development of piezoelectric nanogenerators as self-sustainable power sources for electronic devices. Piezoelectric generators are more reliable, resistant to harsh environmental conditions, perceptive to minor strains, and manufactured in small structures, unlike conventional batteries. Also, it is profitable to harvest mechanical energy in the surroundings as a power source because of its easy availability and the better and longer performance of electronic devices [5]. Piezoelectric nanogenerators can also operate on *in vivo* mechanical energies, such as heartbeat, muscle stretching, and lung motion, to empower sensors for heart monitoring, hearing aids, and other biomedical devices [6].

In the course of time, new energy harvesting strategies have been proposed, such as triboelectric, pyroelectric, thermoelectric, and piezoelectric [2]. The piezoelectric energy harvesting mechanism is broadly accepted because of the abundance of mechanical energy and the direct utilization of piezomaterials to transform mechanical stimulus into electrical energy. Active piezoelectric materials possess unique properties that allow them to have uses, such as energy harvesters, actuators, and sensors [6, 7]. The multifunctionality of piezoelectric materials varies according to their physical and chemical characteristics, for instance, flexibility, morphology, brittleness, synthesis technique, and elemental composition.

Over the past few years, different synthetic piezoelectric materials like composites, ceramics and polymers, single crystals, and bio-inspired materials were investigated to enhance the piezoelectric performance of devices with their unique advantages. In ceramics, prominent piezoelectric examples include lead zirconate titanate (PZT), barium titanate (BT), ZnO, potassium sodium niobate (KNN), and barium titanate–bismuth ferrite (BT–BF) [5, 7, 8]. PZT is advantageous in the piezoelectric area among these well-known materials because of its high-performance values. Different morphologies of the polycrystalline materials like rods, particles, flakes, and sheets were synthesized for enhancing the piezoelectric performance [9, 10]. For polymers, there are several choices such as polyvinylidene difluoride (PVDF), polymethyl methacrylate (PMMA),

polydimethylsiloxane (PDMS), and nylon 11 (PA11); they showcase remarkable piezoelectric properties upon electric poling treatment which facilitates the dipole alignment inside the polymer [11]. Among these polymer materials, PVDF offers the best piezoelectric performance because of its inherent dipole moment; as a result, PVDF and its co-polymers have been extensively analysed in the energy harvesting sector because of their high crystallinity, and all-trans dipole inherited existing  $\beta$ -phase [11–13]. Numerous experimentally realizable and successful combinations of ceramic fillers with polymers have attracted the academic world's attention towards the realization of piezo-composites to harness the power and advantages of both ceramics and polymers. Composites have exciting properties like flexibility, lightweight, stretchability, biocompatibility, and possess an extensive range of applicability in the piezoelectric nanogenerator domain. The flowchart of the different stages essential for nanogenerators and their applications can be visualized in Fig. 1 [7].

The mechanism of piezoelectricity is based on the asymmetric shift of electrical charges in the material when exposed to external mechanical stress, as shown in Fig. 2 [11]. As non-centrosymmetry is crucial for piezoelectricity, analysis of crystal symmetry is vital while considering the enhancement in the piezoelectric performance of the crystalline materials. Perovskite materials (BT, KNN, PZT) show ferroelectric behaviour and non-cubic crystal structures at operational temperatures, which is highly desirable for piezoelectric applications. Direct and converse piezoelectric effects arise in piezoelectric crystals mainly due to the above-mentioned crystalline asymmetry. The direct piezoelectric effect is the generation of electric polarization when a material is subjected to mechanical stress. In contrast, if the potential is applied across a material, it results in an induced strain and is termed as the converse piezoelectric effect. Direct and converse effects are essential in industrial applications; pressure sensors and nanogenerators are based on direct effect, whereas actuators are founded on the converse effect. These materials usually attribute a polar axis. The direction along which the mechanical stimulus was exerted on the material with reference to the polar axis, influences the piezoelectric functioning and output of the material. The constitutive equations which explain the piezoelectric phenomenon are given as follows:

**Fig. 1** The visual flow of domains comprising the piezoelectric energy harvesters

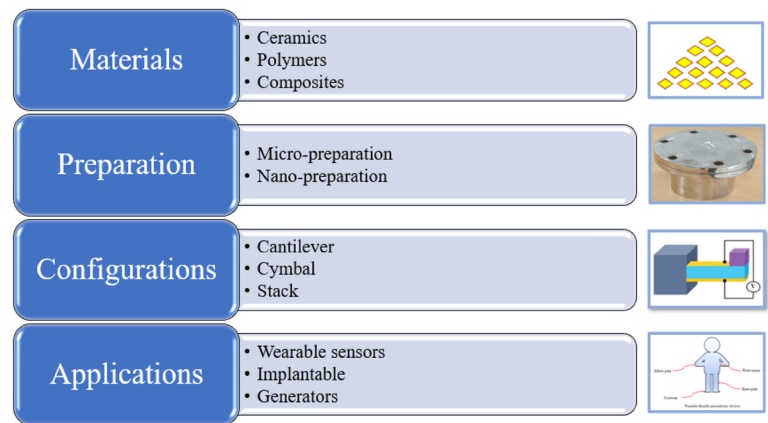
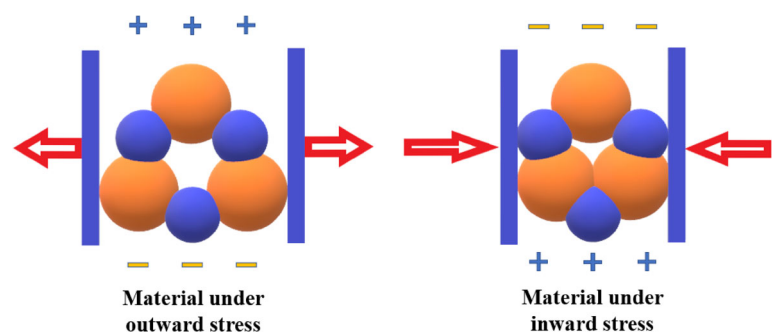


**Fig. 2** Breaking of charge symmetry in a crystal when outward and inward mechanical force is applied, giving rise to electric polarization



$$D = dT + \epsilon E \tag{1}$$

$$X = sT + dE \tag{2}$$

where  $E$  is the electric field,  $D$  is electric displacement,  $\epsilon$  is the permittivity of the material,  $d$  is the piezoelectric constant,  $s$  is mechanical compliance,  $T$  is stress, and  $X$  is strain. Equation (1) represents the direct effect, and Eq. (2) converse effect.

As discussed, piezoelectric materials are essential in several technological fields and are pivotal in the energy sector as self-sustainable devices because of recent developments in materials and manufacturing methods [14, 15]. The number of published journal articles in the piezoelectric area drastically increased from 1 to 1172 from 2000 to 2019, based on device fabrication, applications, and material properties [5]. The present article will extensively review the available piezoelectric materials and their application as nanogenerators. The aim is to concentrate on the aspects such as available materials, material properties, physics of the piezoelectric mechanism, factors affecting the performance of nanogenerators, applications of nanogenerators, performance enhancement, and fabrication techniques. Also, it comprised the detail analysis of recent advances in materials,

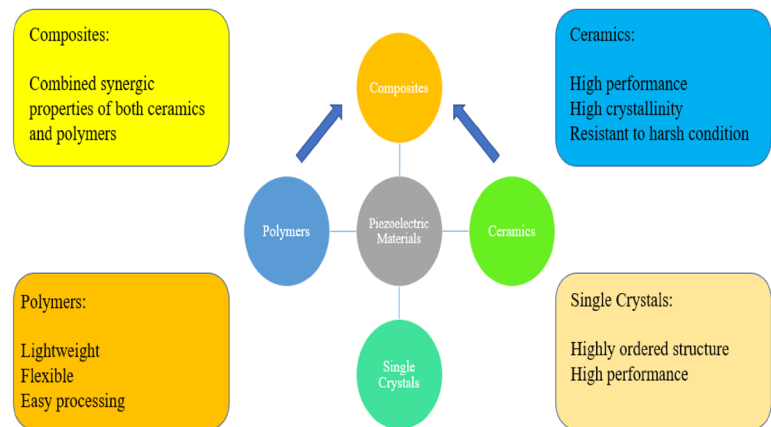
including ceramics, polymers, and composites, with their advantages and disadvantages. More emphasis is provided on recently developed composites because of their novel and exciting properties, including a broad range of applications in the harvesting area. Finally, it covers existing nanogenerator applications of piezoelectric materials with their working principle and properties.

## 2 Types of materials

Conversion of externally induced mechanical strain into electrical surface polarization is an inherent property of piezoelectric materials. The performance of a material critically depends upon its types [2], in particular polymers, ceramics, single crystals, and polymer–ceramic composites (Fig. 3). Since there is an alarming requirement for self-sustainable energy sources, extensive work is ongoing in the piezoelectric materials to achieve potential solutions.

The selection of piezoelectric materials is based on the electromechanical conversion factor, piezoelectric coefficient, dielectric constants, Curie temperature, and crystal structure [2]. Among piezoelectric materials, ceramics are the most promising ones because

**Fig. 3** Synthetic materials available for piezoelectric applications with their unique characteristics and advantages



of the enormous value of piezoelectric constant ( $d_{33}$ ) and observed ferroelectricity with high Curie temperature ( $T_C$ ), but possess disadvantages such as brittle nature and heavy weight. Polymers have low piezoelectric performance and electromechanical coupling factor, but they are potential candidates in the flexible piezoelectric material industry because of their lightweight, flexibility and low cost. To conquer the drawbacks of both ceramics and polymers, piezo-composites were explored, which retain the advantages of both ceramics and polymers and hold great potential in the energy harvesting sector.

## 2.1 Piezoceramics

After the discovery of natural materials such as quartz, many synthetic ones were prepared, exhibiting outstanding piezoelectric properties relative to natural crystals. Piezoelectric ceramics are polycrystalline in nature and have potential applications in mechanical energy harvesting [7]. As discussed, electric poling is essential to align the existing dipoles in the material with proper orientation to obtain the induced piezoelectric properties in ferroelectric ceramic candidates [2, 7]. Among ceramics, synthetic piezoelectric ceramics are famous for their better electromechanical conversion, huge dielectric constant, massive  $d_{33}$  value, and high Curie temperature. Although they have excellent properties, their brittleness limits their piezoelectric performance because they cannot absorb large strains without getting damaged [2]. Among ceramics, perovskite and wurtzite-structured materials are of prime importance for piezoelectric energy harvesting applications because of their well-established non-centrosymmetric properties [5]. Synthetic materials with high

piezoelectric performance, like PZT, BT, and KNN, show perovskite structure with high performance, whereas ZnO exhibits a wurtzite structure with comparatively low piezoelectric performance [5]. Asymmetry along the 'c' direction in perovskite crystal structures induces the necessary non-centrosymmetry in the material, which instigates the essential requirements for higher piezoelectric performance. Perovskite materials have considerable importance in smart applications since they showcase various novel effects such as piezoelectric effect, electrostriction, domain switching, and volume change because of electric field-induced strain [5, 16]. Consequently, it is crucial to emphasize their (metal oxides) synthesis techniques for completeness purposes. Some of the conventional techniques are quite popular within the research community because of their unique advantages as listed below [1]:

- (a) Solid-state reaction: This procedure is widely used to prepare ferroelectric (FE) oxides with the best piezoelectric and dielectric properties. Solid-state synthesis is an irreversible process where powder compacts are fused into a single compound (dense polycrystalline ceramic) with the help of thermal energy created during the milling process [17]. The decrease in the interfacial free energy in an ensemble of particles with respect to a collection of distinct particles is the main driving force behind the solid-state reaction. Major studies with the KNN, BT–BF, and other ceramics were performed with solid-state synthesis because the resulting high density drastically increases the piezoelectric functioning and material characteristics such as dielectric properties [18, 19].

- (b) Sol–gel synthesis: This technique is a template procedure for developing nanostructures in which piezoelectric material synthesis within the other solid's nanopores is carried out [17]. In this method, a hydrolysis reaction is performed to get the suspension of colloidal particles (sol) followed by the condensation of the molecular precursors, and templating is used to provide a nanostructured morphology to the material [17]. The two main advantages of this method are producing materials with better purity at low-temperature values and the facile preparation of a uniform, multi-element system by simply blending precursor chemicals [17, 20].
- (c) Hydrothermal synthesis: Hydrothermal synthesis is a cost-effective solvent-based technique used to synthesize piezoelectric polycrystalline ceramic with advantages like controllable microstructures, low-temperature requirement, and substrate independency. Hydrothermal synthesis is widely used for ceramic synthesis because it is a facile method for modifications like elemental doping and morphology control of the material [20].

### 2.1.1 Lead-based piezoceramics

The invention of PZT in the 1950s can be considered a paradigm-shifting moment in the energy harvesting research field because it is the most extensively utilized and exploited material in the mechanical energy harvesting area [21]. PZT outperforms all piezoceramics because of large dielectric and ferroelectric properties with high-performance coefficients such as electromechanical conversion factor and piezoelectric constant [22]. Detailed analysis of the PZT system revealed the vital phenomenon of morphotropic phase boundary (MPB) in the perovskite ferroelectric materials domain, which primarily contributes to enhancing the value of the piezoelectric constant. In PZT, close to the compositional MPB, the possibility of simultaneous existence of tetragonal and rhombohedral phases was detected over a finite composition range, which provides extra degrees of freedom for dipole arrangement. It is observed that ferroelectric piezoceramics show extremely good dielectric and piezoelectric properties near the phase coexistence region because it increases the number of

attainable spontaneous polarization directions [23]. Similar to MPB, scientific efforts are directed towards understanding the mechanism of high piezoelectric performance of PZT with the variation of doping elements, temperature regimes, chemical proportions, and phase transitions [24]. Among all the piezoceramics, materials with perovskite structure show the best piezoelectric properties because the asymmetric distribution of constituent elements allows easy deformation into non-centrosymmetric phases like monoclinic, orthorhombic, rhombohedral, and tetragonal. Most of the perovskite piezoelectric ceramics show the best performance near the compositional MPB, where it is viable to achieve the multiphase structure [16]. Considering the example of PZT, it is practicable to monitor the crystal symmetry with the Zr content between tetragonal and rhombohedral, and hence near Ti/Zr ratio close to 1 (near to MPB region), it is possible to achieve outstanding performance because of easy dipole reorientation. The piezoelectric performance of lead-based materials can be increased while compromising the Curie temperature since they are inversely related [25, 26], as shown in Fig. 4. Achieving high piezoelectric performance at the cost of reduced Curie temperature has several drawbacks, such as decreased polarization stability and larger variation in the piezoelectric properties with respect to temperature, which is not favourable for pragmatic applications [25]. There are other strategies to improve the output of Pb-ceramics, such as integrating dopants [16, 27], sintering aids [16, 28], and mixing with perovskite-structured compounds [29, 30].

Pb ceramics are classified as soft and hard based on their unique traits, “soft” lead-based ceramics are characterized by strong piezoelectric performance with high hysteresis loss, whereas the reverse is true for “hard” piezoceramics [16, 25]. Upon comparing soft PZT, hard PZT, and single crystals for vibration-based energy harvesters, it is found that for low-frequency off-resonance regime, soft PZT (PZT-5H and PZT-5A) outperform their counterpart hard PZT (PZT-4 and PZT-8). Also, single crystals lead magnesium niobate–lead zirconate titanate (PMN–PZT) outperform relatively hard Pb-based ceramics (PMN–PZT–Mn) [31].

Lead-based antiferroelectric (AFE) materials are crucial in applications like high-force actuators in the defence and aerospace industries [32]. The

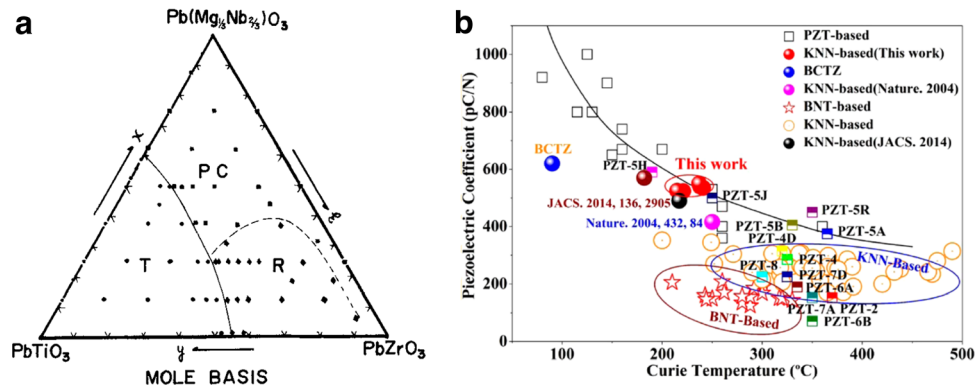


**Fig. 4** (a) Crystal structure dependence on the composition for PZT piezoceramic (PS: Pseudocubic, T: Tetragonal, R: Rhombohedral). Adapted/Re-used with authorization from

antiparallel neighbouring electric dipoles characterize an antiferroelectric phase. It is possible to change the antiferroelectric phase to a ferroelectric phase with an external electric field which is the key parameter in their internal strain dynamics. Here, the transformation from AFE to FE comes with a significant volume change in the unit cell, and hence considerable strain gets induced, which is helpful in high strain applications, as discussed earlier. The induced strain because of this transformation (0.3–0.6%) is way higher than the strain induced due to the electrostrictive effect (0.1%) [33]. It is practicable to maintain the AFE phase of material under certain environmental conditions with adequate precautions. However, it is also easy to induce ferroelectric (FE) or paraelectric (PE) phase transition with the help of an electric field or with variation in temperature, respectively, [34] accompanied by an increase in volume. Zhang and his team [35] discussed the electric field-induced strain properties and phase transition in Sm-doped PZST (Sm-PZST) ceramics, where it is observed that with an increase in the amount of Sm in PZST, the phase transition from FE to AFE takes place. During this transition, the most significant value of strain, 0.73%, was obtained near AFE/FE phase boundary at a frequency of 1 Hz, and that is why PZST is well known because of its high electrostrictive and energy storage properties [35]. It is no surprise that similar to the MPB existence in FE lead-based perovskites, AFE also has excellent values of induced strains near MPB compositions [36]. Detection of high piezoelectric response from Sm-modified PZT in the neighbourhood of Curie temperature led to new findings in the PZT research

citation 233. Copyright 1965, Wiley; and (b) relation between Curie temperature and  $d_{33}$ . Adapted/Re-used with authorization from citation 232. Copyright 2016, American Chemical Society

domain. The value for Sm-PZT is twice (915 pm/V) when compared to other dopants like Nb-PZT (477 pm/V) and La-PZT (435 pm/V), respectively. It is clearly shown that increased permittivity and MPB phenomenon is not solely responsible for the high piezoelectric response in Sm-doped PZT. Sm doping causes immense internal stress due to deviation in ionic radius, and PZT may allow the coexistence of pseudo-cubic and tetragonal phases below temperature  $T_C$ . The coexistence allows higher strain accommodation and, hence, more feasible interphase boundary motion; hence, a tremendous piezoelectric response is recorded for Sm-doped PZT [24]. Upon investigating the correlation between the microscopic distortion in crystals and macroscopic piezoelectric response for polycrystalline and epitaxial PZT thin films grown on magnesium oxide (MgO) and Si substrates, the results revealed a significant piezoelectric response in polycrystalline thin film because of ease of rotation of polarization direction of dipoles along with domain reorientation and crystal phase transition [37].

### 2.1.2 Lead-free piezoceramics

Lead-based materials possess many toxicity issues, such as environmental contamination and public health hazards; as a consequence, many restrictions are imposed on using lead-based ceramics in piezoelectric applications. Piezoelectric materials have applications in several major sectors, including biomedical and wearable devices, which motivates exploring alternative lead-free piezoceramics with comparable performance. The continuous efforts to

develop new lead-free piezoceramics led to several breakthroughs and the invention of lead-free candidates such as BT, BNT, ZnO, KNN, and BT–BF. KNN is well known because of its perovskite structure, biocompatible nature, high Curie temperature ( $\sim 623$  K), and high piezoelectric performance ( $\sim 190$  pC/N) with chemical formula  $(K_{0.5}Na_{0.5})NbO_3$ . A significant leap in the lead-free materials was taken by Saito et al. [38] when their efforts invented lead-free textured KNN ceramic with piezoelectric performance comparable to PZT. They proposed that the considerable enhancement in piezoelectric performance of KNN is possible because of the existence of MPB in alkaline niobate perovskites [39, 40] and the development of highly textured polycrystals [41]. A piezoelectric performance constant of 300 pC/N was attained without texturing for doped KNN, and a huge value of 416 pC/N with texturing for doped KNN is significant for lead-free ceramics. For better piezoelectric performance and temperature-based stability, materials with high Curie temperature were selected, namely, orthorhombic  $(K_{0.5}Na_{0.5})NbO_3$  ( $T_C = 415$  °C) and  $LiTaO_3$  ( $T_C = 615$  °C). In addition to  $LiTaO_3$ ,  $LiSbO_3$  was also used because the higher electronegativity difference between Sb and Nb will introduce a more covalent character into the bonding. The measured performance for  $(K, Na)NbO_3$ – $LiTaO_3$  was 230 pC/N with  $T_C = 323$  °C, whereas, for  $(K, Na)NbO_3$ – $LiTaO_3$ – $LiSbO_3$ , it increased up to 300 pC/N with  $T_C = 253$  °C which were outstanding values given the fact that they are lead-free materials. The overall performance of textured and doped KNN is summarized in Fig. 5, emphasizing that with microstructure engineering and elemental doping, it is feasible to achieve results (400–500 pC/N) comparable to PZT. From the theory of Landau–Devonshire–Ginzburg, it is concluded that the piezoelectric effect is proportional to saturation polarization ( $P_S$ ), and the value of  $P_S$  for KNN-based polycrystals is in the proximity of 15–25  $\mu C/cm^2$ . Moreover, it is comparable to PZT piezoceramics [42]. The research performed by Saito et al. [38] intensified the investigation on lead-free candidates for practical applications instead of lead-based materials and led to deeper insights into many novel phenomena, such as MPB and polymorphic phase transitions (PPT) in potential piezoceramics like BT, KNN, ZnO, and bismuth sodium titanate (BNT).

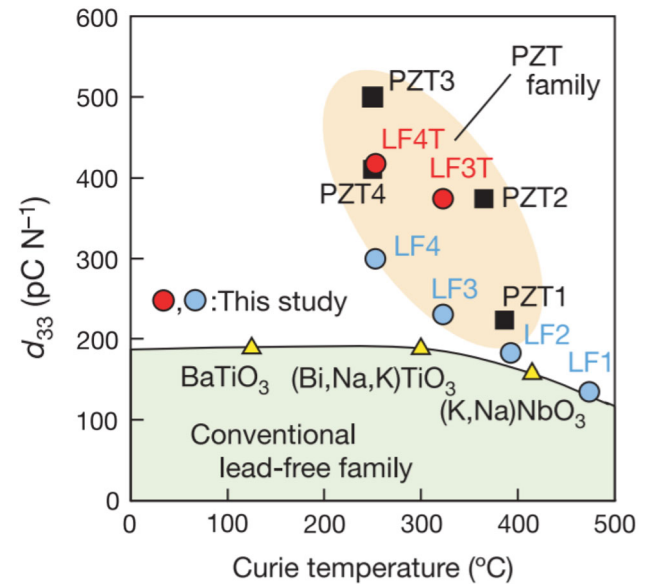


**Fig. 5** Comparison of lead-free (LF) piezoceramics with well-known PZT ceramics. Adapted/Re-used with authorization from citation [38]. Copyright 2004 Springer Nature

KNN is the leading candidate among lead-free ceramics because of its ferroelectric nature and attains the best piezoelectric performance near MPB [42, 43], similar to PZT. KNN exhibits orthorhombic crystal structure from room temperature to 220 °C, tetragonal structure in the range 220–420 °C, and cubic for above temperatures where it loses its ferroelectric properties [16, 42]. These three possible phase transitions in KNN at low temperatures are termed PPT. PPT effect plays a substantial part in the piezoelectric dynamics of KNN [44], and it is practical to get the best properties of KNN-based ceramics by shifting the PPT point towards room temperature (RT) with the help of dopants like  $Sb^{5+}$  [45] and  $LiNbO_3$  [46]. However, some PPT issues, such as temperature and ferroelectric domain instability [47], are recently addressed in some research works [47, 48]. The high electric field applied strain values are obtained near the orthorhombic–tetragonal and rhombohedral–tetragonal phase boundaries [49]. It is also practical to boost the properties of KNN with texturing, as reported in [38, 50], and simultaneously reduce the temperature dependency of the strain properties. Figure 6 shows the correlation between piezoelectric performance and Curie temperature for different phases of KNN [16]. Elemental doping influences several properties of the piezoelectric materials, including ferroelectric properties, thermal

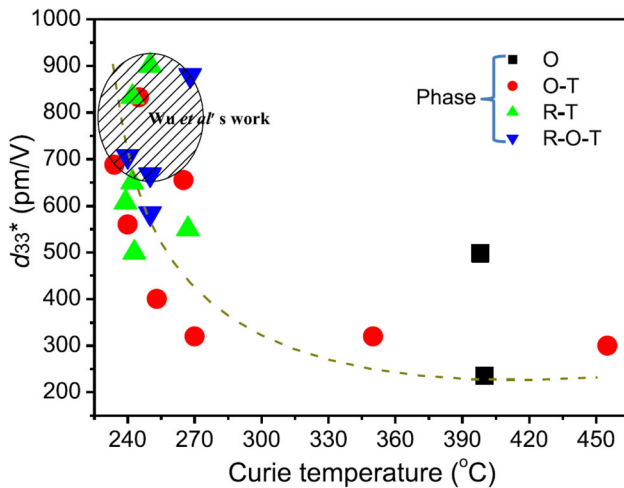


**Fig. 6** Relation between Curie temperature and  $d_{33}$  for KNN piezoceramic and crystal structure variation. Adapted/Re-used with authorization from citation [16]. Copyright 2019, Elsevier

stability, ageing, fatigue properties, dielectric properties, and microstructure [51].

Another novel route to enhance the piezoelectric properties of the KNN-based system was demonstrated experimentally by Gao and co-workers [52]. It was found that the given dopants (Bi, Sb, and Zr) induced a tetragonal phase with large-density nanoscale heterostructures, which enhanced the overall properties of the doped KNN. It is claimed that the development of local structure heterogeneity with comparable Landau and interfacial energies with average tetragonal structure improved the piezoelectric characteristics of KNN ceramics. Figure 7 summarizes the results obtained for Bi, Zr, and Sb-doped KNN.

As mentioned above, elemental doping, inducing local structural heterogeneity and texturing are prominent ways to improve performance drastically. Other than these methods, an invention of domain

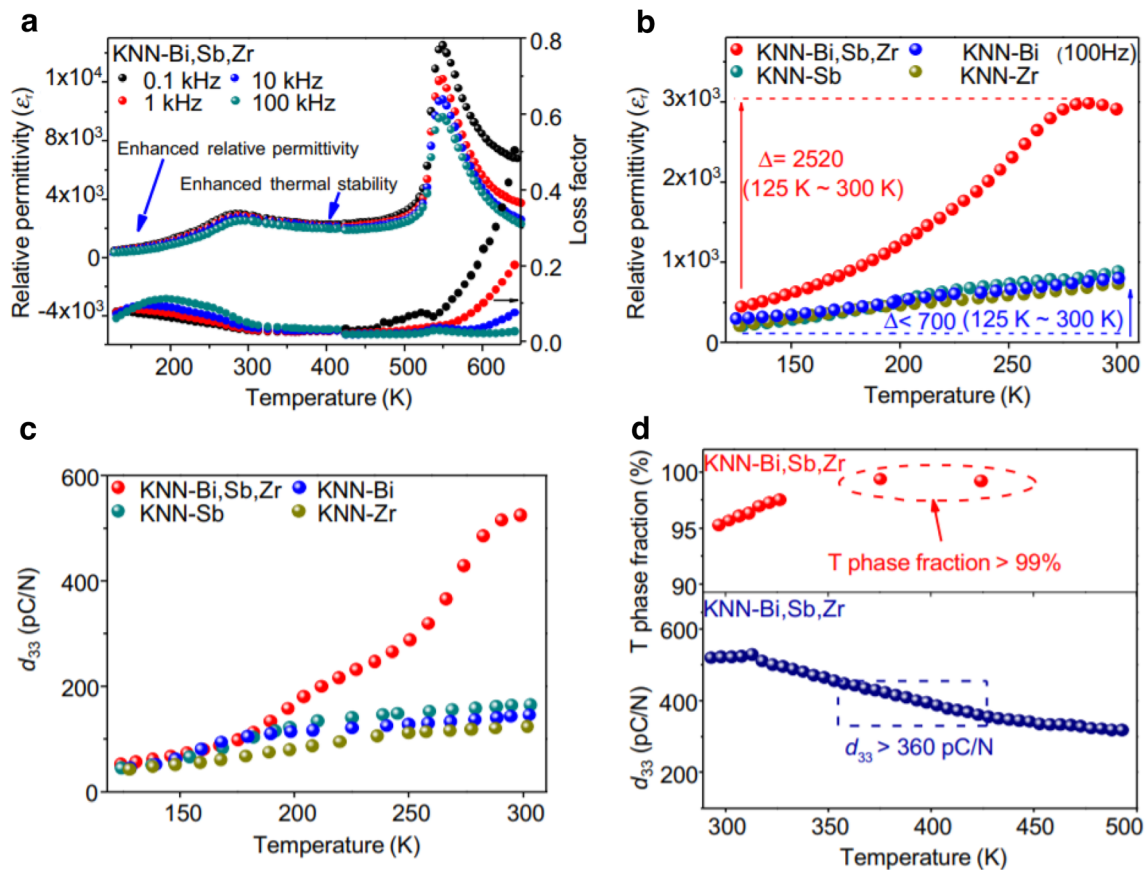


**Fig. 7** **a** Relative permittivity variation of KNN–Bi, Sb, Zr with respect to temperature and frequency, **b** relative permittivity of KNN with different doping elements with respect to temperature, **c**  $d_{33}$  variation for various KNN-doped samples as a function of

temperature, **d** comparative study of  $d_{33}$  and phase fraction in response to temperature. Adapted/Re-used with authorization from citation [52]. Copyright 2021 Springer Nature



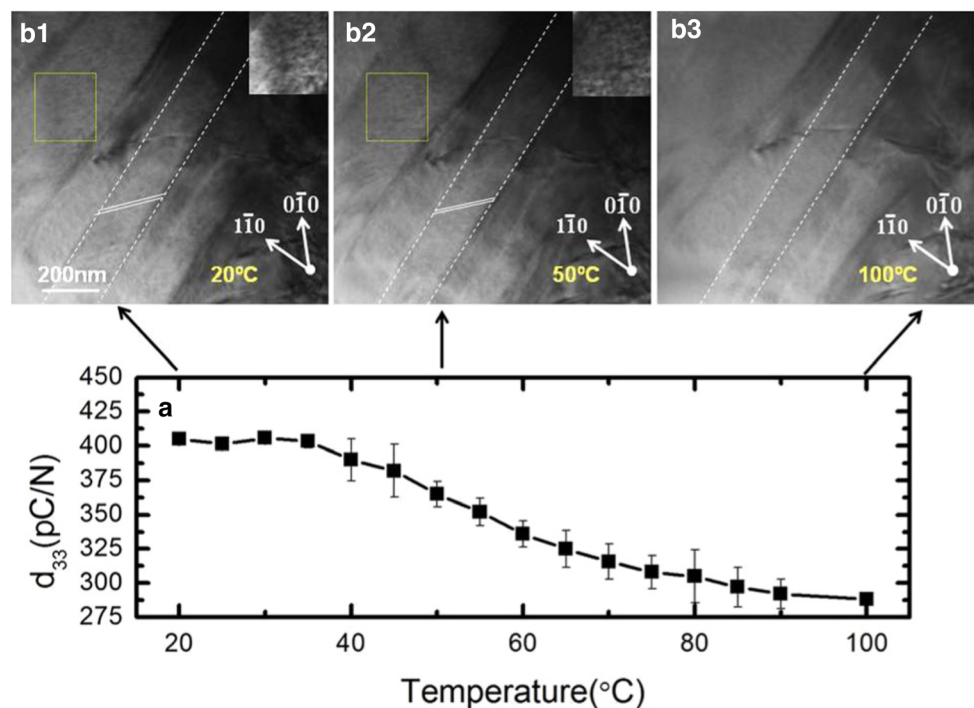
engineering led to new milestones in the development of synthetic piezoelectric materials; domain engineering refers to the process of reorientation of ferroelectric domains in polycrystals with the help of an external electric field [53]. Ferroelectric domain engineering in the case of perovskites is advancing because considerable modifications can be achieved with the help of poling process in which it is practical to align the domain in the applied electric field direction. The motion of domain walls in the presence of an external electric field contributes hugely to the high strain value. Poling treatment is most effective in the proximity of the orthorhombic–tetragonal phase boundary in the case of KNN-perovskite ceramics [42].

Given the relationship between  $c/a$  and  $d_{33}$  values for perovskite ceramics, a large  $c/a$  implies a high value for polarization. However, its direct relation with  $d_{33}$  is not true because small  $c/a$  favours domain wall motion since it reduces the internal compatibility stress and enhances piezoelectric performance [42]. The presence of ferroelectric domains contributes hugely to the piezoelectric performance of ferroelectric ceramics. Almost all synthetic ceramics need poling treatment to align ferroelectric domains inside the material [18, 19], which induces a macroscopic piezoelectric response in the material.

A detailed analysis of ferroelectric domains present inside the system  $0.96(\text{K}_{0.5}\text{Na}_{0.5})_{0.95}\text{Li}_{0.05}\text{Nb}_{0.93}\text{Sb}_{0.07}\text{O}_3-0.04\text{BaZrO}_3$  was performed using transmission electron microscopy (TEM) for exploration of the reasons for large piezoelectric constant (400 pC/N). The primary reason for the high piezoelectric performance is due to the presence of miniaturized nanodomain arrangement in a domain hierarchy. Loss of piezoelectric properties was observed upon heating the ceramic with the disappearance of the nanodomains, as shown in Fig. 8. Another factor contributing to the giant  $d_{33}$  is the simultaneous existence of tetragonal and orthorhombic phases, which provided easy dipole rotation due to more degrees of freedom and low polarization anisotropy [54].

An interesting theory related to the movement and re-sizing mechanism of ferroelectric domains present in KNN-based ceramic was demonstrated where authors studied the electric field caused stress–strain curves over a wide compositional range across PPT in Li-, Ta-, Sb-doped KNN (KNN–LTS). The observed highest value of coercive electric field ( $E_C$ ) near the PPT region for pristine samples supports the idea of the presence of nanodomains in the material, which strongly obstructs the motion of ferroelectric domain walls. The electric poling treatment for the same samples caused a sharp decline in the  $E_C$  value near

**Fig. 8** Disappearance of nanodomains with increasing temperature and a simultaneous decrease in  $d_{33}$  for ferroelectric KNNLS–BZ. Adapted/Re-used with authorization from citation [54]. Copyright 2015 American Institute of Physics



the PPT, confirming the formation of micron-sized ferroelectric domains, which are irreversible in nature. The development of micron-sized ferroelectric domains enabled the domain wall motion and accounted for the inverted macroscopic piezoelectricity in the PPT region of KNN–LTS [55].

In the ongoing quest to improve the functionality of piezoelectric materials, scientists developed several engineering techniques such as domain engineering, micro-texturing, and ageing treatment. The ageing of ceramic materials is another way to modify the piezoelectric performance in which high electrostrain can be induced in applications such as actuating materials in optics. As discussed by Lin et al. [56] and Hao et al. [16], the mechanism of induced high strain lies in the dynamics of point defects present in the material. As pointed out by the authors, when  $\text{Cu}^{2+}$  is used to displace the B site atom in KNN, charge neutrality will be maintained via oxygen vacancies, leading to the point defects (defect dipoles  $P_D$ ) that get created near the central atom. The defect polarization is oriented along the direction of saturation polarization ( $P_S$ ), and upon application of an external electric field,  $P_S$  will change its direction along the external electric field, whereas  $P_D$  will maintain its original polarization orientation during the complete domain switching. Removal of an external electric field causes a restoring force to act on  $P_S$  because of the alignment of  $P_D$ , and  $P_S$  will get oriented along its original direction, which originates a substantial effect known as double  $P$ – $E$  hysteresis

loop with significant non-linear strain in KNN polycrystals [56]. As already known, lead-free ferroelectric materials with high strain properties have many applications in the optical as well as the electronics industry.

Recently discovered porous Sb-doped sodium potassium niobate (NKNS) piezoceramics are also crucial from an industrial perspective because it has several advantages in underwater application [57]. Low acoustic impedance and better coupling with living tissues make them beneficial in low-frequency hydrophone applications and in medical diagnosis. The freeze-casting route is adopted to manufacture porous ceramics due to its environment-friendly nature, low material waste, and fast-manufacturing duration. The schematics of the freeze-cast porous NKNS are provided in Fig. 9. The piezoceramics' performance depends on porosity as piezoelectric properties decrease with respect to the reduction in the active ceramic phase. Observations revealed enhanced microstructure and better alignment of domains for microwave-sintered samples. Porous ceramics have a low dielectric constant because of the low volume fraction of ceramics. Significant results of the study are summarized in Fig. 10.

Similarly, BNT plays a vital role as lead-free piezoceramic with distorted rhombohedral crystal structures at room temperature [16]. BNT is a ferroelectric ceramic with a high remnant polarization of  $38 \mu\text{C}/\text{cm}^2$ , large  $E_C$  of  $73 \text{ kV}/\text{cm}$ , and exhibit a huge value of electric field-induced strain. A study was

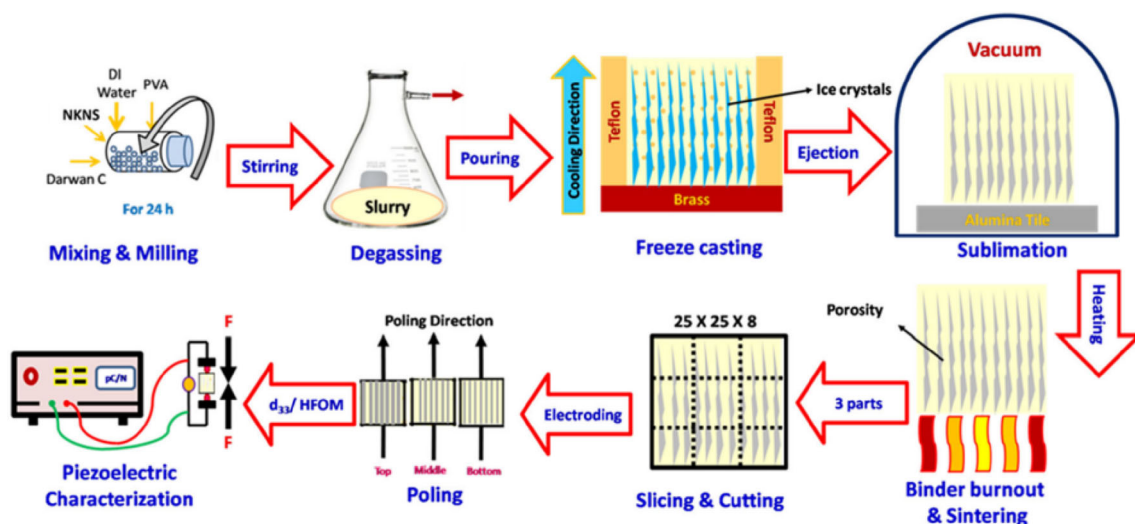


**Fig. 9** Schematics of the freeze casting of porous KNNS piezoelectric material. Adapted/Re-used with authorization from citation [57]. Copyright 2021 Springer

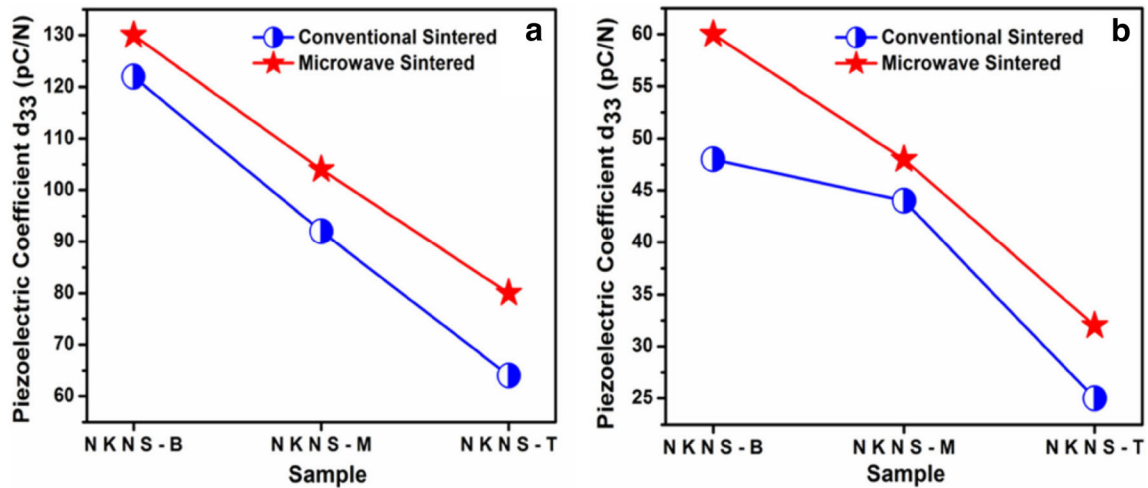
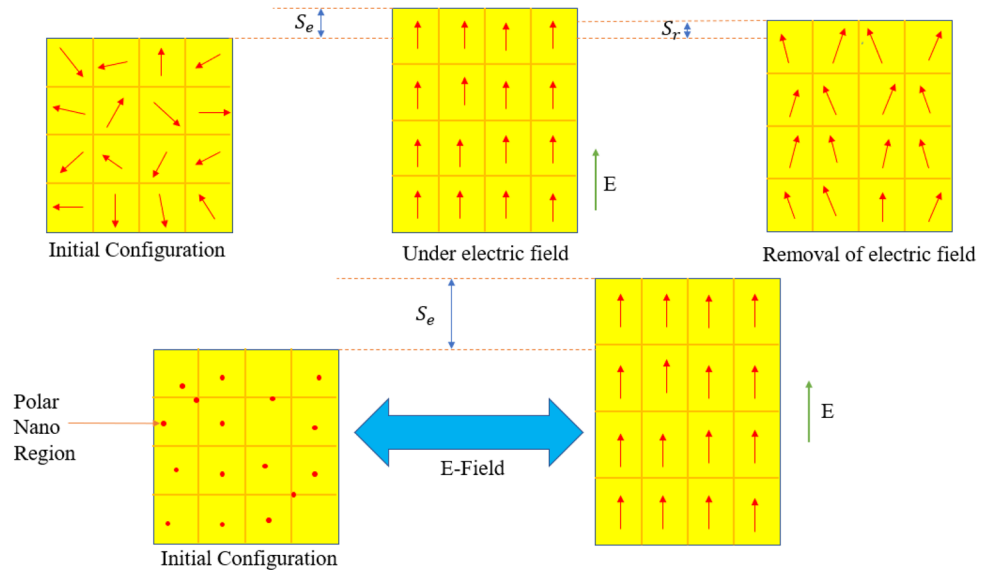


**Fig. 10** Piezoelectric coefficient of porous KNNS for (a) conventionally poled samples, and (b) corona-poled samples. Adapted/Re-used with authorization from citation [57]. Copyright 2021 Springer

**Fig. 11** Prototype to elucidate the physics behind the enormous electric field-induced strain in BNT-based ceramics



conducted based on bismuth sodium potassium titanate (BNKT)-based ceramic for strain enhancement. Sb doping in BNKT resulted in the phase transition from tetragonal ferroelectric to electrostrictive pseudo-cubic symmetry. This phase transformation decreased the piezoelectric performance of the material but simultaneously enhanced the electric field-induced strain value to 585 pm/V [58]. A similar phenomenon was observed where a 0.57% strain value was recorded for BNT-based piezoceramic [59]. The prototype to elucidate the enormous value of electric field-induced strain can be visualized in Fig. 11.

The model describes the transition in BNT-based ceramics from the non-polar pseudo-cubic to the polar anisotropic crystalline phase, primarily responsible for massive electric field-induced strain. Study of  $(\text{Bi}_{0.5}\text{Na}_{0.5})_{1-x}\text{Ba}_x\text{Ti}_{0.98}(\text{Fe}_{0.5}\text{Sb}_{0.5})_{0.02}\text{O}_3$  (BNBT100x-2FS) revealed that the randomly oriented ferroelectric domains present inside the material generates electric field-induced strain upon poling treatment and shows remnant strain upon removal of the field for  $x < 0.06$  as shown in Fig. 11. The prepared samples with  $x = 0.06$ , which are close to the ferroelectric non-polar phase boundary, possess polar nano-regions (PNRs) in a complete non-polar matrix, which showcases the ability to change between a

non-polar pseudo-cubic phase and a polar ferroelectric phase under cyclic electric field application. The transition between the two phases is possible because of their comparable free energies which eventually leads to a higher value of field-induced strain in the material [59].

Over a decade, several studies were performed to enhance the field-induced strain values in BNT ceramics, including chemical modifications where the BNT–BT–KNN system is used as base composition [60] having large poling strain values. Also, chemical modifications are performed in BNT–BT–KNN to break the long-range ferroelectric dipole order so that it is feasible to re-attain it via the application of an electric field [61], enhancing the field-caused strain values for the material. Microstructural design is another option feasible for strain value enhancement because it is built on the recognized material properties of the single crystal, enabling polycrystalline material to resemble its single-crystal part [62, 63]. A detailed MPB analysis of the BNT–BKT–KNN system showcased its switching characteristics. The addition of KNN causes the shift in MPB from MPB(I) to MPB(II), where MPB(I) corresponds to the coexistence between ferroelectric rhombohedral and tetragonal phases and MPB(II) corresponds to the coexistence between ferroelectric rhombohedral and relaxor pseudo-cubic phase. After the switch from MPB(I) to MPB(II) phase, a significant surge was observed in field-caused strain values (0.46%) for the BNT–BKT–KNN system [64].

BT was discovered in 1947, which was considered revolutionary because it can be converted into permanent piezoelectric material after poling treatment [5]. BT has an excellent piezoelectric performance, better than all existing natural piezo crystals of 190 pC/N. BT ceramic powder prepared hydrothermally acquired better dielectric properties than BT ceramic prepared via the conventional route [65]. Similar to BNT, BT ceramics found their application as actuator and similar techniques were developed to enhance the electric field-induced strain in them, such as doping [66], microstructural engineering [67], and ageing [16].

Lead-free piezoceramics will be the future materials in the piezoelectric applications because of toxicity issues in lead-based ceramics. KNN-based materials proved to be important because chemical modifications and texturing enabled them to match piezoelectric performance with that of Pb-based

ceramics [38]. Further improvement in their performance is possible by improving the sintering process with techniques like multi-step sintering to avoid the loss of alkali metals and probe the required stoichiometry for MPB [68]. The effect of multi-step sintering on the phase fraction in KNN needs to be addressed in detail. Also, it is important to explore rhombohedral to tetragonal (R–T) phase boundary in KNN-based ceramics via multi-elemental doping. In the era of machine learning, it is also possible to use the physical and chemical properties of the known ceramics as features to train the model, and build a system which can predict the properties the modified ceramic materials. Multiferroic BT–BF system is also crucial in this regard because it is lead-free, multi-functional, and has high Curie temperature. It is important to explore MPB in BT–BF with more sophisticated and advanced characterization techniques along with modified sintering techniques [69]. The phenomenon of local structure heterogeneity might be explored for multi-elements doping in piezoelectric ceramics for enhancing piezoelectric properties [52].

## 2.2 Piezo-polymers

Polymers are widely accepted in flexible electronics domain because of their low density, flexibility, lightweight, ease of processing, and cost-effectiveness. Polymers are amorphous in nature, and hence they do not have good piezoelectric or electrostrictive performance when compared with ceramics [2, 70]. Low dielectric constant and acoustic impedance made them very important in the field of sensors. First-time piezoelectric activity in PVDF  $[(\text{CH}_2\text{-CF}_2)_n]$  was observed in 1969, which is a well-known ferroelectric polymer, and later its co-polymers were discovered with excellent piezoelectric output among other polymers [2, 70]. PVDF occurs in many phases, but only the  $\beta$ -phase was studied widely in the piezoelectric research community because of its all-trans chain conformations, which create permanent dipole in PVDF, as shown in Fig. 12. Similar to the case of ceramics, poling is essential for polymers as well to induce permanent dipoles because of their inherent amorphous nature [2, 70]. Other co-polymers of PVDF, such as PVDF–TrFE, PVDF–TeFE, and PVDF–HFP, were broadly explored because of their enhanced performance due to steric hindrance as compared to PVDF [71, 72]. A relative comparison

**Fig. 12** Schematics of the  $\beta$ -phase of PVDF. An inherent dipole is present in the  $\beta$ -phase because of the Trans position of hydrogen and fluorine atoms

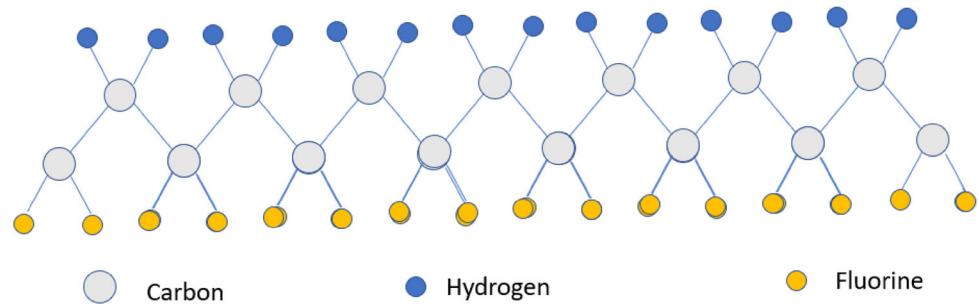


**Table 1** Comparison between properties of PZT (piezoelectric ceramic) and PVDF (piezoelectric polymer) [11]. Adapted/Re-used with authorization from citation [11]. Copyright 2019 Wiley

Properties	PZT	PVDF
Piezoelectricity properties	High	Low
Acoustic impedance	High	Low
Density ( $10^3 \text{ kg m}^{-3}$ )	7.5	1.78
Relative permittivity	1200	12
Piezo-strain constant ( $10^{-12} \text{ C N}^{-1}$ )	225–590	– 33
Piezo-stress constant ( $10^{-3} \text{ Vm N}^{-1}$ )	26	– 330
Electromechanical coupling (% at 1 kHz)	30	12
Dielectric constant	1180	10–15
Mechanical Flexibility	Poor	Outstanding
Curie temperature ( $^{\circ}\text{C}$ )	386	80

**Table 2** Piezoelectric polymers available with their piezoelectric and dielectric properties

Polymers	$d_{33}$ (pC/N)	Relative permittivity	References
PVDF	– 24 to – 34	6–12	[22, 73]
PVDF-TrFE	24 to 40	18	[74, 75]
PVDF-HFP	24	11	[76, 77]
Polyamide 11	4	5	[78]
Cellulose	5.7	2.6	[79, 80]
Polyurea	19	6	[81, 82]
Polyimide	2.5 to 16.5	4	[83]

between piezoelectric ceramic (PZT) and piezoelectric polymer (PVDF) is given in Table 1 [11].

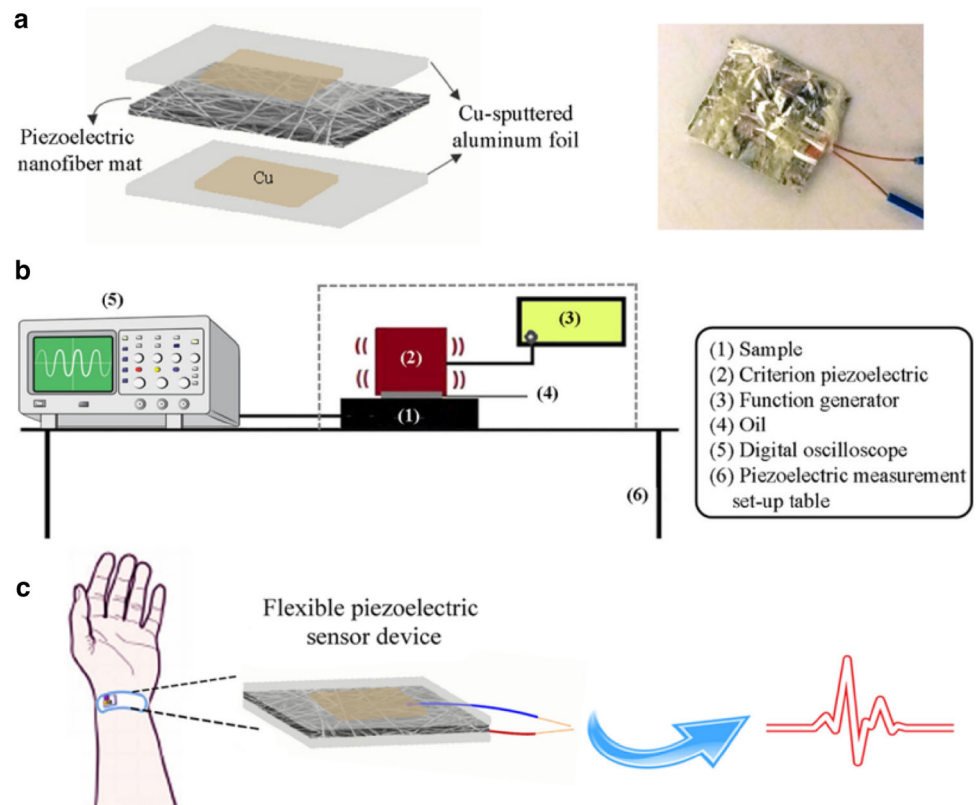
Polymers have exciting properties and are widely explored in piezoelectric nanogenerator applications. Some other well-known polymers with good piezoelectric performance are polylactic acid (PLA), polyamide 11, polyimide, polyurea, and celluloses [11, 22]. To enhance polymers’ performance, they usually undergo processes like stretching, drawing, and corona poling (Table 2) [22].

PVDF and its co-polymers are primarily used for flexible nanogenerator applications because of the polar nature of  $\beta$ -phase of PVDF (all TTT chain conformations as in Fig. 12) and its excellent properties as ferroelectric material with a dipole moment of  $8 \times 10^{-30}\text{Cm}$ . Other co-polymers perform better

because extra PVDF fluorine atoms cause steric hindrance and limit the formation of non-polar phases [11].

PVDF has excellent piezoelectric properties, and scientists in the biomedical domain have given a lot of attention to flexible and self-powered piezoelectric devices based on ferroelectric polymers because of the drawbacks of conventional real-time biomedical monitoring devices, such as high-power consumption and rigid structure. Many researchers recently explored the metal–organic frameworks (MOF), which are newly invented nano-porous crystalline materials having unique properties such as adjustable pore size, high porosity, and large surface area to increase the piezoelectric properties of PVDF. Moghadam et al. [84] made a novel self-sustainable

**Fig. 13** Schematics of (a) sensor fabrication, (b) measurement setup, and (c) recording of radial artery pulse signals. Adapted/Re-used with authorization from citation [84]. Copyright 2020 American Chemical Society



flexible piezoelectric sensor device for wrist pulse monitoring with UiO-66 MOF-incorporated (Zr-based metal organic framework) PVDF nanofibers. It is observed that the percentage of  $\beta$ -phase increases, whereas the size of electrospun polymer fibres decreases, resulting in flexible piezoelectric membranes with high performance (568 mV). The functioning of the developed self-sustainable (Fig. 13) device is comparable to or better than other reported PVDF energy harvesters so far [85–87].

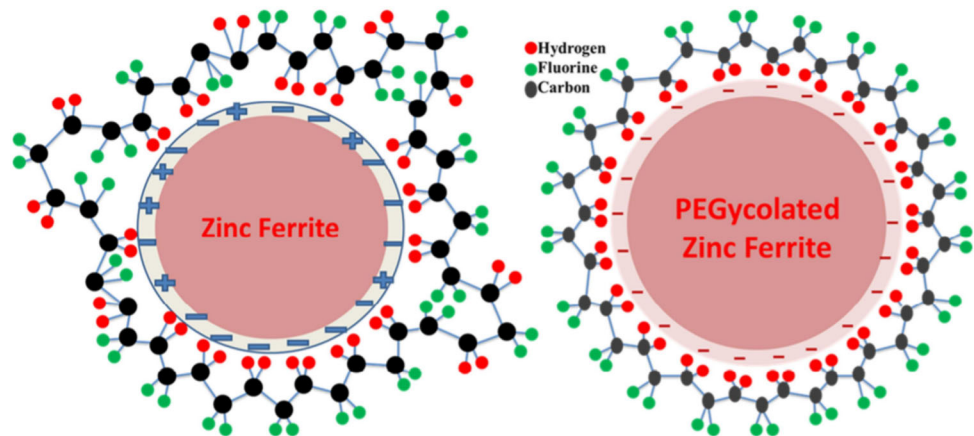
Chinya et al. [88] prepared flexible nanocomposite films using PVDF and polyglycolated Zinc ferrite (ZF), where sol-gel auto-combustion prepared ZF particles were treated with polyethylene-glycol-6000 (PEG-6000), and films were prepared using casting technique. The PEG-6000 treated sample showed better dielectric and piezoelectric properties because the PEG layer acts as a coupling between organic and inorganic parts of the composite and improves the Maxwell-Wagner-Sillars interfacial polarization (Fig. 14). These modifications improved energy storage density ( $4.3 \text{ J/cm}^3$ ) and maximum energy discharge efficiency with an open-circuit voltage of 18 V. It is essential for better coupling between ceramic and polymer matrix to functionalize ceramic particles

with various matrix-compatible surfactants, polymers, and natural materials.

Poly(lactic acid) (PLA) is popular within the research community because of its biodegradable nature, mechanical stability, ease of fabrication, and flexibility. The carbonyl group in the structure induces polarity and showcases piezoelectric performance without poling treatment which is desirable for energy harvesting applications. Tajitsu [89] attempted to enhance the piezoelectric performance of PLA by designing a film actuator whose driving force is a surface wave which induces shear motion where it is concluded that the crystal structure of PLA is helical. However, it has several disadvantages, such as higher cost, the requirement of food crops for synthesis, a prolonged composting rate, an effect on the soil's pH value, lower melting point making it unstable at higher temperatures, and low mechanical properties.

As a biomaterial, cellulose is readily available and is multifunctional in the energy harvesting and sensors industry. Dipolar alignment and confined charges hugely contribute to cellulose's piezoelectric activity and are comparable to naturally occurring quartz crystals. The enhanced piezoelectric

**Fig. 14** Zinc ferrite and suggested interaction between ZF and PEG-6000. Adapted/ Re-used with authorization from citation [88]. Copyright 2017 Elsevier



performance of bacterial cellulose (BC) was attained by incorporating  $\text{MnFe}_2\text{O}_4$ . The sensors were manufactured using the composite films of  $\text{BC}/\text{MnFe}_2\text{O}_4$ , where the piezoelectric response raised from 5 to 23 pC/N [90]. Scientists explored odd-numbered polyamides and showed the existence of piezoelectric behaviour because of their inherent polar nature [91].

In summary, PVDF and its co-polymers are highly desirable in piezoelectric applications because of their inherent dipole moment. Also, it is possible to understand the fundamental mechanism in PVDF for piezoelectricity via structural characterization and molecular simulation to achieve a performance as high as  $-62$  pC/N [92]. Other bio-polymer such as cellulose is also potential candidate for piezoelectric application because of its high crystallization and inherent abundance of polar hydroxyl groups with strong electron donating capacity. Further attention is required towards cellulose-based composite to understand the piezoelectric dynamics in detail for enhancement comparable to PVDF [93]. Also, recently reported polarization interlocking phenomenon in PVDF needs further attention to understand the relevant dynamics [94]. Nanogenerators have wide applications in wearable piezoelectric devices, and their poor stretchability and mechanical stability limits their applications because constant movements induce deformations in the polymer. Incorporation of other structural adhesives might improve the properties of PVDF films substantially [95].

### 2.3 Piezo-composites

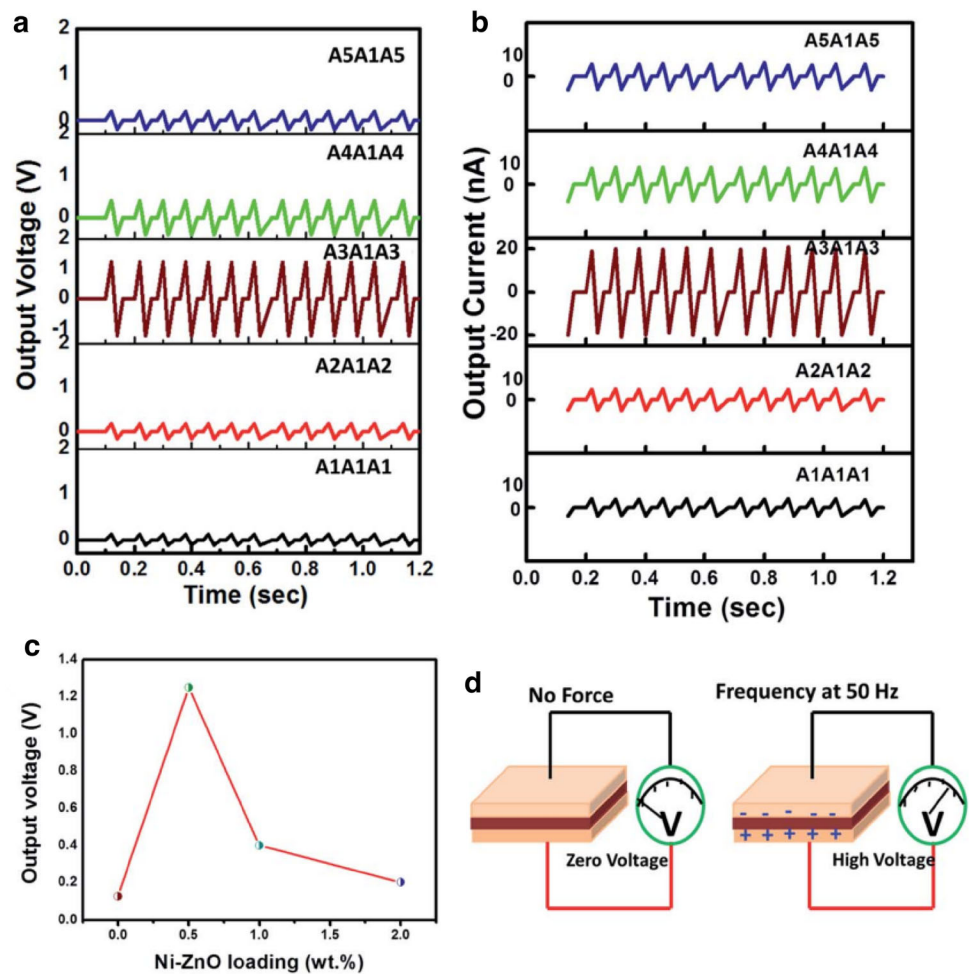
Researchers directed their attention towards composite materials to harness the outstanding

characteristics of ceramics and the flexibility of polymers simultaneously. Fabrication technology of composite materials created the path to probe the best characteristics of both ceramics and polymers for application in energy harvesting systems. The study of piezoelectric composites is rich and offers multi-dimensional applications in biomedical devices, sensors, and energy scavenging. Recently, intense research has been carried out on piezoelectric composites, which produce sustainable solutions for low-power and high-performance electronic devices [96].

#### 2.3.1 Advances in piezo-composites

The first breakthrough in piezoelectric nanogenerators was in 2006 by Wang and Song when they reported the first-ever nanogenerator based on ZnO nanowires. The authors showed that when the aligned nanowires of ZnO are deflected with the help of the tip of the probe of an atomic force microscope (AFM), the coupling between the piezoelectric and semiconducting properties occurs in ZnO, which results in the charge separation and strain field across the nanowire. This phenomenon causes the formation of the Schottky barrier between the metal tip and the ZnO nanowires, which creates an electrical current with an efficiency of 17 to 30%. This breakthrough in converting nanoscale mechanical energy into electrical energy with ZnO nanowires caused a paradigm shift in the piezoelectric community, and nanocomposites became potential applicants for energy harvesting applications. Later, intense efforts from the scientific community led to the invention of novel fabrication techniques for composites to strengthen the performance of piezoelectric nanogenerators [97].

**Fig. 15** **a** Output voltage vs time, **b** output current vs time for different composites of Ni-ZnO and PVDF-HFP, **c** max voltage attained as a function of filler content, **d** mechanism of direct piezoelectric effect. Adapted/Re-used with authorization from citation [98]. Copyright 2017 Royal Society of Chemistry



Tri-layer nanocomposites with Ni-doped ZnO and PVDF-HFP were formed first time through the sandwich preparation technique, where the layer-by-layer structure showed enhanced properties compared to the monolayer. XRD analysis showed Ni doping in ZnO caused a decrease in the intensity values of peaks with broadening and slight shift towards the low angle value, which indicates Ni ions occupied interstitial position and the samples are in uniform compressive stress. The decreased crystallite size after doping resulted from the distortion in the lattice due to Ni doping, and the strain enhancement eventually increased the piezoelectric performance of Ni-ZnO. Dielectric studies of the tri-layer composites showed that the values of the dielectric constant increase in the low-frequency regions with the addition of the nanofillers because of the interfacial polarization within ceramic particles and polymer matrix. The values tend to decrease at higher frequencies because of the lower contributions from

dipolar effects. The piezoelectric performance of the tri-layer composites was evaluated and shown in Fig. 15, where it was observed that composite with 0.5 wt% Ni-doped ZnO highly increased voltage as compared to other composites due to uniform distribution of filler also the nomenclature for the composites is as follows: A1(PVDF-HFP) and A3(PVDF-HFP/0.5 wt% Ni-ZnO) [98].

Chary and group [99] prepared an energy harvester based on a large aspect ratio  $\text{Ba}_{0.85}\text{Ca}_{0.15}\text{Zr}_{0.1}\text{Ti}_{0.9}\text{O}_3$  (BCZT) nanofibers prepared with RT vulcanized silicone elastomer using the electrospinning technique. The newly developed BCZT nanofibers with standardized sintering temperatures were used to fabricate nanogenerator with required toughness and flexibility having potential applications in wireless microelectronics and structural health monitoring. The fabrication of nanogenerator was done with the help of sintered nanofibers obtained via electrospinning of precursor gel of



BCZT-PVP. Structural analysis of BCZT revealed the appearance of the perovskite phase for sintering temperature above 500 °C, and the grain growth caused the narrowing of XRD peaks. Although the crystal structure of Ba (Zr<sub>0.1</sub>Ti<sub>0.9</sub>)O<sub>3</sub> is rhombohedral at RT, the substitution of Ca<sup>2+</sup> ion at the “A” site is responsible for splitting (002) plane, and hence creates an MPB between the tetragonal and orthorhombic phases. The Raman spectra of BCZT showed a broadening of the A1(TO<sub>2</sub>) peak at 205 cm<sup>-1</sup>, which indicates the phase transformation from tetragonal to rhombohedral and occurred due to the substitution of Zr at the Ti site. The peak at 738 cm<sup>-1</sup> confirmed the presence of the tetragonal phase in BCZT, and the above phase formation was confirmed via thermogravimetry analysis (TGA). Dielectric studies of BCZT sintered nanofibers were carried out to study the polarization dynamics better and understand phase transition. An expected trend was observed in the variation of the dielectric constant with respect to the frequency since the decline in the dielectric constant at higher frequencies is expected due to a lowering of polarization time. The dielectric constant increased from 0 to 108 °C due to a decrease in dipole relaxation time. The phase transition from ferroelectric to non-ferroelectric caused the decrease in dipole relaxation time, and results demonstrated that the Curie temperature for BCZT is close to 108.8 °C. The Curie temperature of 108.8 °C is much higher than the ceramic counterpart (80–85 °C). The possible reason for this increment is that electrospun fibres have a diameter in the range of 80–250 nm with a very small grain size in the order of 10–20 nm, and hence the reduced grain size in nanofibers results in a large grain boundary density and relieves the internal stress in the material due to sliding of the grain boundary. This results in the decreased free energy of the ferroelectric phase and is responsible for the increased value of the  $T_C$ . Several other studies were performed to manufacture nanocomposites for piezoelectric nanogenerators, and researchers obtained remarkable results and output favourable for industrial applications. Therefore, it is vital to perform a detailed analysis of the fabrication of the piezo-composites and nanogenerators and the factors that affect their performance.

Recently, in piezoelectric composite research, two-dimensional materials are becoming centre of attraction because of their unique characteristics such as ferroelectric nature, non-centrosymmetry in 2D

plane, and better mechanical-to-electrical conversion efficiency. Two-dimensional nanomaterials such as boron nitride (BN), tungsten diselenide, and molybdenum sulphide have excellent flexibility when compared with conventional piezoelectric one-dimensional nanorods and nanowires. h-BN is a wide-band semiconductor with high thermal conductivity, chemically inert, and environmentally friendly. BN is well known for its planar three-fold symmetry, which does not allow electric polarization in its ground state, but when the BN sheet is enveloped into a nanotube, the symmetry breaks and leads to the polarization along the cylindrical axis, which is governed by the boundary conditions on the electronic states present around the nanotube's circumference [100]. Hence, the electric polarization in BN nanotubes has a quantum mechanical origin, which can be formulated using Berry's conjecture. Kuang and group [101] created boron nitride nanosheets (BNNS)-based piezo-triboelectric nanogenerator with PDMS polymer, which showed a current density of 230 mA/m<sup>2</sup>, an output voltage of 1870 V, and a power density of 100 W/m<sup>2</sup>. The schematics of the piezo/triboelectric nanogenerator fabrication using BNNS-PDMS/PA6, including its electrical output characteristics are shown in Fig. 16. Authors used powder of h-BN (98% Aldrich) and added into glass vial with isopropanol for magnetic stirring and then finally ultrasonicated to achieve the required morphology. The BNNS-PDMS membranes were fabricated through the process of spin coating.

Boron nitride nanotubes (BNNT) possess a strength-to-weight ratio equivalent to carbon nanotubes (CNTs), high-temperature stability up to 800 °C, and outstanding neutron radiation shielding properties, which are essential for space missions [102]. The multifunctional electroactive nanocomposite was developed using boron nitride nanotubes which showcase significant electroactive coefficients. Authors aligned the BNNTs present in the composite via stretching the 2 wt% BNNT/polyimide film and found the value of  $d_{33}$  equal to - 4.17 pm/V which is quite high for 2D materials [102].

2D materials also possess high crystallinity and strength to endure high levels of strain during piezoelectric applications. MoS<sub>2</sub> is an interesting 2D material because they do not display the piezoelectric phenomenon in bulk form because of opposite alignments of the neighbouring atomic layers, which induces centrosymmetry in bulk. When the

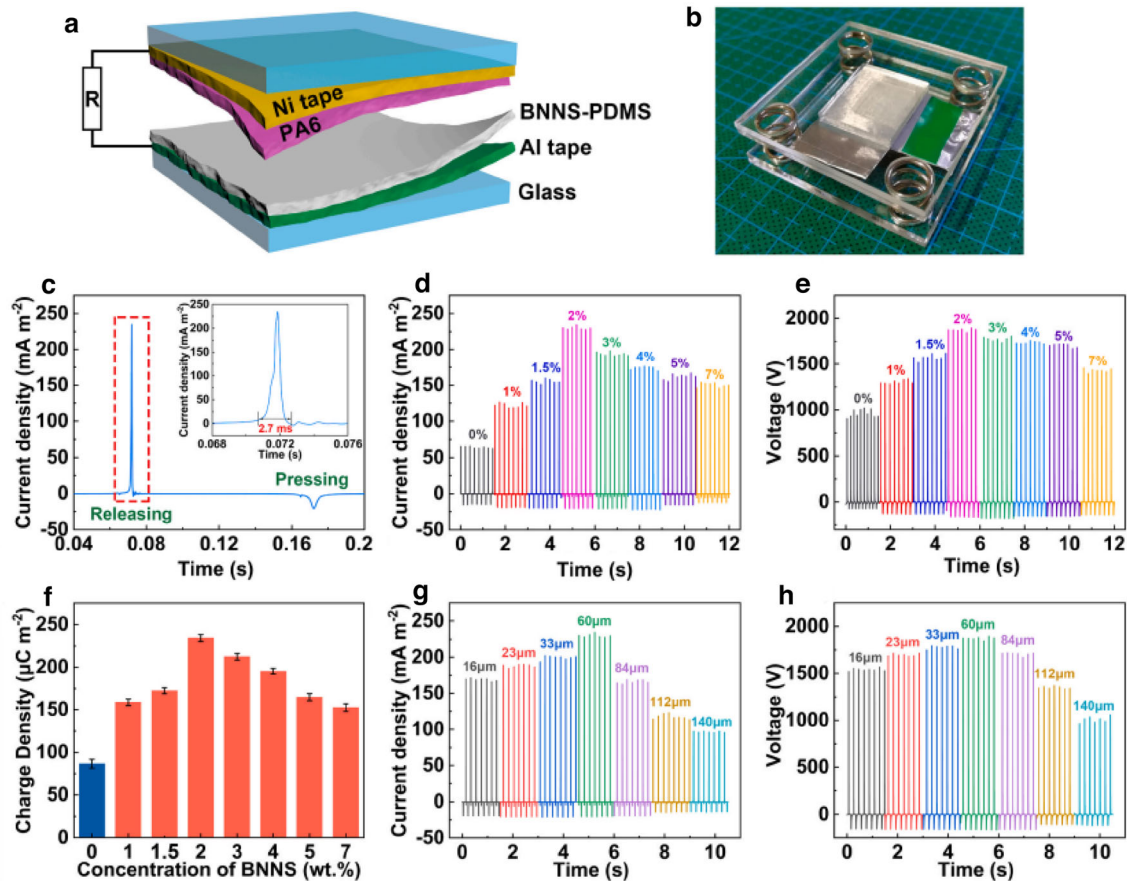


**Fig. 16** Schematics of the piezo-triboelectric nanogenerator based on BNNS-PDMS/PA6 and its electrical output characteristics, **a** 3D view of the generator, **b** photo of nanogenerator, **c** enlarged view of an output waveform of nanogenerator, **d** short-circuit current density with respect to time, **e** output voltage of

nanogenerator with respect to time, **f** charge density of the composite as a function of BNNS weight composition, **g** short-circuit current density, and **h** output voltage with respect to of BNNS-PDMS membrane thickness. Adapted/Re-used with authorization from citation [101]. Copyright 2021 Elsevier

identical  $\text{MoS}_2$  is thinned to a few odd-numbered layers, inversion symmetry vanishes, and piezoelectricity appears; hence the effect in 2D  $\text{MoS}_2$  depends on the number of layers [103]. It is shown that strain-induced polarization charges in  $\text{MoS}_2$  modulate the charge transport at the interface and is responsible for the increased strain-sensing properties [104]. Undoped  $\text{MoS}_2$  has low piezoelectric response also finite charge carrier density; hence modification of the distribution of free charge carriers in  $\text{MoS}_2$  or additional doping can result in higher piezoelectricity [103, 105]. Nakamura [106] reported that the p-type  $\text{MoS}_2$  monolayer has high longitudinal gauge factors than n-type  $\text{MoS}_2$ . When uniaxial tensile strain is applied to a p-type monolayer, carrier reallocation occurs in the bands, which causes asymmetrical modulation of carrier transport and hence higher piezoelectric response. Choi et al. [103] implied that it

is viable to tune the piezoelectric properties with the precise control of defects in 2D  $\text{MoS}_2$ . The difference in atomic bonding lengths creates inequivalent charge distribution, which results in the broken reflection symmetry along the vertical direction. Choi et al. in [103] extended the thermal solvent method for the synthesis of asymmetrical 2D  $\text{MoS}_2$  with induced defects for achieving exceptional piezoelectric properties where authors obtained current and voltage of 20 pA and 700 mV respectively (Fig. 17).

Graphene oxide (GO) as well-captivated massive attention from the community because of its many applications attributed to various functional groups present in it, such as ketonic, carboxylic, hydroxyl, and epoxy [107]. The incorporation of GO and reduced-GO (RGO) in PVDF-TrFE-based composites resulted in the crystallization of the ferroelectric phase, which enhanced the properties of the

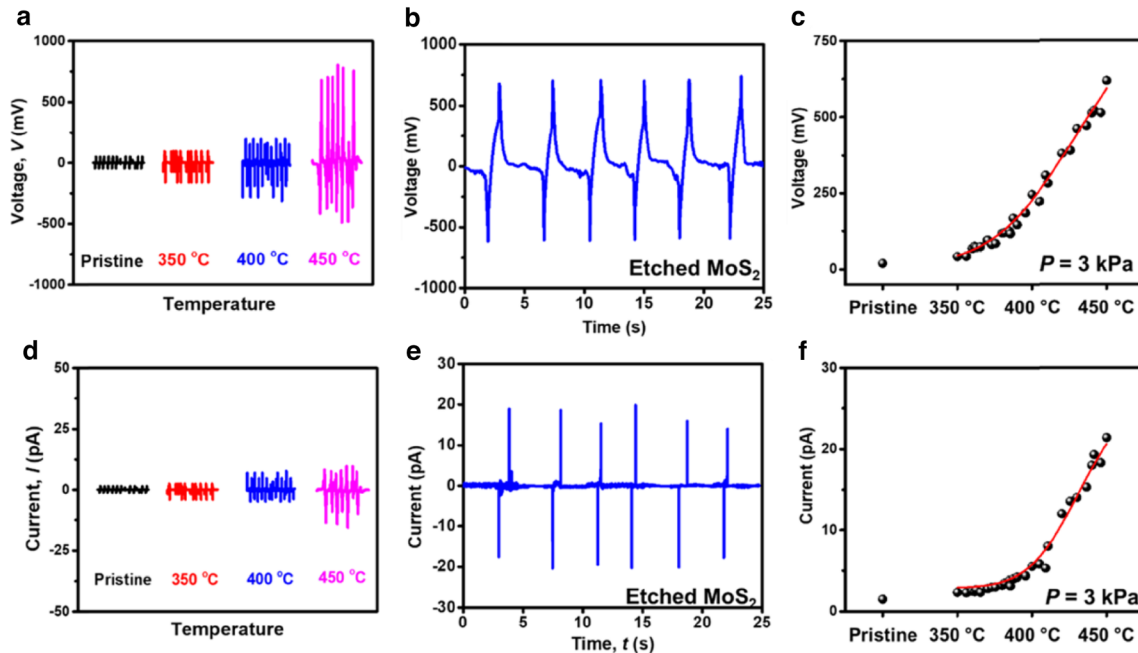


**Fig. 17** Piezoelectric characteristics of MoS<sub>2</sub> (a, d) output voltage and current with respect to temperature for samples MoS<sub>2</sub>, (b, e) current and voltage data of 450- MoS<sub>2</sub>, (c, f) output voltage and current values of pristine and ten samples annealed between 350

and 450 °C which revealed that systematically controlled sulphur vacancy has an output current enhancement. Adapted/Re-used with authorization from citation [103]. Copyright 2021 American Chemical Society

fabricated composite materials. The high Young's modulus and dielectric constant of GO are shown to be responsible for the effective transmission of electrical and mechanical energy [107]. From experiments, it can be concluded that using charged materials' interface with ferroelectric polymers is a great way to improve the piezoelectric performance of materials. Authors prepared the bilayer films with drop casting of GO on the PVDF-TrFE film followed by vacuum drying at room temperature. The working mechanism and the voltage output characteristics for the bilayer energy harvesting devices are provided in Fig. 18.

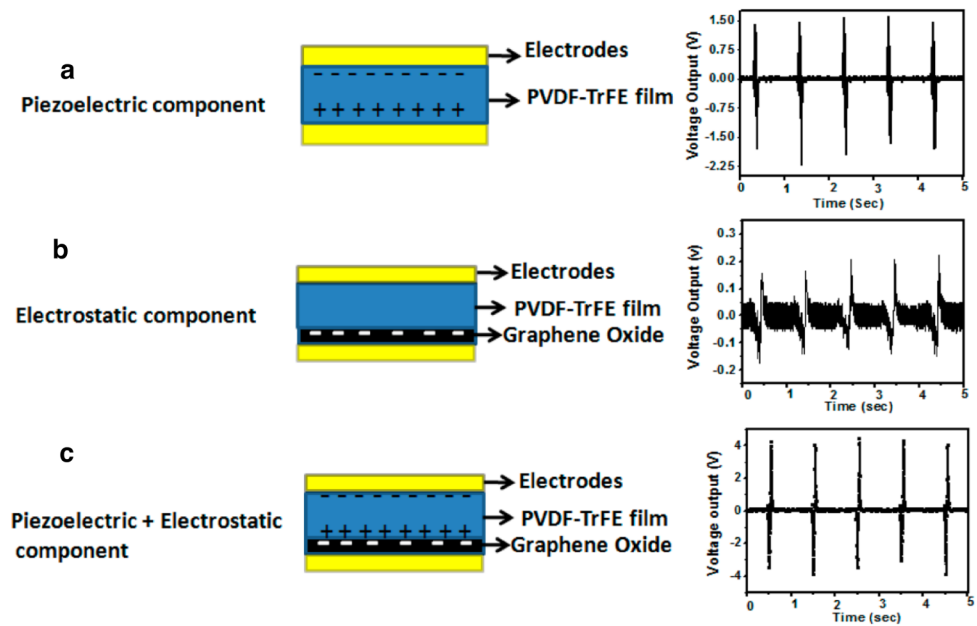
Transition metal dichalcogenides possess intrinsic piezoelectricity due to their inherent non-centrosymmetric structure, and tungsten disulphide has been explored for its good electrical and optical properties. Zhou et al. [108] reported direct evidence of intrinsic piezoelectric behaviour in WS<sub>2</sub> monolayer with 325 pA and 65 mV as output performance.

Some critical advancements are also reported in the case of piezoelectric polymers which perform a pivotal role in fabricating composites for energy applications. As known, in order to transform mechanical energy into electrical energy, an induced net

polarization is essential in polymers via poling process. Shepelin et al. [94] invented the polarization locking phenomenon in PVDF-TrFE perpendicular to the base plane of 2D Ti<sub>3</sub>C<sub>2</sub>T<sub>x</sub> MXene nanosheets and showed that the strong electrostatic interaction-based polarization locking can demonstrate an outstanding energy harvesting performance of − 52 pC/N. The fabrication of a self-sustainable linear pressure sensor was carried out with the help of a blend of MXene and PVDF-TrFE. MXene supported the percentage increment in the electroactive phase of PVDF-TrFE and improved the polarization of the fibres during the electrospinning process, generating an output voltage of 1.58 V, three times the pure PVDF-TrFE with linear voltage-pressure response [109].

Polypyrrole (Ppy) is a conductive polymer with a facile preparation route and is easy to blend with other polymers; a recent study reported that incorporating Ppy fillers in PDMS dramatically improves the dielectric constant and conductivity of the composites. In human wearable applications, self-powered and biodegradable electronic devices are in huge demand, and recently, Veeralingam and his team [110] made a low-cost PDMS/Ppy composite-based nanogenerator as a self-driven arterial pulse

**Fig. 18** Schematics of the functioning mechanism of the bilayer harvesting device. Adapted/Re-used with authorization from citation [107]. Copyright 2016 American Chemical Society



pressure sensor. The authors successfully fabricated the piezoelectric nanogenerator with Al-coated polyethylene terephthalate (PET)/(PDMS: Ppy)/ITO-coated PET and drew a voltage output of 12 V and a current density of 110 nA/cm<sup>2</sup> when 1.47 N/cm<sup>2</sup> pressure was applied.

### 2.3.2 Factors affecting piezoelectric properties of composites

Piezo-composites' performance depends on several factors during their manufacturing, such as filler volume fractions, temperature, synthesis procedures, and several other elements. After years of research, many cutting-edge techniques are available for piezoelectric composite fabrication, namely, dice and fill [111], solvent casting [112], 3D printing [113], dielectrophoresis [114], and injection moulding [115], which significantly affect the piezoelectric and dielectric performance of piezo-composites. The factors that substantially affect a piezo-composite's piezoelectric performance are arranged in Fig. 19 and are discussed in detail.

**2.3.2.1 Crystallinity** The degree of crystallinity of polymers and ceramics performs a vital role in the performance of piezo-composite because [116–118] high crystallinity of constituents increases the tensile strength, elastic modulus, and heat resistance of the polymer [119]. Researchers incorporated various

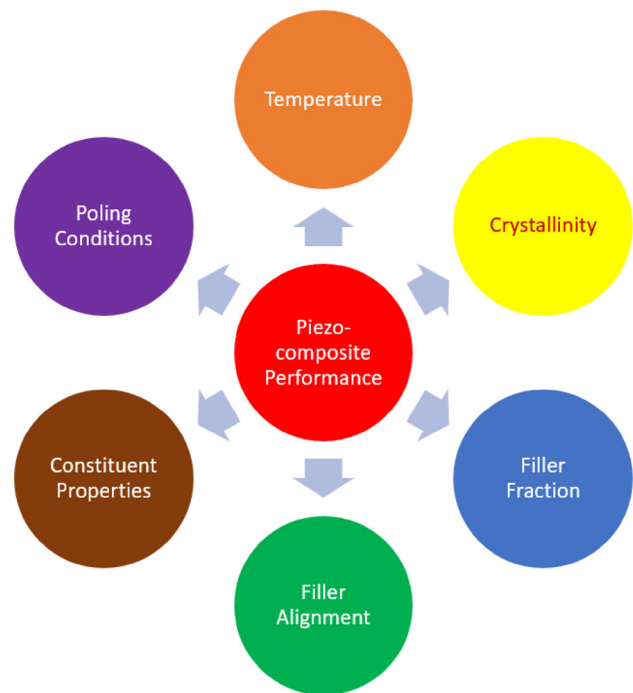


**Fig. 19** Essential factors during the manufacturing process affecting the overall performance of the piezoelectric nanocomposites

fillers in the PVDF to increase the crystallization of the polar phase of PVDF for better piezoelectric performance and increment in the  $\beta$ -phase of PVDF [120, 121]. In the case of ceramics, it is evident that single crystals will show higher piezoelectric performance than other polycrystalline ceramics because of

the highly ordered crystal structure and dipole alignment [2, 122, 123].

**2.3.2.2 Filler alignment** Filler alignment inside the composite decreases interparticle distance and increases the piezoelectrically active phase in the case of PVDF and its co-polymers. It has already been observed that aligning the filler inside the polymer matrix has led to the enhancement of piezoelectric as well as dielectric properties of the materials. Several techniques which can be used to perform filler alignment inside the polymer matrix are namely, injection moulding [124], doctor blading [125], vacuum-assisted assembly [126], and electric field-dependent alignment [127]. Injection moulding is primarily used to align fillers in the fibre-shaped template. When the dispersion of filler and polymer is injected through a nozzle, the filler tends to align along the direction of the injection. Electric field alignment is quite important in the field of science because it allows us to control the electric field in site-selective mode and have a remote effect on fillers. It can manipulate the filler orientation inside the matrix and allows anisotropic fillers to have physical contact [127]. The activity of filler alignment in composites is sometimes performed using dielectrophoretic techniques, which helps achieve higher performance in the  $d_{33}$  value. Pohl [128] found that the alignment of filler particles will occur inside the solvent due to the polarization forces produced by the alternating/inhomogeneous external electric field. A study by Zhang and his colleagues [114] implemented the dielectrophoresis technique for the alignment of ZnO filler in the PDMS matrix for the enhancement of the piezoelectric and dielectric properties of the composite. After dielectrophoresis, microscopic analysis revealed a chain-like structure of particles along the applied field direction, which showed an increase in permittivity with respect to filler concentration. Significant improvement in piezoelectric properties of the ZnO/PDMS composite was achieved through the dielectrophoretic process. When low concentrations of ceramic additives are randomly dispersed in a polymer matrix, a large difference between the two (ceramic and polymer) causes uneven distribution of electric field which results in poor properties of the composite. Whereas composites with 1–3 connectivity have better properties as compared to 0–3 connectivity but the cost of fabrication is much higher. Hence, dielectrophoretic activity can be implemented

to create composites which are in between 0–3 and 1–3 connectivity to achieve better properties [114]. Freeze casting is another method which is based on the directional freezing technique [127] used for creating links of fillers. A highly active strain sensor array was created using oriented PZT-PDMS composite materials where the authors invented porous PZT with a freeze-casting technique, and PDMS was impregnated into the aligned pores of PZT for composite manufacturing where the measured performance of highly active composite was 750 pC/N which is 110% higher than PZT ceramic alone [129].

**2.3.2.3 Properties of constituents** Constituents of the composites, namely ceramics and polymers, and their properties significantly affect the overall functioning of the composite materials. Among ceramics, perovskites show the best properties, and it is practical to probe their properties by variation in synthesis processes [18, 52, 130–134], doping with other elements or compounds [135, 136], and controlling their composition to achieve the MPB [41, 137, 138].

Researchers attempted to introduce dopants in prominent perovskite piezoelectric ceramics such as KNN, PZT, BT, and BNT, which resulted in the PPT effect [16, 44]. According to PPT theory, properties of KNN-based ceramics improved because of the shift in PPT points ( $T_{R-O}$  or  $T_{O-T}$ ) towards room temperature [45, 139], whereas in the case of PZT, the best performance was attained near the MPB. Enhanced piezoelectric performance for PZT was observed with Zr/Ti ratio equal to 52:48 because, at this composition, structural changes resulting from tetragonal to rhombohedral took place with the intermediate monoclinic phase [16, 140].

In the case of polymers, a higher percentage of crystallinity, the presence of aligned electric dipoles, and flexibility are favourable for better piezoelectric performance. In the case of PVDF, the  $\beta$ -phase has an all-trans configuration with an inherent net dipole moment; hence, it is favoured in piezoelectric applications [141]. Several researchers included filler addition into the PVDF polymer to increase the percentage of  $\beta$ -phase crystallization [142]. Odd-numbered nylons and PLA are other polymers showing inherent dipole present in their structures.

Both ceramic and polymer must be compatible for better dispersion and supportive interfacial interaction for composite fabrication. Some barriers to ceramic and polymer composites include phase

separation and agglomeration of ceramic additives inside the matrix. Fu and his colleagues [143] modulated the interface between the ceramic filler (BT) and polymer matrix (PVDF) by chemical modification of BT fillers with polyvinylpyrrolidone (PVP) which is low in toxicity. In accordance with the multi-layered core model, creating an intermediate layer tightly bonded to ceramic and polymer will improve interfacial compatibility since PVP and PVDF can interact. The authors demonstrated that PVP is effective for surface modification of BT ceramics, being the cause of the uniform dispersion of BT in PVDF matrix with enhanced properties and energy density 4.5 times higher than pure PVDF matrix.

**2.3.2.4 Poling conditions** Unpoled ferroelectric ceramics and polymers accommodate randomly oriented dipoles, resulting in net-zero electrical polarization. For piezoelectric properties, both ceramics and polymers require poling treatment under a strong DC field for dipole alignment along the electric field direction. For the composites, the electric field experienced by the ceramic particles during the poling treatment heavily depends on the dielectric properties of the polymer matrix used and is given by

$$E_c = \frac{3\epsilon_p}{\epsilon_c + 2\epsilon_p} E_o. \quad (3)$$

Here,  $\epsilon_p$  and  $\epsilon_c$  are the dielectric constant of polymer and ceramic, and  $E_o$  is the applied electric field, respectively; hence to enhance the piezoelectric performance of the composites, polymers like ferroelectric PVDF with comparatively high dielectric constants are used [96]. Domain engineering is doable in the case of ferroelectric ceramics with the help of electric poling. It is practicable to attain domain alignment in ceramics with the help of a high electric field of thousands of V/mm [42].

Wang and his group [144] showed a novel direction for improving Li-doped KNN ceramics' ferroelectric properties by manipulating the crystal's vacancy configuration. In short, the authors implemented domain engineering to increase the piezoelectric performance from 190 to 324 pC/N, which is accomplished through the externally applied electric field. The Li-KNN samples were re-poled after room temperature ageing treatment which improved  $d_{33}$  to a large extent. Figure 20a shows an ideal perovskite crystal structure, and after sintering treatment above

500 °C, A-site and O-site vacancies will be created. A-site vacancy will be created because of the volatile nature of alkaline components, and O-site vacancies will be there to maintain charge neutrality.

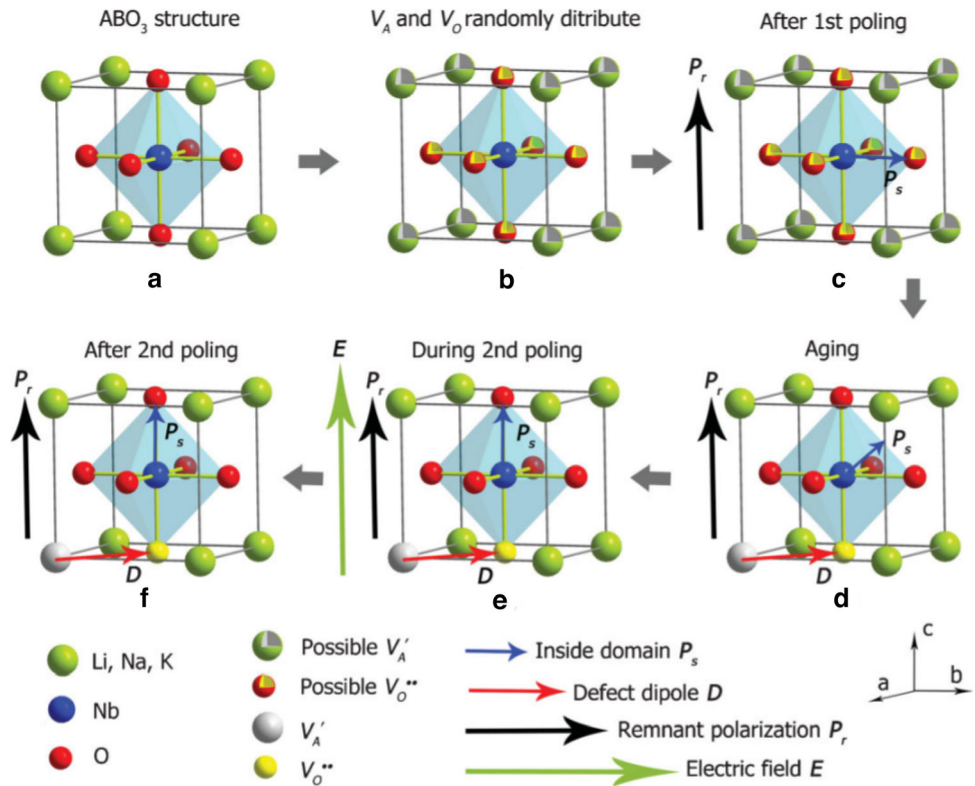
Above  $T_C$ , Li-KNN has a cubic structure; hence, the vacancies will distribute randomly in the crystal, as in Fig. 20b. After first poling, 90° domains of tetragonal phases are maintained at a high level and over a period of ageing, defect dipoles will attain a minimum energy level perpendicular to remnant polarization as shown in Fig. 20d. During the process, defect dipoles will affect spontaneous polarization through interactions which plays a deciding role in the value of  $d_{33}$  after re-poling. Both tetragonal and orthorhombic phases have comparable energies for samples with a composition close to 8 mol%, and  $T_{O-T}$  is close to room temperature. It is possible that spontaneous polarization can rotate in different modes of two phases easily. After re-poling,  $P_S$  can remain along the electric field direction even after removing the electric field, which eventually leads to the enhanced piezoelectric performance of the Li-KNN-based ceramic.

**2.3.2.5 Filler fraction** The volume fraction of ceramic filler strongly affects the dielectric and piezoelectric efficiency of the composite in several ways. Hence, optimizing the volume fraction of filler for better performance of the polymer–ceramic composite is crucial. Calculations of volume fraction inside the composite are done using SEM images of the cross-sectional area of the composite, where the formula for volume fraction is given as  $V_f = A_f/A$  ( $A_f$ : filler area,  $A$ : cross-sectional area) and the dielectric constant for a piezo-composite is predicted by Yamada et al. [96, 145] as

$$\epsilon_r = \epsilon_p \left[ 1 + \frac{n\phi(\epsilon_c - \epsilon_p)}{n\epsilon_p + (1 - \phi)(\epsilon_c - \epsilon_p)} \right]. \quad (4)$$

Here,  $\epsilon_c$  and  $\epsilon_p$  are the dielectric constants of the ceramic and polymer, respectively, with  $n$  as the aspect ratio of ceramic and  $\phi$  as the volume fraction. Khaliq and his team [146] demonstrated that the dielectric constant value of ceramic has more significant role than the piezoelectric coefficient in the determination of the piezoelectric properties of the composite. It is observed that the effective electric field experienced by the ceramic filler is inversely proportional to their dielectric constant value; hence

**Fig. 20** Saturation Polarization and remnant polarization alignment mechanism responsible for large piezoelectric performance after ageing and re-poling of the material. Adapted/Re-used with authorization from citation [144]. Copyright 2010 Wiley



it is vital to consider the dielectric and piezoelectric properties of filler material. Jayendiran and Arockiarajan [147] modelled the dielectric and piezoelectric response of 1–3 type piezo-composites (PZT5A1 fibres and epoxy matrix) and compared the theoretical predictions of stiffness, coupling factor, and piezoelectric constant with the experimental results. It is observed that the given model successfully predicted the characteristics of non-linear coupled response for the material.

**2.3.2.6 Temperature** In the composite fabrication process, the calcination temperature of ceramic and glass transition temperature of polymer plays a significant role in finalizing the composite [96, 148].

Perovskite ceramics exist in several phases, namely cubic, rhombohedral, tetragonal, and orthorhombic, whereas it is feasible to probe their geometrical phases through the variation of temperature and composition. In review, Li et al. [42] re-examined the phase structure of KNN, showing phase transitions with temperature variation, as shown in Fig. 21.

Calcination and sintering temperatures are essential in deciding the piezoelectric properties of the synthesized ceramic powder because these processes significantly affect their grain size and density.

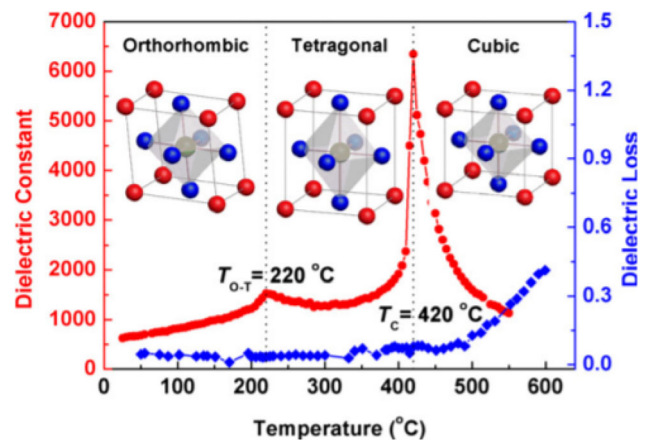
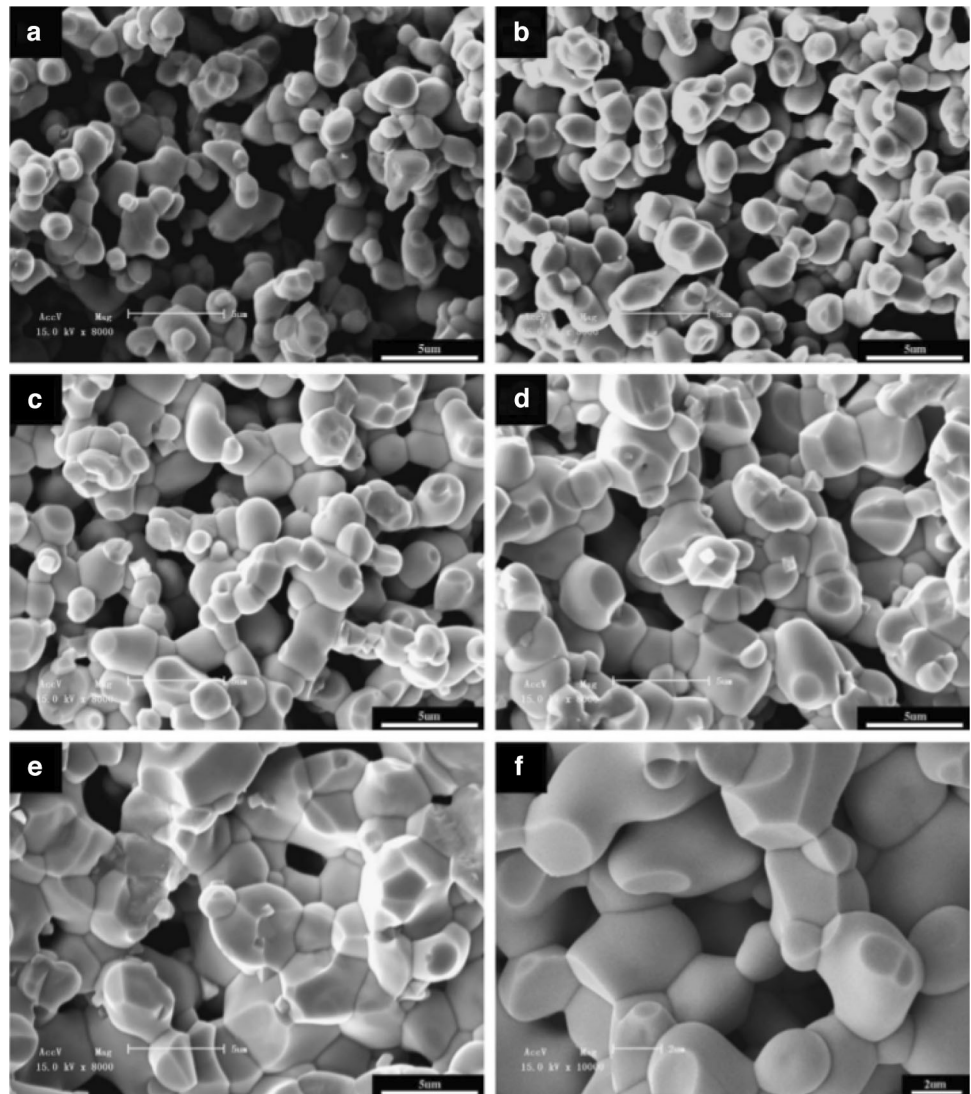


**Fig. 21** Polymorphic phase transition temperatures for KNN ceramic in temperature range 0 °C–600 °C. Adapted/Re-used with authorization from citation [16]. Copyright 2019 Elsevier

Calcination removes the volatile substances from the ceramic, and sintering is mainly used to densify polycrystalline ceramics. Yang and his colleagues [149] analysed the results of sintering porous PZT at different temperatures on the microstructure and piezoelectric properties. It is observed that porosity and grain size are crucial factors in determining the material's overall properties. Authors reported that with the increase in the sintering temperature, a

**Fig. 22** Effect of sintering temperature on porous PZT-based ceramic. **a** 1150 °C, **b** 1175 °C, **c** 1200 °C, **d** 1225 °C, **e** 1250 °C. Adapted/Re-used with authorization from citation [149]. Copyright 2010 Elsevier



decline in porosity, whereas an increase in grain size was observed, which led to the possibility of optimum control of both factors for the best piezoelectric properties. The morphology of pores of PZT at different sintering temperatures is shown in Fig. 22.

Among lead-free piezoceramics, Yoo [150] analysed the effect of sintering temperature on ferroelectric, piezoelectric, and dielectric properties of KNN-based ceramic synthesized using a conventional solid-state route. Obtained observations provide an insight that 1040 °C is an optimal temperature for sintering in order to get a high Curie temperature (225 °C) and piezoelectric performance (343 pC/N) with high  $K_p$  (0.52).

Several other studies related to various sintering processes were conducted [151, 152]. Spark plasma sintering, two-step sintering, and normal sintering

treatments were given to BCZT to obtain grains of different sizes. As grain size decreases, both  $T_c$  and  $T_{T-R}$  shift towards higher value and excellent piezoelectric performance was observed for grain sizes more than 10  $\mu\text{m}$  [153].

Calcination also impacts the piezoelectric properties and morphology of the material. Anh and Koh [154] varied the calcination temperature from 720 to 840 °C and optimized it to obtain an enhanced piezoelectric coefficient from 388 to 440 pC/N. The impact of poling temperature on the piezoelectric properties of ceramics is discussed in detail in Wan et al. [155] and Yao et al. [156]. It is found that poling performed above room temperatures gives a better piezoelectric performance.

Hafner and group [157] discussed the temperature effect on piezoelectric properties of P(VDF<sub>70</sub>-TrFE<sub>30</sub>).



It is observed that the piezoelectric constant increases by 150% when the temperature is increased from 25 to 80 °C, and the authors concluded that the increment in piezoelectric properties of the polymer is linked to the temperature dependence of its elastic modulus and polarization. Sherman et al. [158] discussed the effect of temperature on piezoelectric properties of pre-poled PVDF, where no degradation was observed in the piezoelectric constant for temperatures below 100 °C.

### 2.3.3 Fabrication

Various bulk fabrication methods are available, such as dice and fill, Solvent casting, 3D printing, 4D printing, arrange and fill, injection moulding, and dielectrophoresis. [111–115, 159] They largely influence the piezoelectric performance of the composites and are used mainly for targeted functions [160–162].

Alluri et al. [163] proposed a BT/PDMS-based composite using the solvent casting technique, which is lightweight, flexible, eco-friendly, and a potential candidate as a piezoelectric energy harvester with an output voltage of 55.9 V (Fig. 23) under the human foot force. The BT particles synthesized with molten salt technique and composite films were fabricated with simple solvent casting technique with electrical poling at 8 kV for 24 h at room temperature. The nanogenerator performance was evaluated with a load of 2 N and obtained peak-to-peak voltage of 126.3 V and current density of 77.6  $\mu\text{A}/\text{cm}^2$ . The role

of PDMS in energy generation and rolling capability was successfully demonstrated.

Piezoelectric composite with high-aspect-ratio micro-rods were developed using the dice and fill method with LKNNT-AS-M piezoelectric ceramic [111]. Dice and fill is a facile method for fabricating 1–3 piezo-composites, and  $\text{AgSbO}_3$ ,  $\text{MnO}_2$ , and Ta-doped KNN ceramic used in this work showed a much better value of  $d_{33} = 287 \text{ pC}/\text{N}$ . The groove cutting and dicing were performed with an automatic dicing machine ZSH-3, in which a diamond dicing saw can rotate at a speed of up to 30,000 rpm. The schematics of the modified dice and fill method implemented to fabricate piezo-composite are illustrated in Fig. 24.

Bodkhe and his team [112] designed nanocomposite using a 3D printing technique to attain piezoelectric performance comparable to commercial PVDF without the electric poling treatment. Experimentally, authors achieved the combination of printability and piezoelectric properties close to the commercial PVDF without the requirement of poling. The nanocomposite formulation was achieved using three different processes, ball milling, extrusion mixing, and sonication, to include different concentrations of BT nanoparticles into the PVDF matrix, which will eventually support the nucleation process  $\beta$ -phase in PVDF for better performance. An extensive study of the nanocomposite formulations prepared concluded that the best properties were achieved with the solvent evaporation-assisted 3D printing of 10 wt% BT nanoparticles ball-milled with

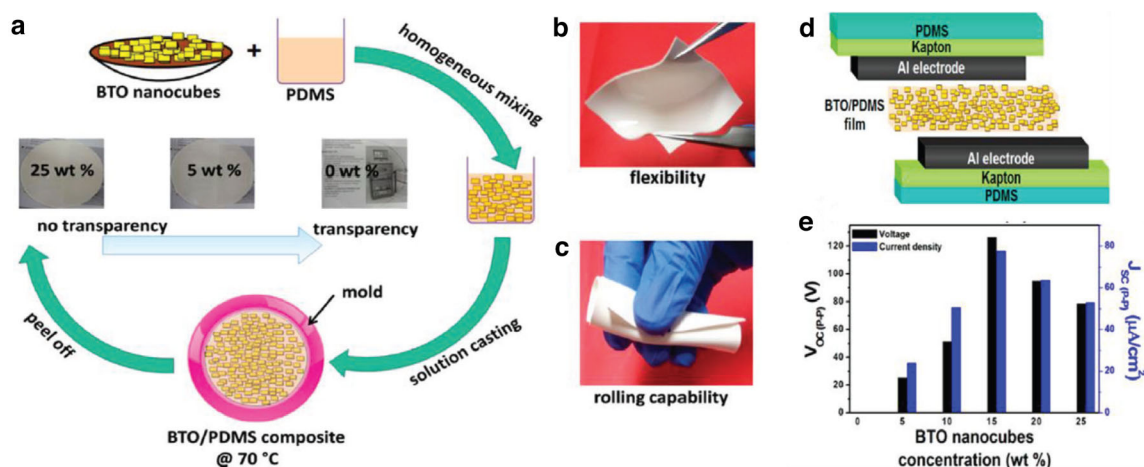
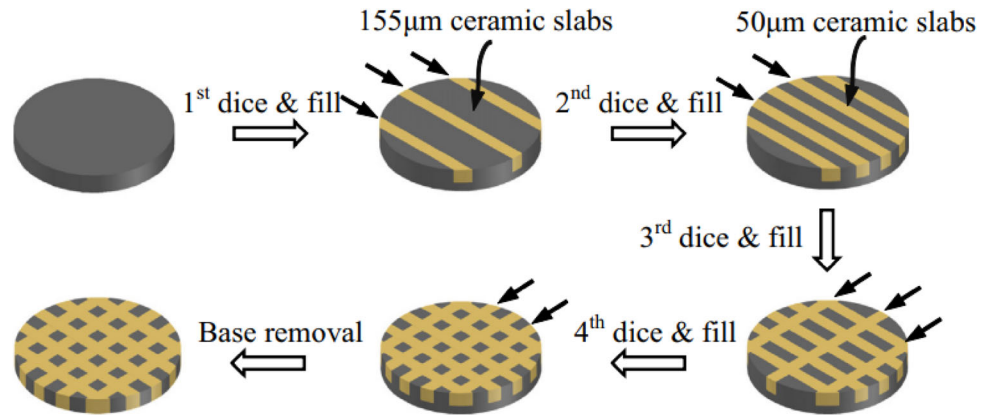


**Fig. 23** Preparation and performance of BT/PDMS nanocomposite (a) synthesis procedure, (b) flexibility visuals, (c) rolling capability, (d) fabrication of generator, (e) performance

concerning BT concentration. Adapted/Re-used with authorization from citation [163]. Copyright 2017 American Chemical Society

**Fig. 24** Modified dice and fill process for fabricating 1–3 composites with high-aspect-ratio ceramic pillars. Adapted/ Re-used with authorization from citation [111]. Copyright 2016 American Chemical Society

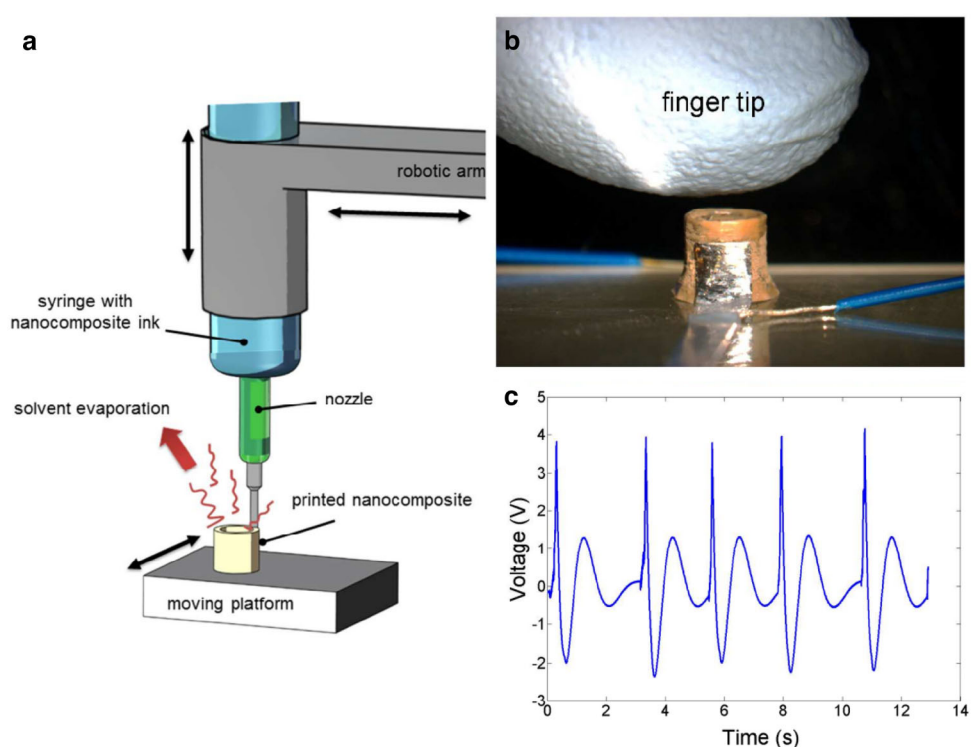


PVDF due to a large percentage increase in  $\beta$ -phase of PVDF (Fig. 25).

Over the past decade, many 3D printing-based piezoelectric materials have been invented; however, the current 3D printing technology in the piezoelectric domain is still in its infancy because they possess challenges such as weak electromechanical coupling constant and poor mechanical properties; also, the maximum value of piezoelectric constant reported for 3D printed piezoelectric PZT-based composite is 110 pC/N [164]. Li et al. adopted the nacre architecture to enhance its mechanical strength, where alternate

layers of soft ferroelectric material and hard electrodes were directly printed with in situ poling through fused deposition modelling (FDM). The soft ferroelectric material consists of lead-free high  $T_C$  material, Li–KNN blended with PVDF–HFP, whereas the electrode material contains bio-friendly printable polymer PLA and conductive carbon black. The invented ferroelectric metamaterial showed a piezoelectric coefficient comparable to that of ceramics and bone-like mechanical strength with Li–KNN, which is the key material for strong interfacial binding (Fig. 26) [164].

**Fig. 25** **a** Schematics of solvent evaporation-assisted 3D printing for PVDF nanocomposites, **b** 3D cylindrical sensor, **c** piezoelectric output of the fabricated sensor. Adapted/ Re-used with authorization from citation [112]. Copyright 2017 American Chemical Society



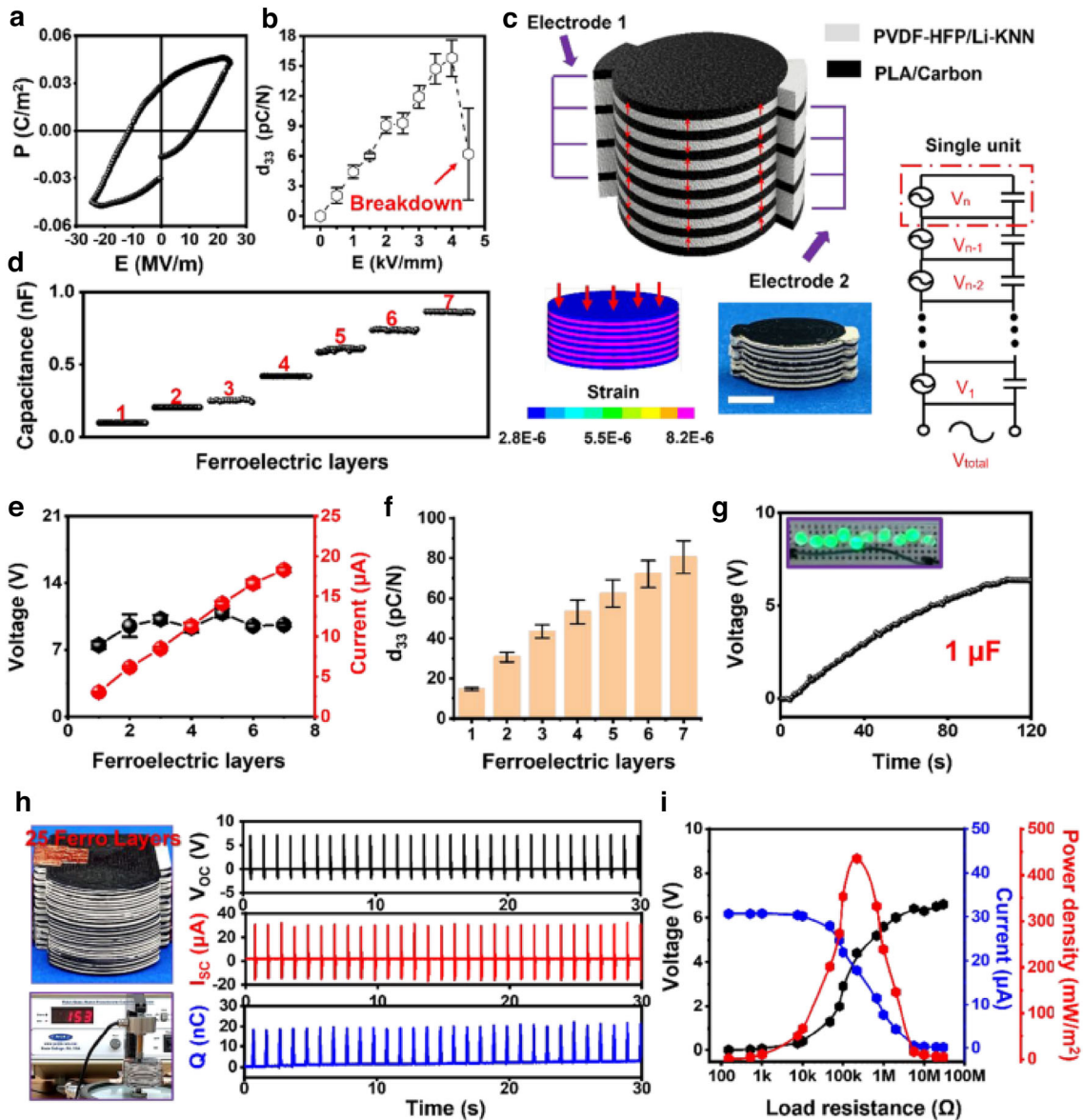


**Fig. 26** Piezoelectric study of the printed lamellar metamaterial. **a** ferroelectric characteristic of the single layer, **b** piezoelectric coefficient of single layer with respect to poling electric field, **c** schematics of the ferroelectric metamaterial with electrode configuration and alternating dipoles, **d** capacitance of the material with respect to ferroelectric layers, **e** output current and output voltage of ferroelectric print as a function of ferroelectric layers, **f** piezoelectric coefficient of the metamaterial with respect to

ferroelectric layers, **g** Voltage curve for 1  $\mu\text{F}$  capacitor charged via 7-layered ferroelectric print, **h** twenty-five ferroelectric layer material and its  $d_{33}$  measurement photograph along with output electrical characteristics, **i** voltage (blue), current (black), and power (red) outputs from the print as a function of different load resistances. Adapted/Re-used with authorization from citation [164]. Copyright 2021 American Chemical Society (Color figure online)

### 3 Piezoelectric nanogenerators

In today’s era of nanotechnology, mechanical energy harvesting technology is developing at a much faster pace to support the urgent need for power for multifunctional microelectronic and nanoelectronic devices. Piezoelectric nanogenerators are quite

popular among researchers due to their ability to harvest freely available ambient mechanical energy in extremely harsh environments. Since 2006 when the first piezoelectric nanogenerator was invented, researchers successfully increased the output performance from 8 mV in 2006 to 250 V at present in terms of voltage [165]. But in terms of short-circuit current,

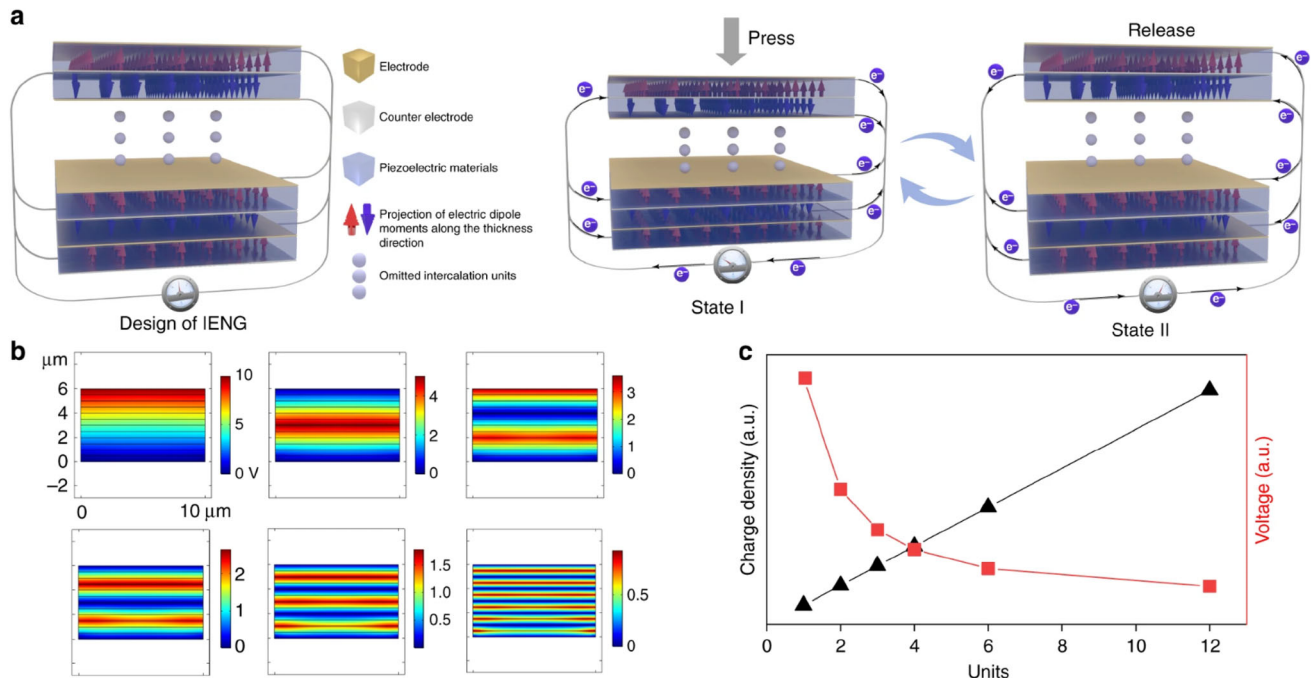


**Fig. 27** **a** 3D representation of intercalation electrode in which piezoelectric material is sandwiched, creating a stacked structure. Blue and red arrows represent the electric dipole orientation along the thickness. **b** Upon applied pressure, the distribution of piezoelectric potential in different units when the same layer is

the progress is still in the range of  $\mu\text{A}$ , which is very low for practical applications [166]. Many successful attempts were made to improve the overall power density output of piezoelectric nanogenerators. Hu and team [167] concisely explained the recently developed strategies to improve the performance of piezoelectric nanogenerators: use of piezoelectric materials with different crystal structures, use of different morphologies of the material, selection of proper substrates and chemical modifications via elemental doping. As per the authors' investigation, it is possible to improve the power output of a piezoelectric nanogenerator in the range of mW by elemental doping with appropriate substrate selection [167]. Initially, Park et al. fabricated PZT thin film-based nanogenerator with intermediate electrodes and connected several PZT films to record the high current density of  $150 \mu\text{A}/\text{cm}^2$  [168]. Recently, Gu et al. proposed a way to enhance the output current density in a piezoelectric nanogenerator with the help of a 3D intercalation electrode. With the creation of several boundary interfaces between the piezoelectric material, increments in the surface polarization of charges occurred, which eventually

divided into 1, 2, 3, 4, 6, and 12 units with the help of intercalation electrodes. **c** Corresponding output characteristics showing charge density and voltage variation. Adapted/Re-used with authorization from citation [165]. Copyright 2020 Springer Nature (Color figure online)

led to the increased current density and current output ( $290 \mu\text{A}/\text{cm}^2$  and  $320 \mu\text{A}$ ). The resulting integrated electrode nanogenerator can light up 100 commercial LEDs and can charge one  $\mu\text{F}$  capacitor to 8 V in only 21 cycles [165]. The schematic for the developed integrated electrode nanogenerator is provided in Fig. 27. However, it is important to figure out the working principles and the mathematical formulation of the nanogenerator for improving the performance, as discussed in the subsequent section.

To improve the performance of nanogenerators, it is important to figure out the working principles and the mathematical formulation of the nanogenerator as discussed in the subsequent sections.

### 3.1 Working and formulation of nanogenerator

In nanogenerators, the transformation of mechanical oscillations into electrical polarization takes place with added advantages such as enhanced energy density and flexibility of integration in a system. Incorporating ceramic nanofillers into flexible polymers allows the composites to be used as generators

with low input frequencies and large excitation amplitude without compromising power output [70]. Formulation for calculating performance metrics of a nanogenerator is quite straightforward as given below. For any nanogenerator developed, the generated charge across the opposite faces of materials can be calculated using

$$Q = d_{33} \times A \times \Delta\sigma, \quad (5)$$

where  $Q$  is the charge,  $d_{33}$  is the piezoelectric coefficient,  $A$  is the surface area, and  $\Delta\sigma$  is the applied mechanical stress [22]. In open-circuit condition, impedance is infinite, and hence  $Q = CV$  is applicable here, and the open-circuit voltage can be calculated using

$$C = A \times \frac{\epsilon_{33}^T}{h} \quad (6)$$

$$V = \frac{d_{33}}{\epsilon_{33}^T} \times h \times \Delta\sigma. \quad (7)$$

Here, “ $h$ ” is the material thickness and “ $\epsilon_{33}^T$ ” is the dielectric permittivity at constant stress in 33-mode [22],  $C$  is capacitance and  $V$  is voltage.  $E = \frac{1}{2}CV^2$  gives the energy generated due to the applied electric field. To calculate the short-circuit current, it is workable using above equation and  $I = \frac{\Delta Q}{\Delta t}$ ,

$$I = d_{33} \times A \times \frac{\Delta\sigma}{\Delta t} \quad (8)$$

short-circuit current and open-circuit voltage calculations are primarily performed in energy harvesting applications; however, it is difficult to obtain effective power output value under the given constraints. In short-circuit mode, there will not be any potential difference; in open-circuit mode, there will not be any current to calculate the effective power. To calculate the instantaneous power density,  $P = \frac{V^2}{RA}$  is generally used, where  $A$  is the surface area of electrodes and  $V$  is the potential difference across load ( $R$ ) [22].

The atmosphere contains a mixture of various gases such as oxygen, nitrogen, and water vapour. Water vapour and oxygen can affect the piezoceramic materials and hence can affect the performance of nanogenerators. Water may penetrate through the polymer packaging and degrade the materials’ piezoelectric and dielectric properties, reducing the nanogenerator’s performance, whether in liquid form or vapour form. The amount of degradation depends upon the wettability of the surface and the amount of

water present [169]. Since nanogenerators have a large surface-to-volume ratio, they are prone to the adsorption of various elements from the atmosphere including moisture and oxygen [170].

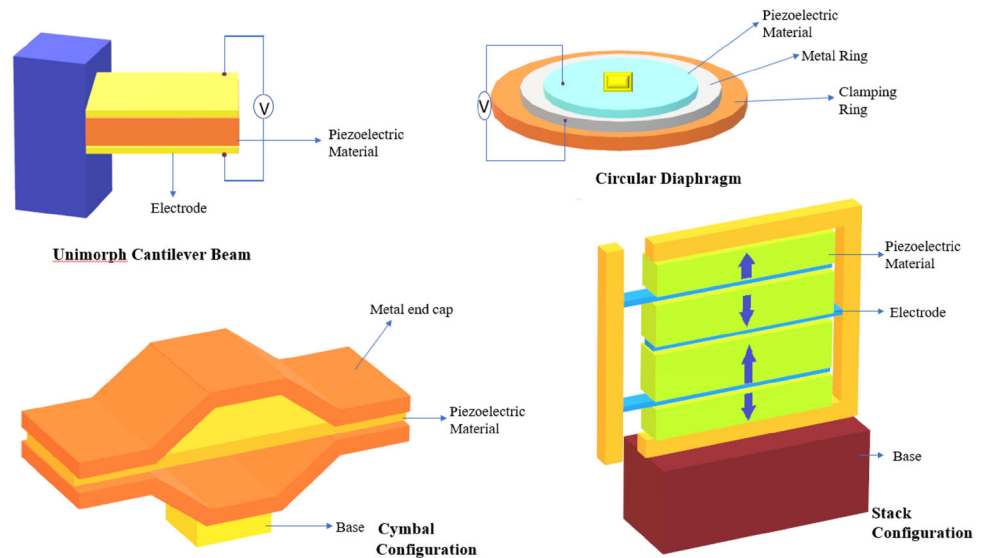
Chowdhury and his group [17] classified nanogenerators based on the different dimensionality of piezoceramics as 0D, 1D, 2D, and 3D. Among the four classifications, nanogenerators based on 0D piezoceramics are most famous among researchers because of advantages like higher surface area and easy preparation compared to other dimensions, and they are composed of nanoparticles isolated from each other. In the case of 1D structures, piezoelectric nanostructures have one dimension less than 100 nm and a length more than micrometers; piezoelectric nanowires are primarily used in self-powered nanogenerators. 2D structures include films or coatings with thickness in the range of nanometers, whereas 3D piezoelectric nanostructures comprise piezoelectric powders, fibrous and multi-layered materials in which lower dimension structures are in close contact with each other. A detailed discussion on the classification of nanogenerators based on dimensionality is also discussed in [20].

### 3.2 Applications of nanogenerator

Now, it is crucial to explore the various applications of nanogenerators in different sectors such as transport, smart homes, defence, automotive, and electronics industries. Nanogenerators are available in different configurations in which bimorph cantilever geometry is most popular among the research community because of its simplicity in the fabrication process and enhanced performance compared to unimorph cantilever [10]. Other practical application-based configurations are shown in Fig. 28.

Vibrations-based energy harvesters are critical for implantable devices because they help in integration, sealing, and mechanical reliability. Deterre et al. [171] demonstrated the fabrication and several experiments of a piezoelectric energy nanogenerator which operates on blood pressure vibrations in the cardiac environment. They produced  $3 \mu\text{J}/\text{cm}^3/\text{heartbeat}$  power and a transduction efficiency of 0.57% at 1.5 Hz. With smart adapted electronic circuits, it is predicted that ten-fold power output is attainable. The responsive environments group at MIT media invented an unobtrusive device that scavenges electrical energy from the shoe [172]. They mounted a

**Fig. 28** Different types of nanogenerator configurations implemented for piezoelectric energy harvesting application



PVDF-based piezoelectric nanogenerator into the shoe with a conditioning circuit. It is viable to use a piezoelectric nanogenerator as a power generation device and a pressure sensor for external activity recognition [173–175].

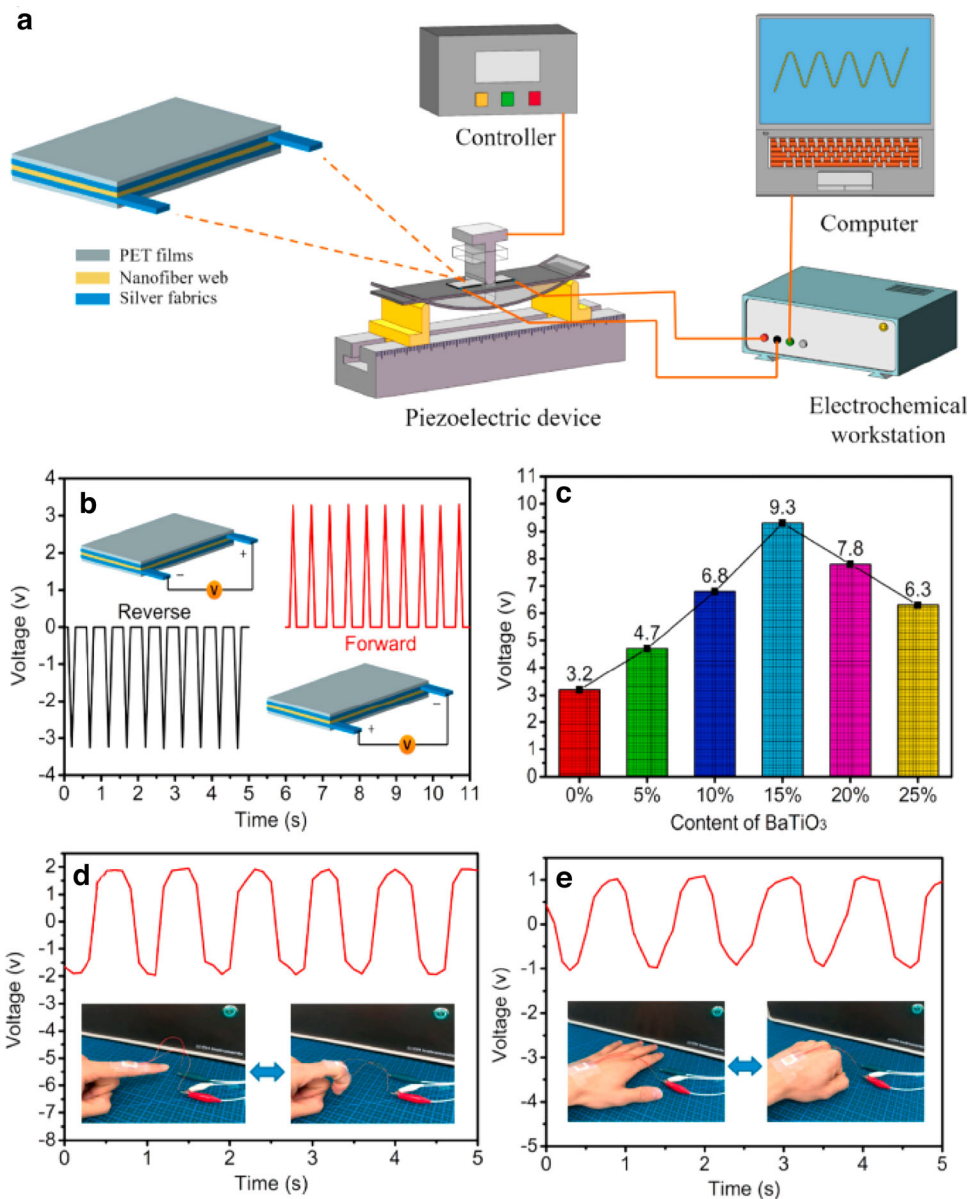
Timely detection of structural damage is an important task in the structural health monitoring domain. Structural health monitoring is a process of observing and evaluating the structural integrity and real-time performance of various composites. Piezoelectric materials have two-way benefits, which include sensing as well as energy harvesting making them potential self-energized active sensors for structural health monitoring. Yuan and team [176] developed Polyacrylonitrile and BT-based nanofiber membrane sensor for real-time structural evaluation in composites. Figure 29a and b shows the schematics of the connection and voltage output characteristics of the sensor. Pure polyacrylonitrile film produced a voltage output of 3.2 V, whereas the addition of 15% BT demonstrated the highest value of voltage equal to 9.3 V (Fig. 29c). Here, Fig. 29d and e shows that when a simple sensor unit is connected to the detector with the help of wires and pasted on the finger and the fist, it is able to produce a voltage output of 1.9 V when strain is induced due to finger movement and 1.0 V when very small pressure is generated due to action of clenching and relaxing of the fist.

Deng et al. [177] found an interesting real-time application in the interactive human–machine interface domain in which they fabricated a self-sufficient

ZnO/PVDF nanofibers-based piezoelectric sensor for pressure sensing and monitoring the bending motions of a robotic arm. Deng and team successfully achieved the pressing and bending sensitivity of  $0.333 \text{ V kPa}^{-1}$  (response time = 16 ms) and  $4.4 \text{ mV/deg}$  (response time = 76 ms) and implemented a self-powered, wireless gesture control system. Park et al. [178] addressed an important real-time technology for detecting the early onset of cardiovascular disease. The authors successfully demonstrated continuous monitoring of the pulse with a PZT-based piezoelectric pressure sensor. The PZT thin film was prepared via the sol–gel method, which demonstrated a sensitivity of  $0.018 \text{ kPa}^{-1}$ , a response time of 60 ms and good mechanical stability. Figure 30 shows the schematics of the arterial pulse monitoring sensor.

Self-powered and portable devices are critical candidates for future energy applications because they can efficiently function without any external source or agency, and several attempts have already been made in this direction [179, 180]. An eco-friendly, flexible, self-powered fluid velocity sensor, and piezoelectric nanogenerator was manufactured based on  $\text{BaTi}_{1-x}\text{Zr}_x\text{O}_3$  nanocubes with PVDF as a matrix [181]. Observations showed that the piezoelectric potential generation in the composite primarily depends on the periodic frequency of the applied stress. Composites showed a small piezoelectric response at a load of 11 N with a low periodic frequency of 3 Hz because of the internal capacitance or the beginning of piezoelectric behaviour, and it

**Fig. 29** **a** Detailed assembly of circuit elements for energy transformation testing. **b** The voltage output from pure polyacrylonitrile (PAN) film for forward and reverse connections, **c** the voltage output of PAN film for different amounts of BT content, **d** the voltage output from the movement of a finger, **e** the Voltage output from the movement of a fist. Adapted/ Re-used with authorization from citation [176]. Copyright 2021 Elsevier

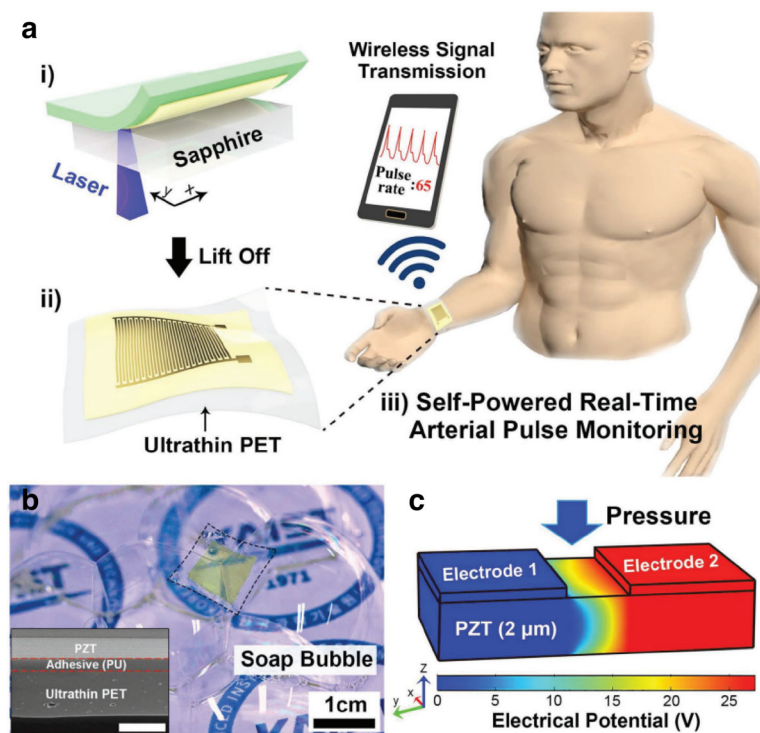


reaches a maximum for 21 Hz, which confirms the orientation of electric dipoles in the composite due to stress-caused poling effect. The prepared flexible piezoelectric nanogenerator (PNG) is implemented as an active pressure sensor to calculate liquid velocity at the exit of the pipe because of its high sensitivity and conformability. Fabricated PNG3 (for  $x = 0.1$  in  $\text{BaTi}_{1-x}\text{Zr}_x\text{O}_3$ ) was attached perpendicular to the flow of water, and the electrical output of assembly was noted with the water ON and water OFF conditions. The mechanism involved in working the velocity sensor is similar to that of periodic pressure acting on the sensor due to the water flow through the outlet. The PNG3 measured an output potential difference

and current of 26 mV and 8 nA at the water velocity of 31.43 m/s (water ON) and 80 mV and 10 nA at the water flow OFF condition. Upon increment of water velocity, a corresponding increment in the output voltage and current was observed for PNG3 (water ON condition). To showcase the self-powering capacity of the PNG sensor, several measurements were performed which showed the ability to store the alternating energy from PNG in the capacitor and that it can be subsequently used for an implantable device and self-powered sensors (Fig. 31) [181].

He et al. [180] invented a self-sustainable device that specifically integrates the nanogenerator and

**Fig. 30** **a** Schematics of the fabrication of a self-sustainable pressure sensor. PZT film is coated on sapphire paper, which is then transferred onto PET substrate and then finally attaching it to the human wrist to monitor the pulse signal via smart-phone **(b)** PZT film on PET substrate floating on soap bubble (inset shows the cross-sectional SEM image) **(c)** Simulated piezoelectric potential over the PZT film under vertical applied pressure. Adapted/Re-used with authorization from citation [178]. Copyright 2017 Wiley



storage device to store the scavenged energy from the harvester for a sustainable power supply (Fig. 32). Recently developed piezoelectric nanogenerators were chosen for energy scavenging applications to convert ambient mechanical energy input into electrical energy. For energy storage purposes, supercapacitors were chosen because of unique advantages such as short charging time and high energy density, long life, and being environmentally friendly. The testing of piezoelectric nanogenerator (PENG) for energy harvesting from the human movement was carried out at various locations (Fig. 33), such as the knee joint, elbow joint, and under the foot.

Recently, much development has been happening in piezoelectric wearable and implantable nanotechnology, which enabled personalized care from fitness to health monitoring. These devices can be thought of as an interface between humans and technology. Although several challenges need to be addressed to achieve sustainable growth in this domain, such as high flexibility and stretchability are essential for wearable devices and biocompatibility to care for health and wellness. It is also essential to meet the challenge of designing a device compatible with a diverse range of consumers. Another challenge that needs to be addressed is that energy harvesters require a resonance environment essential for the

best performance, and changes in those conditions can drastically reduce the device's performance. Although there are many challenges, they allow us for continuous, real-time data transmission enabling various sensing and monitoring applications, which is the need to revolutionize humans' daily lives and healthcare. Advances are going on in the field of nanogenerators, and some of the energy harvesting devices, along with their specifications, are mentioned in Table 3.

Aside from energy harvesting from nanogenerators, simultaneous storage of produced energy can improve the overall flexibility of energy usage, enabling us to use electronic devices at any time and at any location. From the existing technology perspective, electrochemical energy storage is the best suitable option with Li-ion batteries. In the electrochemical mechanism of energy storage, externally applied voltage causes a reaction between the anode and cathode inside the cell resulting in the migration of ions. So, in a nutshell, first mechanical energy gets converted into electrical energy, which is then stored as chemical energy inside the cell [182]. Wang et al. [183] demonstrated the first-ever self-charging power cell with a novel mechanism which can directly transform mechanical energy into the stored chemical energy inside the cell. To realize the hybridization of



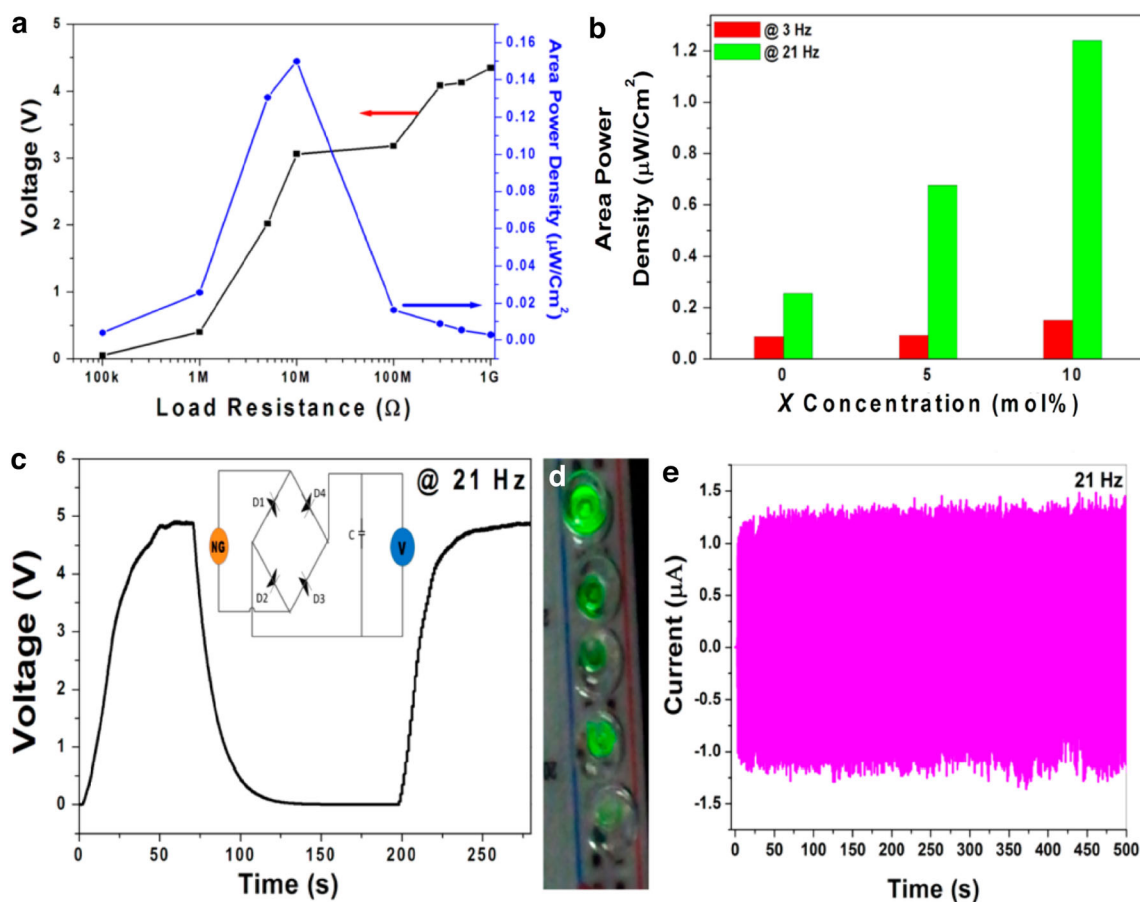


**Fig. 31** **a** Voltage output and area power density of PNG3 at 3 Hz with respect to variable load, **b** comparison of the area power density of PNG1, PNG2, and PNG3 at two different frequencies of mechanical load at a resistance of 10 M $\Omega$ , **c** potential differences across storage capacitor (1  $\mu\text{F}$ ) when charged with PNG3 at 21 Hz,

**d** five LEDs can be light up by rectified piezoelectric potential from PNG3, **e** output current of PNG3. Adapted/Re-used with authorization from citation [181]. Copyright 2015 American Chemical Society

two mechanisms, authors replaced the conventional separator between the cathode (LiCoO<sub>2</sub>) and anode (TiO<sub>2</sub>) in batteries with PVDF film. The device is fabricated as a completely sealed stainless-steel coin cell filled with electrolyte (LiPF<sub>6</sub>), as shown in Fig. 34. When a compressive force acts on the cell, PVDF film will induce piezo-potential which will, in turn, create an electric field resulting in the movement of Li ions in the electrolyte towards anode through the PVDF separator film. Reduction in Li<sup>+</sup> ions at the cathode will cause an imbalance in the equilibrium reaction at the cathode, and Li<sup>+</sup> ions deintercalation from LiCoO<sub>2</sub> and leave excess electrons at the cathode end. Migrated Li<sup>+</sup> ions at the anode will react with TiO<sub>2</sub> forming Li<sub>x</sub>TiO<sub>2</sub> and leaving positive charges at the anode, and this process continues to charge the cell.

When compressive force was applied to the cell assembly ( $\sim 2.3$  Hz), the voltage increased from 327

to 395 mV in 240 s and discharged back to its initial value of 327 mV once the self-charging was over with discharge current of 1  $\mu\text{A}$  (for 130 s). Schematics of the assembly, internal charging dynamics, and performance metrics are depicted in Fig. 35. With a similar principle, Ramadoss et al. [184] demonstrated piezoelectric driven self-charging supercapacitor power cell based on ZnO/PVDF composite and MnO<sub>2</sub>-based electrodes showing charging efficiency of 100 mV for 300 s.

Chary and his team [71] created KNN–Sb and PVDF–HFP-based nanofibers for thermal management in heat pipes. A flexible nanogenerator was invented using the composite of nanofibers prepared via hydrothermally synthesized Sb-doped KNN and PVDF–HFP with electrospinning. Crystal structure and morphology analysis revealed the formation of orthorhombic crystal structure with two symmetric

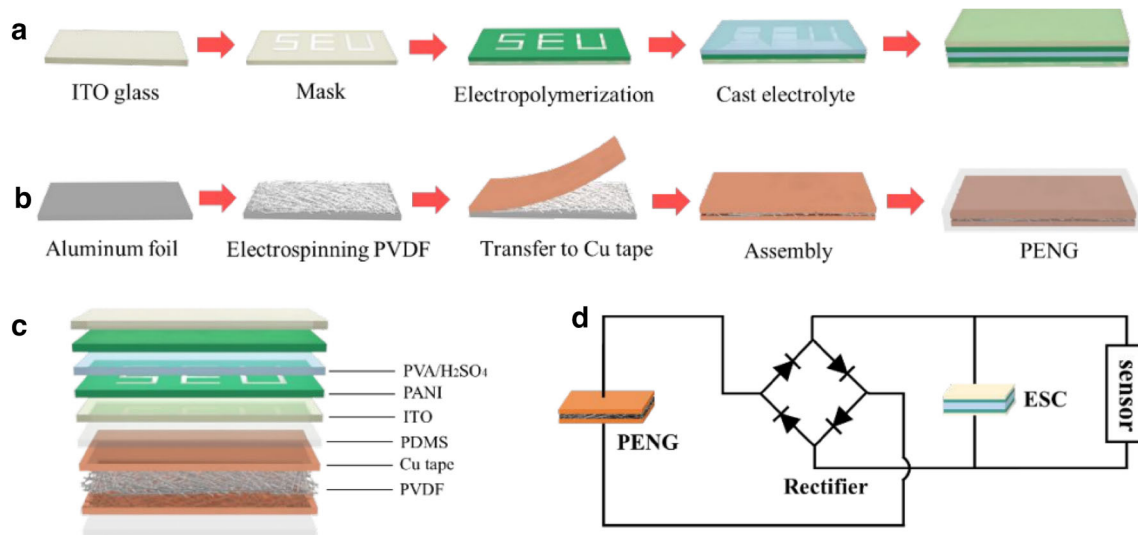
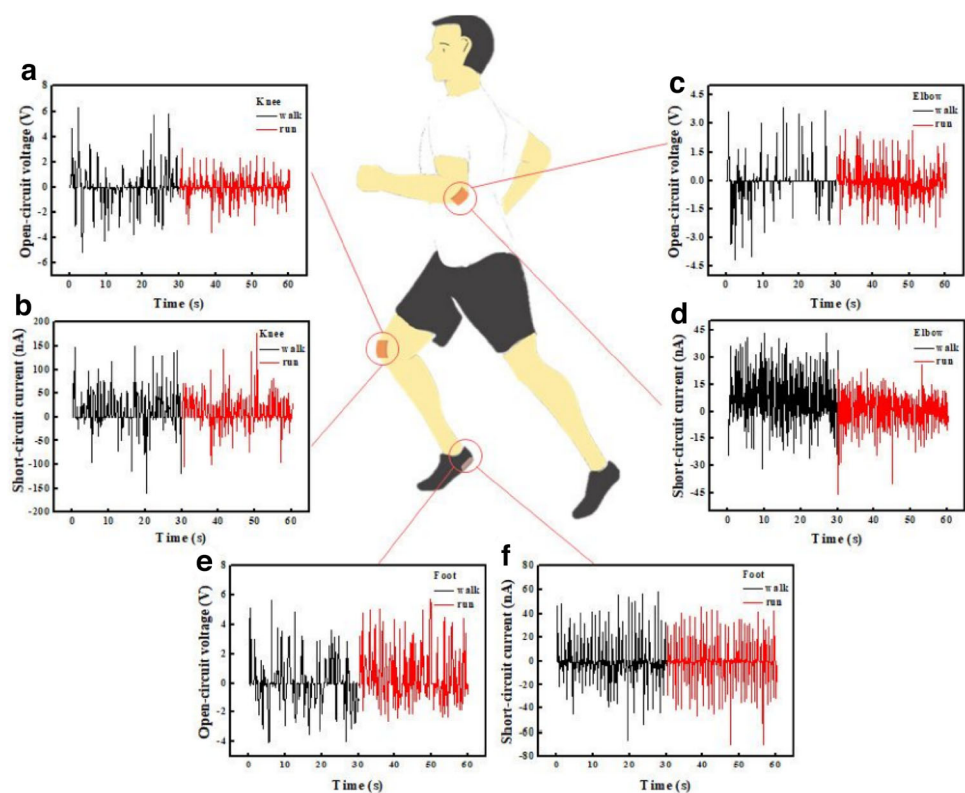


**Fig. 32** Schematics of electrochromic supercapacitor. **a** fabrication of patterned ESC, **b** fabrication of wearable PENG, **c** visuals of self-sustainable ESC in a layer-by-layer structure,

**d** equivalent circuit of self-powered patterned ESC. Adapted/Re-used with authorization from citation [180]. Copyright 2019 American Chemical Society

**Fig. 33** Testing of PENG for energy harvesting from human movement (**a, b**)  $V_{OC}$  and  $I_{SC}$  of PENG at knee joint, (**c, d**)  $V_{OC}$  and  $I_{SC}$  of PENG at elbow joint, (**e, f**)  $V_{OC}$  and  $I_{SC}$  of PENG under the foot. Adapted/Re-used with authorization from citation [180]. Copyright 2019 American Chemical Society



configurations (*Amm2* and *Bmm2*), where elemental doping resulted in a minor shift in the diffraction peaks of KNN slightly towards the greater angle values with lattice shrinkage and distortion due to size difference in Sb and Nb. XRD analysis of KNNsSb/PVDF-HFP revealed the peak at 20.4°,

which confirmed the formation of  $\beta$ -phase. Calculation of peak intensity ratios from XRD patterns of both PVDF-HFP and KNNsSb/PVDF-HFP strongly suggested that KNN-Sb filler acted as a nucleating agent for  $\beta$ -phase.

**Table 3** Summary of recently developed piezoelectric composites with their performance for nanogenerator applications

Sr. No	Polymer matrix	Filler	Synthesis techniques	Performance	Application	Reference
1	PVDF-HFP	GQD	Chemical exfoliation/spin coating	$V_o = 6 \text{ V}$ , $I_S = 25 \text{ nA}$	Flexible nanogenerator	[185]
2	PVDF	Fe-RGO	Solvent casting	$V_o = 5.1 \text{ V}$ , $I_S = 254 \text{ nA}$	Flexible nanogenerator	[186]
3	PDMS	BT	Solid state/freeze drying	$V_o = 39 \text{ V}$ , $I_S = 2900 \text{ nA}$ , $P = 24,200 \text{ nW}$	Tactile imitation application	[187]
4	PVDF-HFP	KNN	Hydrothermal/electrospinning	$V_o = 4.9 \text{ V}$ , $I_S = 250 \text{ nA}$ , $P = 780 \text{ nW}$	Thermal heat pipes	[71]
5	PVDF	ZF	Hydrothermal/solvent casting	$V_o = 39.1 \text{ V}$ , Energy storage = $7.68 \text{ mJ cm}^{-3}$	Flexible energy harvesters	[188]
6	PVDF	KNN/CNT	Hydrothermal/electrospinning	$V_o = 23.24 \text{ V}$ , $I_S = 900 \text{ nA}$ , $P = 52.29 \text{ } \mu\text{W cm}^{-2}$	Nanogenerator	[189]
7	PVDF	NN/RGO	Hydrothermal/drop casting	$V_o = 2.16 \text{ V}$ , $I_S = 383 \text{ nA}$	Nanogenerator	[190]
8	PVDF-HFP	BT/h-BN	Solvent casting	$V_o = 2.4 \text{ V}$	Nanogenerator	[191]
9	PVDF	Ag-RGO	Solvent casting	$V_o = 18 \text{ V}$ , $I_S = 1050 \text{ nA}$	Nanogenerator	[192]
10	PDMS	NN	Hydrothermal/spin coating	$V_o = 3.2 \text{ V}$ , $I_S = 72 \text{ nA}$	Nanogenerator	[193]
11	PVDF	LiTaO <sub>3</sub>	Solid state/solvent casting	$V_o = 18 \text{ V}$ , $I_S = 1200 \text{ nA}$ , $P = 25 \text{ mW m}^{-2}$	Nanogenerator	[194]
12	PDMS	BT	Electrospinning	$V_o = 2.67 \text{ V}$ , $I_S = 261.4 \text{ nA}$ , $P = 0.184 \text{ } \mu\text{W}$	Nanogenerator	[195]
13	PDMS	Mn-KNN	Electrospinning	$V_o = 0.3 \text{ V}$ , $I_S = 50 \text{ nA}$	Nanogenerator	[196]
14	PVDF	ZnO	Solvothermal/electrospinning	$V_o = 85 \text{ V}$ , $I_S = 2200 \text{ nA}$	Nanogenerator	[197]
15	PVDF-TrFE	BT@C	Solution blending	$V_o = 17 \text{ V}$ , $P = 14.3 \text{ } \mu\text{W}$	Nanogenerator	[198]
16	PVDF	Tb-BCZT	Electrospinning	$V_o = 48.5 \text{ V}$ , $I_S = 3350 \text{ nA}$	Microenergy Harvester	[199]
17	PVC	ZnSnO <sub>3</sub>	Solution casting	$V_o = 40 \text{ V}$ , $I_S = 1400 \text{ nA}$	Power source for portable electronic device	[200]
18	PDMS	Li-ZnO	Hydrothermal/spin coating	$V_o = 180 \text{ V}$ , $I_S = 50 \text{ } \mu\text{A}$	Nanogenerator	[201]
19	PDMS	BT	Molten salt/solution Casting	$V_o = 126.3 \text{ V}$ , $P = 7 \text{ mW cm}^{-2}$		[163]
20	PDMS	2D-BT	Hydrothermal	$V_o = 13 \text{ V}$ , $I_S = 200 \text{ nA}$	Nanogenerator	[202]
21	PDMS	PANI-ZnS	Hydrothermal/solvent casting	$V_o = 35 \text{ V}$ , $P = 2.43 \text{ } \mu\text{W cm}^{-3}$	Power source for portable electronic device	[203]
22	PVDF	BT-BF	Electrospinning	$V_o = 83 \text{ V}$ , $I_S = 1.62 \text{ } \mu\text{A}$ , $P = 142 \text{ mW m}^{-2}$	Source for fast-charging supercapacitor	[204]
23	PDMS	ZnSnO <sub>3</sub>	Hydrothermal/solvent casting	$V_o = 20 \text{ V}$ , $I_S = 0.6 \text{ } \mu\text{A}$	Energy Harvesting	[205]
24	PVDF	KNN/ZnO	Electrospinning	$V_o = 25 \text{ V}$ , $I_S = 1.81 \text{ } \mu\text{A}$	Energy Harvesting	[206]
25	Flexible cellulose nanofibril	MoS <sub>2</sub>	Solvent casting	$V_o = 4.1 \text{ V}$ , $I_S = 0.21 \text{ } \mu\text{A}$	Energy Harvesting	[207]
26	PMMA	BT	Hydrothermal/electrospinning	$V_o = 12.6 \text{ V}$ , $I_S = 1.3 \text{ } \mu\text{A}$	Nanogenerator	[208]
27	PVDF-TrFE	KNNS-BZ-BKZ	Combustion synthesis/electrospinning	$V_o = 12.2 \text{ V}$ , $P = 33.2 \text{ nW}$	Nanogenerator	[209]
28	PDMS	Zn <sub>2</sub> SiO <sub>4</sub> /Graphene sheet	Hydrothermal	$V_o = 10 \text{ V}$ , $J = 50 \text{ nA/cm}^2$	Transparent flexible nanogenerator	[210]

Table 3 continued

Sr. No	Polymer matrix	Filler	Synthesis techniques	Performance	Application	Reference
29	PVDF-TrFE	BNNT	Solution casting	$V_o = 22 \text{ V}$ , $P = 11.3 \text{ } \mu\text{W}/\text{cm}^2$	Radiation protection in space and energy harvesting	[211]
30	PVDF-HFP	BTO	Spin coating	$V_o = 75 \text{ V}$ , $I_S = 15 \text{ } \mu\text{A}$	Nanogenerator	[212]
31	PDMS	BNNT-ZnO QD	Casting	$d_{33} = -60.3 \text{ pC/N}$	Nanogenerator	[213]
32	PVDF	MoS <sub>2</sub>	Casting	$V_o = 47 \text{ V}$ , $I_S = 0.12 \text{ } \mu\text{A}$	Photovoltaically self-charging power cell	[214]
33	PVDF	ZnO-rGO	Electrospinning	$E = 487 \text{ nJ}$ $P = 138 \text{ } \mu\text{W}/\text{cm}^3$	Self-powered cardiac pacemaker	[215]
34	Thermoplastic triblock copolymer grafted with maleic anhydride	PZT-NH <sub>2</sub>	Drop casting	$V_o = 65 \text{ V}$ , $I_S = 1.6 \text{ } \mu\text{A}$	Nanogenerator	[216]
35	PVDF-HFP	BT	Solvent evaporation	$V_o = 110 \text{ V}$ , $I_S = 22 \text{ } \mu\text{A}$ , $P = 0.48 \text{ } \mu\text{W}/\text{cm}^3$	Nanogenerator	[217]
36	PVDF	Pt nanoparticle	Electrospinning	$V_o = 30 \text{ V}$ , $I_S = 6 \text{ mA}/\text{cm}^2$ , $P = 22 \text{ } \mu\text{W}/\text{cm}^2$	Wearable nano-tactile sensor	[218]
37	PVDF	SnO <sub>2</sub> nanosheets	Solution casting	$V_o = 42 \text{ V}$ , $I_S = 0.0062 \text{ mA}/\text{cm}^2$ , $P = 4900 \text{ W}/\text{cm}^3$	Self-cleaning energy harvester	[219]
38	PVDF	Ce-Graphene	Electrospinning	$V_o = 11 \text{ V}$ , $I_S = 0.07 \text{ } \mu\text{A}$ , $P = 0.56 \text{ } \mu\text{W}/\text{cm}^2$	Nanopressure sensor and ultrasensitive acoustic nanogenerator	[220]
39	PVDF	Graphene-Ag	Solution casting	$V_o = 0.1 \text{ V}$ , $I_S = 0.1 \text{ nA}$ ,	Self-powered optical sensor	[221]
40	PDMS	BiFeO <sub>3</sub>	Spin casting	$V_o = 3 \text{ V}$ , $I_S = 250 \text{ nA}$	Energy harvester	[222]
41	PDMS	BT	Spin casting	$V_o = 3.2 \text{ V}$ , $I_S = 350 \text{ nA}$	Nanogenerator	[223]
42	PDMS	KNLN and Cu rods	Spin coating	$V_o = 12 \text{ V}$ , $I_S = 1.2 \text{ } \mu\text{A}$	Nanogenerator	[224]
43	PDMS	ZnO NP and MWCNT	Mechanical mixing	$V_o = 7.5 \text{ V}$ , $I_S = 2.5 \text{ } \mu\text{A}$	Flexible nanogenerator	[225]
44	PDMS	PZT and CNT	Ball Milling and Stirring	$V_o = 100 \text{ V}$ , $I_S = 10 \text{ } \mu\text{A}$	Energy harvester	[226]
45	Cellulose	BT	Aqueous suspension casting	$V_o = 2.86 \text{ V}$ , $I_S = 0.262 \text{ } \mu\text{A}$	Nanocomposite	[227]
46	PVDF	PMN-PT/CNT	Magnetic stirring and heat treatment	$V_o = 4 \text{ V}$ , $I_S = 30 \text{ nA}$	Nanogenerator	[228]
47	PDMS	BT	Hydrothermal/casting	$V_o = 7 \text{ V}$ , $I_S = 360 \text{ nA}$	Generator	[229]
48	PDMS	PMN-PT	Mechanical mixing	$V_o = 7.8 \text{ V}$ , $I_S = 2290 \text{ nA}$	Nanocomposite	[230]
49	PDMS	ZnSnO <sub>3</sub>	Hydrothermal/curing	$V_o = 120 \text{ V}$ , $I_S = 13 \text{ } \mu\text{A}$ , $P = 230 \text{ } \mu\text{W}/\text{cm}^2$	Nanogenerator	[231]

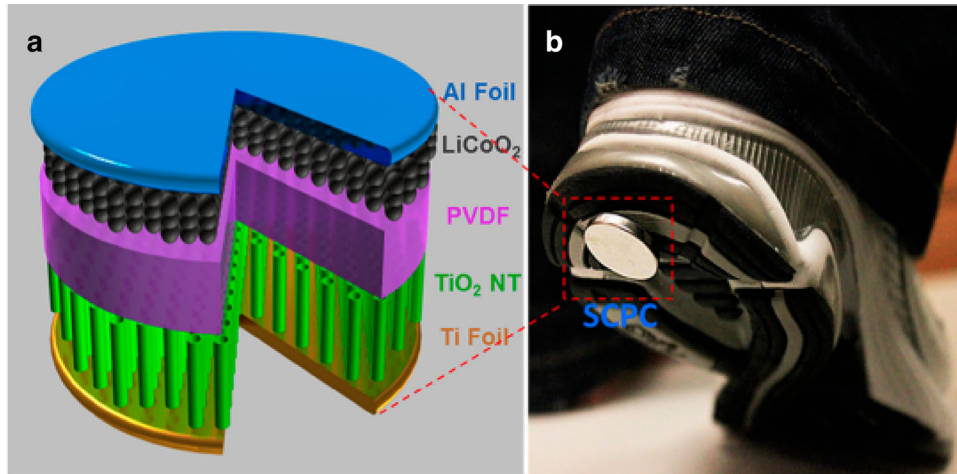
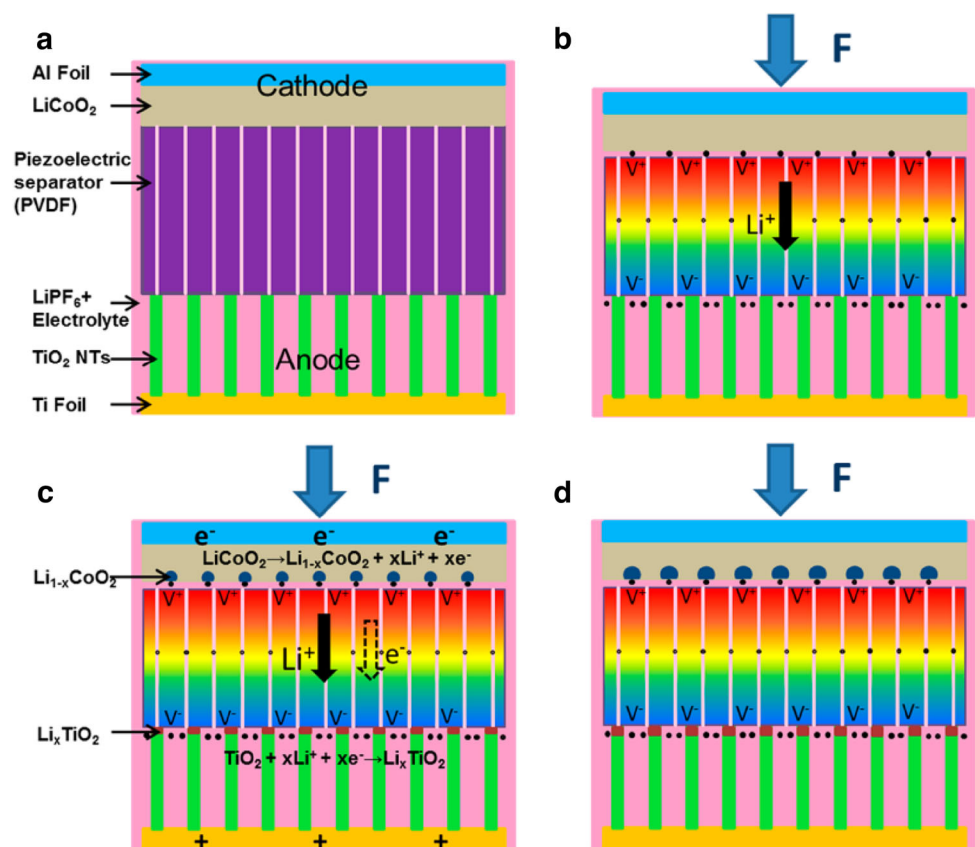


**Fig. 34** **a** Structure of the self-charging power cell having LiCoO<sub>2</sub> as a cathode and TiO<sub>2</sub> as an anode. PVDF film acts as a separator for the power cell **(b)** Complete power cell assembly is sealed inside the stainless-steel coin-shaped packaging and installed

below the shoe to harness the mechanical pressure energy while walking. Adapted/Re-used with authorization from citation [183]. Copyright 2012 American Chemical Society

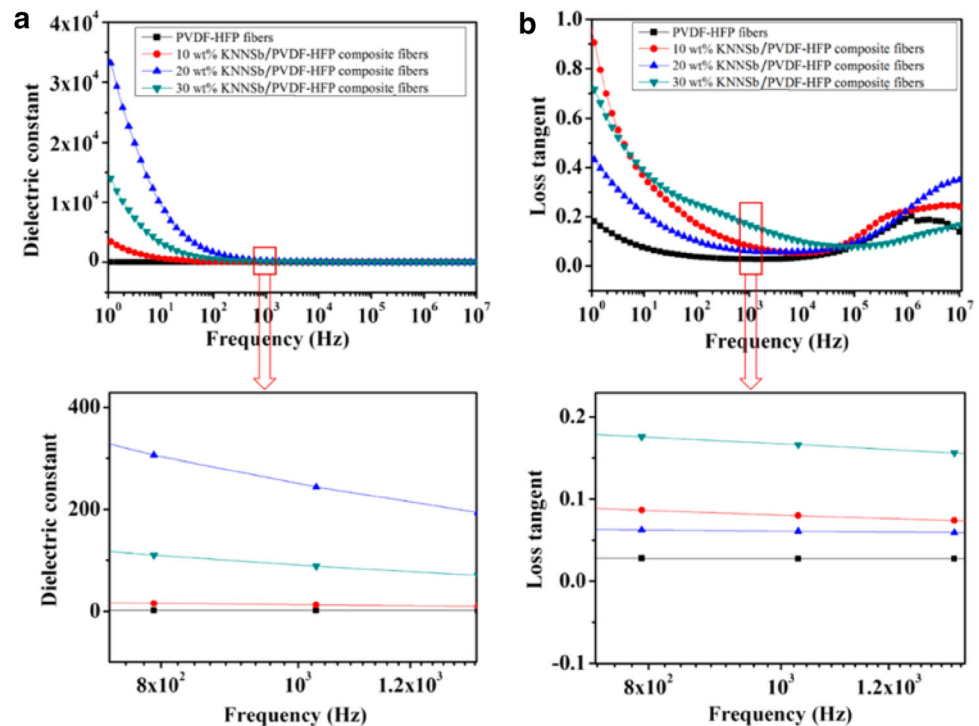
**Fig. 35** Working mechanism of self-charging power cell. **a** Power cell with TiO<sub>2</sub> as anode and LiCoO<sub>2</sub> as cathode; PVDF film is used as a separator with LiPF<sub>6</sub> as electrolyte **(b)** Upon application of pressure, PVDF causes piezo-potential with positive potential towards the cathode and negative towards anode **(c)** Under the piezo-potential, Li ions from cathode will travel towards anode through PVDF film, resulting in the cell charging reaction **(d)** Stage at which the chemical equilibrium between the two electrodes is established. Adapted/Re-used with authorization from citation [183]. Copyright 2012 American Chemical Society



Further, the authors performed the dielectric studies of pure PVDF-HFP and composite fibres at room temperature for the range of 1 Hz–1 MHz. At the low-frequency range (1 Hz–1 kHz), composites' dielectric constant increased drastically compared to

pristine PVDF-HFP due to the interfacial polarization that occurred on the surface of nanoparticles (Fig. 36). The emergence of interfacial polarization occurred due to the shape and size of the nano-additives and the drastic difference in the dielectric

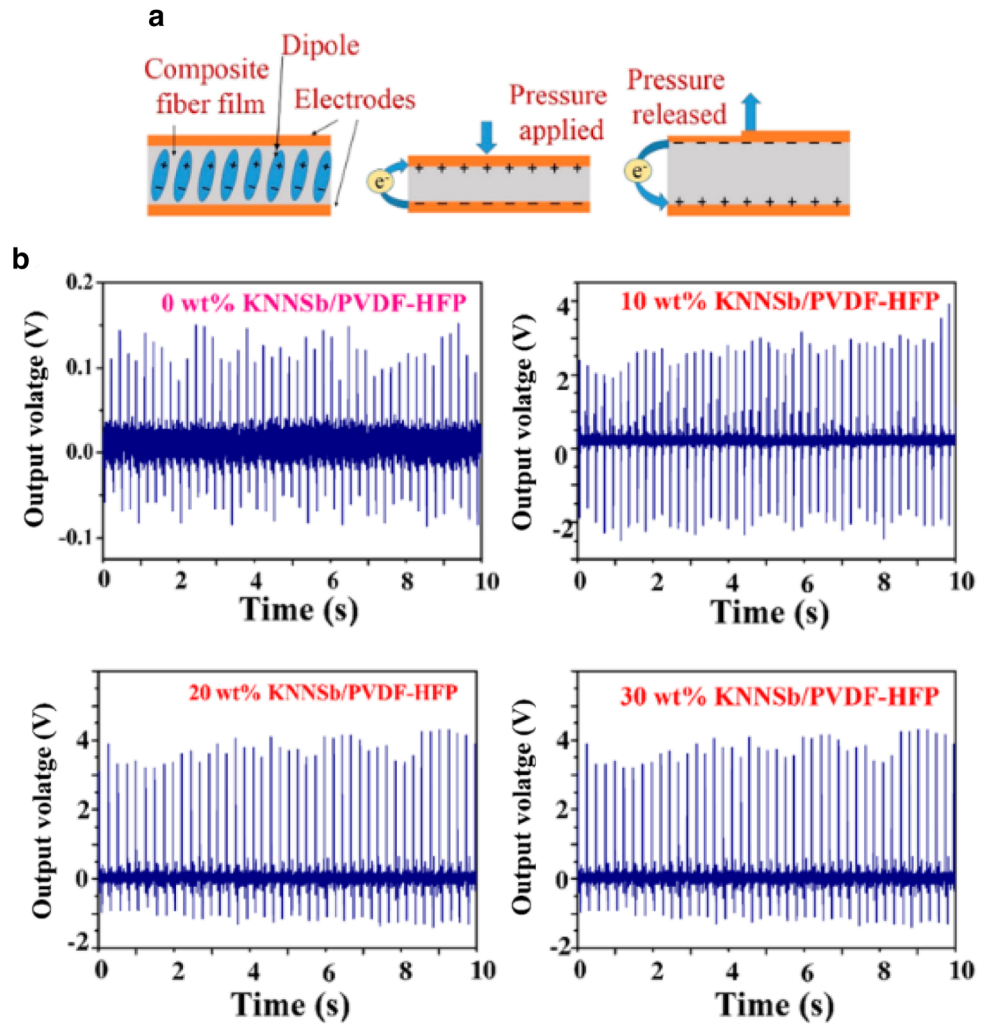
**Fig. 36** **a** Variation in dielectric constant with respect to frequency, **b** loss tangent for composites with different weight percentages of KNNSb dispersed in PVDF-HFP matrix. Adapted/Re-used with authorization from citation [71]. Copyright 2021 American Chemical Society



values of the ceramic and the polymer. Extensive reduction in size and wire-like shape of nanofibers with increased surface area facilitated the enhanced contribution from interfacial polarization. The same effect is also confirmed from the decreased value of loss tangent in the lower frequency region; however, at higher frequencies, a slight increase in the loss tangent is seen for the composites, attributed to the  $\alpha$ -relaxation of the PVDF-HFP polymer. Notably, the anomalous behaviour of the 30 wt% KNNSb/PVDF-HFP may have resulted from the non-uniform dispersion of nano-additives in the PVDF-HFP polymer matrix (Fig. 36). For the fabrication of the nanogenerator, 20 wt% KNNSb/PVDF-HFP nanofibers were selected because they showed higher ferroelectric values of ( $P_S$ : 0.992  $\mu\text{C}/\text{cm}^2$ ) as compared to pure PVDF-HFP nanofibers (0.510  $\mu\text{C}/\text{cm}^2$ ) and also exhibited a low value of tangent loss which is desirable. The energy harvesting functioning of the KNNSb/PVDF-HFP composite was measured with the help of periodic impulsive pressing on the nanogenerator, resulting in the nanogenerator's open-circuit voltage. When this periodic impulsive pressing causes alternating mechanical pressure variations on the nanogenerator, the outcome is the separation of the charged dipoles present and therefore causes a potential difference generation across

the material. The positive potential in the output window is appeared because of the transient flow of electrons, and the negative potential is due to the reverse flow of the electrons after the release of the pressure from the nanogenerator. The high value of output voltage of 4 V is observed for 10 wt% KNNSb composites, which is significant with respect to pure PVDF-HFP, whereas 4.9 V and 4.5 V values were observed for 20 wt% KNNSb and 30 wt% KNNSb, respectively, under cyclic pressure of 2 kPa (Fig. 37). The poling treatment and the addition of nanofillers in the PVDF-HFP are responsible for the increase in the percentage of  $\beta$ -phase of polymer, which resulted in this significant improvement in the output voltage in the composite. The short-circuit current observed for the 20 wt% KNNSb-based nanogenerator is 0.25  $\mu\text{A}$  with a current density of 0.014  $\mu\text{A}/\text{cm}^2$  across the load of 1 M $\Omega$ . The developed flexible nanogenerator is used as a temperature monitoring device in the heat pipe. The nanogenerator exhibited a  $V_{OC}$  of 0.1–0.3 mV from 20 to 80  $^\circ\text{C}$ , and then  $V_{OC}$  reached 6 mV from 80 to 100  $^\circ\text{C}$ . After 100  $^\circ\text{C}$ , it boosts to 150 mV because of the evaporation of the water. The nanogenerator showed sensitive behaviour to low variations in temperature and pressure; hence, it is possible to use it as a thermal controller in electronic devices.

**Fig. 37** **a** Mechanism of piezoelectric nanogenerator, **b** output voltages of different KNNSb and PVDF-HFP polymer. Adapted/Re-used with authorization from citation [71]. Copyright 2021 American Chemical Society



With so many advances in piezoelectric nanogenerators, it is possible to power micro-devices with the corresponding output. Although more emphasis is necessary on making them bio-friendly and increasing their current output to achieve power output in the range of mW. It is important to make currently available PENGs more durable, eco-friendly, and ready to use in real-life applications which can withstand problems such as intense heat or cold weather and external environmental factor for longer duration [97]. Further investigation is required to understand the dynamics of stacked alternate piezoelectric-electrode assembly which is novel tool to boost the current density. It is necessary to gain better understanding of the dynamics happening inside a self-charging power cell which is causing the conversion of mechanical energy directly into chemical energy.

Since the demand for portable and wearable microelectronic devices is increasing exponentially, they are currently trending in research community as well. As a self-sustainable energy source, piezoelectric nanogenerators are expected to be eco-friendly, biocompatible, flexible, lightweight, have high power output, and long service life.

## 4 Conclusion

Piezoelectric materials are multifunctional in nature and hold the potential for nanogenerator applications. In this review, a brief discussion and exploration of the ongoing advances in piezoelectric research in ceramics, polymers, and composites was performed. In addition, for achieving self-sustainable flexible devices, piezoelectric nanogenerators are also deliberated as potential future substitute for existing

conventional energy sources. Since many new lead-free piezoceramics are coming into the market with performance comparable to PZTs, it is plausible to make piezoelectric nanogenerator environmentally friendly in near future for a better tomorrow.

## Acknowledgements

The authors would like to thank Dr. C. P. Ramnarayanan, Vice-Chancellor, DIAT (DU), Pune, for his support.

## Author contributions

All authors contributed in the given study.

## Funding

The authors declare that no funds, grants, or other support were received during the preparation of this manuscript.

## Data availability

The authors declare that the data supporting the findings of this study are available within the article. No new data were created during the study.

## Declarations

**Conflict of interest** The authors have no relevant financial or non-financial interests to disclose.

## References

1. Y. Zhang, H. Kim, Q. Wang, W. Jo, A.I. Kingon, S.H. Kim, C.K. Jeong, *Nanoscale Adv.* **2**, 3131 (2020)
2. N. Sezer, M. Koç, *Nano Energy* **80**, 1 (2021)
3. P. Glynn-Jones, S.P. Beeby, N.M. White, *IEE Proc.* **148**, 68 (2001)
4. Z.L. Wang, J. Song, *Science* **312**, 242 (2006)
5. N. Sezer, M. Koç, *Nano Energy* **80**, 105567 (2021)
6. H. Liu, J. Zhong, C. Lee, S.-W. Lee, L. Lin, *Appl. Phys. Rev.* **5**, 041306 (2018)
7. M. Safaei, H.A. Sodano, S.R. Anton, *Smart Mater. Struct.* **28**, 62 (2019)
8. R.A. Surmenev, T. Orlova, R.V. Chernozem, A.A. Ivanova, A. Bartasyte, S. Mathur, M.A. Surmeneva, *Nano Energy* **62**, 475 (2019)
9. V. Buscaglia, C.A. Randall, *J. Eur. Ceram. Soc.* **40**, 3744 (2020)
10. P. Pascariu, M. Homocianu, *Ceram. Int.* **45**, 11158 (2019)
11. S. Mishra, L. Unnikrishnan, S.K. Nayak, S. Mohanty, *Macromol. Mater. Eng.* **304**, 1800463 (2019)
12. L. Lu, W. Ding, J. Liu, B. Yang, *Nano Energy* **78**, 105251 (2020)
13. R.A. Surmenev, R.V. Chernozem, I.O. Pariy, M.A. Surmeneva, *Nano Energy* **79**, 105442 (2021)
14. Y. Hu, C. Xu, Y. Zhang, L. Lin, R.L. Snyder, Z.L. Wang, *Adv. Mater.* **23**, 4068 (2011)
15. Z. Wang, X. Pan, Y. He, Y. Hu, H. Gu, Y. Wang, *Adv. Mater. Sci. Eng.* **2015**, 165631 (2015)
16. J. Hao, W. Li, J. Zhai, H. Chen, *Mater. Sci. Eng. R Reports* **135**, 1 (2019)
17. A.R. Chowdhury, J. Jaksik, I. Hussain, R. Longoria, O. Faruque, F. Cesano, D. Scarano, J. Parsons, M.J. Uddin, *Nano-Structures and Nano-Objects* **17**, 148 (2019)
18. B. Rawal, P. Dixit, N.N. Wathore, B. Praveenkumar, H.S. Panda, *Bull. Mater. Sci.* **43**, 82 (2020)
19. B. Rawal, P. Dixit, B. Praveenkumar, H.S. Panda, *J. Aust. Ceram. Soc.* **55**, 729 (2019)
20. X.-Q. Fang, J.-X. Liu, V. Gupta, *Nanoscale* **5**, 1716 (2013)
21. B. Jaffe, R.S. Roth, S. Marzullo, *J. Appl. Phys.* **25**, 809 (1954)
22. S. Das Mahapatra, P.C. Mohapatra, A.I. Aria, G. Christie, Y.K. Mishra, S. Hofmann, V.K. Thakur, *Adv. Sci.* **8**, 210086 (2021)
23. M.R. Soares, A.M.R. Senos, P.Q. Mantas, *J. Eur. Ceram. Soc.* **20**, 321 (2000)
24. S.B. Seshadri, M.M. Nolan, G. Tutuncu, J.S. Forrester, E. Sapper, G. Esteves, T. Granzow, P.A. Thomas, J.C. Nino, T. Rojac, J.L. Jones, *Sci. Rep.* **8**, 4120 (2018)
25. S.-E. Park, T.R. Shrout, *J. Appl. Phys.* **82**, 1804 (1997)
26. M.J. Hoffmann, H. Kungl, *Curr. Opin. Solid State Mater. Sci.* **8**, 51 (2004)
27. T. Leist, T. Granzow, W. Jo, J. Rödel, *J. Appl. Phys.* **108**, 014103 (2010)
28. L. Wang, C. Mao, G. Wang, G. Du, R. Liang, X. Dong, *J. Am. Ceram. Soc.* **96**, 24 (2013)
29. N. Luo, Q. Li, Z. Xia, X. Chu, *J. Am. Ceram. Soc.* **95**, 3246 (2012)
30. L.L. Wei, A.Y. Liu, C.C. Jin, F.T. Lin, P. Wang, Q.R. Yao, C.Y. Tian, Y. Li, J. Tang, H.L. Han, W.Z. Shi, C.B. Jing, *J. Alloys Compd.* **590**, 368 (2014)
31. S. Shahab, S. Zhao, A. Erturk, *Energy Technol.* **6**, 935 (2018)



32. T. Tani, J. Li, D. Viehland, D.A. Payne, *J. Appl. Phys.* **75**, 3017 (1994)
33. J. Li, D.D. Viehland, T. Tani, C.D.E. Lakeman, D.A. Payne, *J. Appl. Phys.* **75**, 442 (1994)
34. B.P. Pokharel, D. Pandey, *J. Appl. Phys.* **86**, 3327 (1999)
35. Q. Zhang, T. Yang, Y. Zhang, X. Yao, *J. Appl. Phys.* **113**, 244103 (2013)
36. X. Hao, J. Zhai, L.B. Kong, Z. Xu, *Prog. Mater. Sci.* **63**, 1 (2014)
37. G. Tan, K. Maruyama, Y. Kanamitsu, S. Nishioka, T. Ozaki, T. Umegaki, H. Hida, I. Kanno, *Sci. Rep.* **9**, 7309 (2019)
38. Y. Saito, H. Takao, T. Tani, T. Nonoyama, K. Takatori, T. Homma, T. Nagaya, M. Nakamura, *Nature* **432**, 84 (2004)
39. P. Kumar, M. Pattanaik, S. Sonia, *Ceram. Int.* **39**, 65 (2013)
40. H. Ishii, H. Nagata, T. Takenaka, *Jpn. J. Appl. Phys.* **40**, 5660 (2001)
41. A.D. Moriana, S. Zhang, *J. Mater.* **4**, 277 (2018)
42. J.-F. Li, K. Wang, F.-Y. Zhu, L.-Q. Cheng, F.-Z. Yao, *J. Am. Ceram. Soc.* **96**, 3677 (2013)
43. L. Egerton, D.M. Dillon, *J. Am. Ceram. Soc.* **42**, 438 (1959)
44. J. Wu, D. Xiao, J. Zhu, *Chem. Rev.* **115**, 2559 (2015)
45. R. Zuo, J. Fu, D. Lv, Y. Liu, *J. Am. Ceram. Soc.* **93**, 2783 (2010)
46. K. Wang, J.-F. Li, N. Liu, *Appl. Phys. Lett.* **93**, 092904 (2008)
47. J. Du, X.-J. Yi, Z.-J. Xu, C.-L. Ban, D.-F. Zhang, P.-P. Zhao, C.-M. Wang, *J. Alloys Compd.* **541**, 454 (2012)
48. F.-Z. Yao, K. Wang, Y. Shen, J.-F. Li, *J. Appl. Phys.* **118**, 134102 (2015)
49. W. Liang, W. Wu, D. Xiao, J. Zhu, J. Wu, *J. Mater. Sci.* **46**, 6871 (2011)
50. Y. Wang, D. Damjanovic, N. Klein, E. Hollenstein, N. Setter, *J. Am. Ceram. Soc.* **90**, 3485 (2007)
51. B. Rawal, N.N. Wathore, B. Praveenkumar, H.S. Panda, *J. Adv. Ceram.* **8**, 79 (2019)
52. X. Gao, Z. Cheng, Z. Chen, Y. Liu, X. Meng, X. Zhang, J. Wang, Q. Guo, B. Li, H. Sun, Q. Gu, H. Hao, Q. Shen, J. Wu, X. Liao, S.P. Ringer, H. Liu, L. Zhang, W. Chen, F. Li, S. Zhang, *Nat. Commun.* **12**, 881 (2021)
53. S. Wada, K. Yako, H. Kakemoto, T. Tsurumi, T. Kiguchi, *J. Appl. Phys.* **98**, 014109 (2005)
54. J. Gao, Y. Hao, S. Ren, T. Kimoto, M. Fang, H. Li, Y. Wang, L. Zhong, S. Li, X. Ren, *J. Appl. Phys.* **117**, 084106 (2015)
55. Y. Huan, X. Wang, J. Koruza, K. Wang, K.G. Webber, Y. Hao, L. Li, *Sci. Rep.* **6**, 22053 (2016)
56. D. Lin, K.W. Kwok, H. Wong Lai-wa Chan, *J. Am. Ceram. Soc.* **92**, 1362 (2009)
57. P. Dixit, S. Seth, B. Rawal, B.P. Kumar, H.S. Panda, *J. Mater. Sci. Mater. Electron.* **32**, 5393 (2021)
58. J.-S. Lee, K.-N. Pham, H.-S. Han, H.-B. Lee, V.D.N. Tran, *J. Korean Phys. Soc.* **60**, 212 (2012)
59. J. Hao, Z. Xu, R. Chu, W. Li, J. Du, G. Li, *J. Phys. D: Appl. Phys.* **48**, 472001 (2015)
60. S.-T. Zhang, A.B. Kouna, E. Aulbach, W. Jo, T. Granzow, H. Ehrenberg, J. Rödel, *J. Appl. Phys.* **103**, 034108 (2008)
61. T.H. Dinh, M.R. Bafandeh, J.-K. Kang, C.-H. Hong, W. Jo, J.-S. Lee, *Ceram. Int.* **41**, S458 (2015)
62. J.T. Zeng, K.W. Kwok, W.K. Tam, H.Y. Tian, X.P. Jiang, H.L.W. Chan, *J. Am. Ceram. Soc.* **89**, 3850 (2006)
63. C. Ye, J. Hao, B. Shen, J. Zhai, *J. Am. Ceram. Soc.* **95**, 3577 (2012)
64. J. Hao, B. Shen, J. Zhai, C. Liu, X. Li, X. Gao, *J. Appl. Phys.* **113**, 114106 (2013)
65. D.F.K. Hennings, C. Metzmacher, B.S. Schreinemacher, *J. Am. Ceram. Soc.* **84**, 179 (2001)
66. W. Liu, X. Ren, *Phys. Rev. Lett.* **103**, 257602 (2009)
67. P. Bharathi, K.B.R. Varma, *J. Appl. Phys.* **116**, 164107 (2014)
68. J. Zhang, Y. Qin, Y. Gao, W. Yao, M. Zhao, *J. Am. Ceram. Soc.* **97**, 759 (2014)
69. K. Meng, W. Li, X.-G. Tang, Q.-X. Liu, Y.-P. Jiang, *ACS Appl. Electron. Mater.* **4**, 2109 (2022)
70. S. Banerjee, S. Bairagi, S. Wazed Ali, *Ceram. Int.* **47**, 16402 (2021)
71. K.S. Chary, A.K. Sharma, C.S. Kumbhar, A.G. Rao, C.D. Prasad, H.S. Panda, *Ind. Eng. Chem. Res.* **60**, 4290 (2021)
72. W. Zhai, Q. Lai, L. Chen, L. Zhu, Z.L. Wang, *ACS Appl. Electron. Mater.* **2**, 2369 (2020)
73. J. Gomes, J.S. Nunes, V. Sencadas, S. Lanceros-Mendez, *Smart Mater. Struct.* **19**, 065010 (2010)
74. H. Xu, Y. Bai, V. Bharti, Z.-Y. Cheng, *J. Appl. Polym. Sci.* **82**, 70–75 (2001)
75. A.J. Lovinger, *Science* **220**, 1115 (1983)
76. M. Aldas, G. Boiteux, G. Seytre, Z. Ghallab, *Dielectric Behaviour of BaTiO<sub>3</sub>/P (VDF-HFP) Composite Thin Films Prepared by Solvent Evaporation Method*. 2010 10th IEEE International Conference on Solid Dielectrics (2010), pp. 1–4
77. Y. Huan, Y. Liu, Y. Yang, Y. Wu, *J. Appl. Polym. Sci.* **104**, 858 (2007)
78. P. Frübing, A. Kremmer, R. Gerhard-Multhaupt, A. Spanoudaki, P. Pissis, *J. Chem. Phys.* **125**, 214701 (2006)
79. S. Rajala, T. Siponkoski, E. Sarlin, M. Mettänen, M. Vuoriluoto, A. Pammo, J. Juuti, O.J. Rojas, S. Franssila, S. Tuukkanen, *ACS Appl. Mater. Interfaces* **8**, 15607 (2016)
80. A. Khouaja, A. Koubaa, H. Ben Daly, *Ind. Crops Prod.* **171**, 113928 (2021)

81. M. Morimoto, Y. Koshiba, M. Misaki, K. Ishida, *Appl. Phys. Express* **8**, 101501 (2015)
82. R.G. Lorenzini, W.M. Kline, C.C. Wang, R. Ramprasad, G.A. Sotzing, *Polymer (Guildf)*. **54**, 3529 (2013)
83. C. Park, Z. Ounaies, K.E. Wise, J.S. Harrison, *Polymer (Guildf)*. **45**, 5417 (2004)
84. B.H. Moghadam, M. Hasanzadeh, A. Simchi, *ACS Appl. Nano Mater.* **3**, 8742 (2020)
85. Y. Xin, X. Qi, C. Qian, H. Tian, Z. Ling, Z. Jiang, *Integr. Ferroelectr.* **158**, 43 (2014)
86. Y.R. Wang, J.M. Zheng, G.Y. Ren, P.H. Zhang, C. Xu, *Smart Mater. Struct.* **20**, 045009 (2011)
87. S.-H. Park, H.B. Lee, S.M. Yeon, J. Park, N.K. Lee, *ACS Appl. Mater. Interfaces* **8**, 24773 (2016)
88. I. Chinya, A. Pal, S. Sen, *J. Alloys Compd.* **722**, 829 (2017)
89. Y. Tajitsu, *IEEE Trans. Ultrason. Ferroelectr. Freq. Control* **60**, 1625 (2013)
90. N. Sriplai, R. Mangayil, A. Pammo, V. Santala, S. Tuukkanen, S. Pinitsoontorn, *Carbohydr. Polym.* **231**, 115730 (2020)
91. Y. Takase, J.W. Lee, J.I. Scheinbeim, B.A. Newman, *Macromolecules* **24**, 6644 (1991)
92. Y. Huang, G. Rui, Q. Li, E. Allahyarov, R. Li, M. Fukuto, G.J. Zhong, J.Z. Xu, Z.M. Li, P.L. Taylor, L. Zhu, *Nat. Commun.* **12**, 1 (2021)
93. Y. Song, Z. Shi, G.-H. Hu, C. Xiong, A. Isogai, Q. Yang, *J. Mater. Chem. A* **9**, 1910 (2021)
94. N.A. Shepelin, P.C. Sherrell, E.N. Skountzos, E. Goudeli, J. Zhang, V.C. Lussini, B. Imtiaz, K.A.S. Usman, G.W. Dicinowski, J.G. Shapter, J.M. Razal, A.V. Ellis, *Nat. Commun.* **12**, 1 (2021)
95. G. Kaur, J.S. Meena, M. Jassal, A.K. Agrawal, *ACS Appl. Polym. Mater.* **4**, 4751 (2022)
96. P. Eltouby, I. Shyha, C. Li, J. Khaliq, *Ceram. Int.* **47**, 17813 (2021)
97. C. Zhang, W. Fan, S. Wang, Q. Wang, Y. Zhang, K. Dong, *ACS Appl. Electron. Mater.* **3**, 2449 (2021)
98. H. Parangusan, D. Ponnamma, M. Al Ali Almaadeed, *RSC Adv.* **7**, 50156 (2017)
99. K.S. Chary, H.S. Panda, C.D. Prasad, *Ind. Eng. Chem. Res.* **56**, 10335 (2017)
100. E.J. Mele, P. Král, *Phys. Rev. Lett.* **88**, 056803 (2002)
101. H. Kuang, Y. Li, S. Huang, L. Shi, Z. Zhou, C. Gao, X. Zeng, R. Pandey, X. Wang, S. Dong, X. Chen, J. Yang, H. Yang, J. Luo, *Nano Energy* **80**, 105561 (2021)
102. J.H. Kang, G. Sauti, C. Park, V.I. Yamakov, K.E. Wise, S.E. Lowther, C.C. Fay, S.A. Thibeault, R.G. Bryant, *ACS Nano* **9**, 11942 (2015)
103. W. Choi, J. Kim, E. Lee, G. Mehta, V. Prasad, *ACS Appl. Mater. Interfaces* **13**, 13596 (2021)
104. W. Wu, L. Wang, Y. Li, F. Zhang, L. Lin, S. Niu, D. Chenet, X. Zhang, Y. Hao, T.F. Heinz, J. Hone, Z.L. Wang, *Nature* **514**, 470 (2014)
105. H. Zhu, Y. Wang, J. Xiao, M. Liu, S. Xiong, Z.J. Wong, Z. Ye, Y. Ye, X. Yin, X. Zhang, *Nat. Nanotechnol.* **10**, 151 (2015)
106. K. Nakamura, *Sensors Mater.* **30**, 2073 (2018)
107. V. Bhavanasi, V. Kumar, K. Parida, J. Wang, P.S. Lee, *ACS Appl. Mater. Interfaces* **8**, 521 (2016)
108. Y.-X. Zhou, Y.-T. Lin, S.-M. Huang, G.-T. Chen, S.-W. Chen, H.-S. Wu, I.-C. Ni, W.-P. Pan, M.-L. Tsai, C.-I. Wu, P.-K. Yang, *Nano Energy* **97**, 107172 (2022)
109. S. Wang, H.-Q. Shao, Y. Liu, C.-Y. Tang, X. Zhao, K. Ke, R.-Y. Bao, M.-B. Yang, W. Yang, *Compos. Sci. Technol.* **202**, 108600 (2021)
110. S. Veeralingam, D.K. Bharti, S. Badhulika, *Mater. Res. Bull.* **151**, 111815 (2022)
111. M.S. Mirza, Q. Liu, T. Yasin, X. Qi, J.-F. Li, M. Ikram, *Ceram. Int.* **42**, 10745 (2016)
112. S. Bodkhe, G. Turcot, F.P. Gosselin, D. Therriault, *ACS Appl. Mater. Interfaces* **9**, 20833 (2017)
113. J. Zhang, S. Ye, H. Liu, X. Chen, X. Chen, B. Li, W. Tang, Q. Meng, P. Ding, H. Tian, X. Li, Y. Zhang, P. Xu, J. Shao, *Nano Energy* **77**, 105300 (2020)
114. X. Zhang, M.Q. Le, O. Zahhaf, J.F. Capsal, P.J. Cottinet, L. Petit, *Mater. Des.* **192**, 108783 (2020)
115. L.J. Bowen, R.L. Gentilman, H.T. Pham, D.F. Fiore, K.W. French, *Proc. IEEE Ultrason. Symp.* **1**, 499–503 (1993)
116. T. Lusiola, A. Soppelsa, F. Rubio-Marcos, J.F. Fernandez, F. Clemens, *J. Eur. Ceram. Soc.* **36**, 2745 (2016)
117. Y. Zhen, Z. Cen, L. Chen, P. Zhao, X. Wang, L. Li, *J. Alloys Compd.* **752**, 206 (2018)
118. H.S. Shulman, M. Testorf, D. Damjanovic, N. Setter, *J. Am. Ceram. Soc.* **79**, 3124 (1996)
119. R. Zhang, Y. Wang, K. Wang, G. Zheng, Q. Li, C. Shen, *Polym. Bull.* **70**, 195 (2013)
120. S. Abdalla, A. Obaid, F.M. Al-Marzouki, *Results Phys.* **6**, 617 (2016)
121. S. Bodkhe, P.S.M. Rajesh, S. Kamle, V. Verma, *J. Polym. Res.* **21**, 434 (2014)
122. K.-B. Kim, D.K. Hsu, B. Ahn, Y.-G. Kim, D.J. Barnard, *Ultrasonics* **50**, 790 (2010)
123. A. Thakre, S. Lee, D.R. Patil, M. Peddigari, G.-T. Hwang, J. Ryu, *J. Asian Ceram. Soc.* **9**, 1290 (2021)
124. C. Guo, L. Zhou, J. Lv, *Polym. Polym. Compos.* **21**, 449 (2013)
125. H. Shen, J. Guo, H. Wang, N. Zhao, J. Xu, *ACS Appl. Mater. Interfaces* **7**, 5701 (2015)
126. X. Zeng, L. Ye, S. Yu, H. Li, R. Sun, J. Xu, C.-P. Wong, *Nanoscale* **7**, 6774 (2015)

127. H. Hong, J. Kim, T. Kim, *Polymers (Basel)* **9**, 413 (2017)
128. H.A. Pohl, *J. Appl. Phys.* **22**, 869 (1951)
129. M. Xie, Y. Zhang, M.J. Krašny, C. Bowen, H. Khanbareh, N. Gathercole, *Energy Environ. Sci.* **11**, 2919 (2018)
130. S.-H. Shin, S.-Y. Choi, M.H. Lee, J. Nah, *ACS Appl. Mater. Interfaces* **9**, 41099 (2017)
131. X. Meng, W. Wang, H. Ke, J. Rao, D. Jia, Y. Zhou, *J. Mater. Chem. C* **5**, 747 (2017)
132. C. Piskin, L. Karacasulu, M. Bortolotti, C. Vakifahmetoglu, *Open Ceram.* **7**, 100159 (2021)
133. T.J. Bukowski, K. McCarthy, F. McCarthy, G. Teowee, T.P. Alexander, D.R. Uhlmann, J.T. Dawley, B.J.J. Zelinski, *Integr. Ferroelectr.* **17**, 339 (1997)
134. K. Batra, N. Sinha, S. Goel, H. Yadav, A.J. Joseph, B. Kumar, *J. Alloys Compd.* **767**, 1003 (2018)
135. N.A. Spaldin, *Phys. Rev. B* **69**, 125201 (2004)
136. C. Ang, Z. Yu, Z. Jing, R. Guo, A.S. Bhalla, L.E. Cross, *Appl. Phys. Lett.* **80**, 3424 (2002)
137. B. Gao, Z. Yao, D. Lai, Q. Guo, W. Pan, H. Hao, M. Cao, H. Liu, *J. Alloys Compd.* **836**, 155474 (2020)
138. C. Zhao, B. Wu, K. Wang, J.-F. Li, D. Xiao, J. Zhu, J. Wu, *J. Mater. Chem. A* **6**, 23736 (2018)
139. Y.G. Lv, C.L. Wang, J.L. Zhang, L. Wu, M.L. Zhao, J.P. Xu, *Mater. Res. Bull.* **44**, 284 (2009)
140. A.J. Bell, *J. Mater. Sci.* **41**, 13 (2006)
141. L. Liu, W. Fu, L. Wang, H. Tian, X. Shan, *J. Alloys Compd.* **885**, 160829 (2021)
142. H. Zhang, Y. Zhu, L. Li, *RSC Adv.* **10**, 3391 (2020)
143. J. Fu, Y. Hou, M. Zheng, Q. Wei, M. Zhu, H. Yan, *ACS Appl. Mater. Interfaces* **7**, 24480 (2015)
144. K. Wang, J.-F. Li, *Adv. Funct. Mater.* **20**, 1924 (2010)
145. T. Yamada, T. Ueda, T. Kitayama, *J. Appl. Phys.* **53**, 4328 (1982)
146. J. Khaliq, D.B. Deutz, J.A.C. Frescas, P. Vollenberg, T. Hoeks, S. van der Zwaag, P. Groen, *Ceram. Int.* **43**, 2774 (2017)
147. R. Jayendiran, A. Arockiarajan, *J. Appl. Phys.* **112**, 044107 (2012)
148. P. Wang, Y. Li, Y. Lu, *J. Eur. Ceram. Soc.* **31**, 2005 (2011)
149. A. Yang, C.-A. Wang, R. Guo, Y. Huang, C.-W. Nan, *Ceram. Int.* **36**, 549 (2010)
150. J. Yoo, *Ferroelectrics* **507**, 12 (2017)
151. L. Zhao, B.-P. Zhang, P.-F. Zhou, L.-F. Zhu, J.-F. Li, *J. Eur. Ceram. Soc.* **35**, 533 (2015)
152. P. Mishra, Sonia, P. Kumar, *J. Alloys Compd.* **545**, 210 (2012)
153. J. Hao, W. Bai, W. Li, J. Zhai, *J. Am. Ceram. Soc.* **95**, 1998 (2012)
154. J.-H. Ahn, J.-H. Koh, *J. Alloys Compd.* **689**, 138 (2016)
155. H. Wan, C. Luo, W.-Y. Chang, Y. Yamashita, X. Jiang, *Appl. Phys. Lett.* **114**, 172901 (2019)
156. F.-Z. Yao, K. Wang, W. Jo, J.-S. Lee, J.-F. Li, *J. Appl. Phys.* **116**, 114102 (2014)
157. J. Hafner, M. Teuschel, M. Schneider, U. Schmid, *Polymer (Guildf)*. **170**, 1 (2019)
158. J.D. Sherman, J. Elloian, J. Jadwiszczak, K.L. Shepard, *ACS Appl. Polym. Mater.* **2**, 5110 (2020)
159. J. Patadiya, A. Gawande, G. Joshi, B. Kandasubramanian, *Ind. Eng. Chem. Res.* **60**, 15885 (2021)
160. H. Kim, F. Torres, D. Villagran, C. Stewart, Y. Lin, T.L.B. Tseng, *Macromol. Mater. Eng.* **302**, 1 (2017)
161. D. Zhou, K.H. Lam, Y. Chen, Q. Zhang, Y.C. Chiu, H. Luo, J. Dai, H.L.W. Chan, *Sensors Actuators A Phys.* **182**, 95 (2012)
162. H. Lee, S. Zhang, Y. Bar-Cohen, S. Sherrit, *Sensors* **14**, 14526 (2014)
163. N.R. Alluri, A. Chandrasekhar, V. Vivekananthan, Y. Purusothaman, S. Selvarajan, J.H. Jeong, S.-J. Kim, *ACS Sustain. Chem. Eng.* **5**, 4730 (2017)
164. J. Li, F. Yang, Y. Long, Y. Dong, Y. Wang, X. Wang, *ACS Nano* **15**, 14903 (2021)
165. L. Gu, J. Liu, N. Cui, Q. Xu, T. Du, L. Zhang, Z. Wang, C. Long, Y. Qin, *Nat. Commun.* **11**, 1030 (2020)
166. G. Cheng, Z.-H. Lin, L. Lin, Z. Du, Z.L. Wang, *ACS Nano* **7**, 7383 (2013)
167. D. Hu, M. Yao, Y. Fan, C. Ma, M. Fan, M. Liu, *Nano Energy* **55**, 288 (2019)
168. K.-I. Park, J.H. Son, G.-T. Hwang, C.K. Jeong, J. Ryu, M. Koo, I. Choi, S.H. Lee, M. Byun, Z.L. Wang, K.J. Lee, *Adv. Mater.* **26**, 2514 (2014)
169. V. Nguyen, R. Zhu, R. Yang, *Nano Energy* **14**, 49 (2015)
170. S. Chandrasekaran, C. Bowen, J. Roscow, Y. Zhang, D.K. Dang, E.J. Kim, R.D.K. Misra, L. Deng, J.S. Chung, S.H. Hur, *Phys. Rep.* **792**, 1 (2019)
171. M. Deterre, E. Lefevre, Y. Zhu, M. Woytasik, B. Boutaud, R.D. Molin, *J. Microelectromechanical Syst.* **23**, 651 (2014)
172. N.S. Shenck, J.A. Paradiso, *IEEE Micro* **21**, 30 (2001)
173. S. Khalifa, G. Lan, M. Hassan, A. Seneviratne, S.K. Das, *IEEE Trans. Mob. Comput.* **17**, 1353 (2018)
174. C. Sun, J. Shi, D.J. Bayerl, X. Wang, *Energy Environ. Sci.* **4**, 4508 (2011)
175. H. Xue, Q. Yang, D. Wang, W. Luo, W. Wang, M. Lin, D. Liang, Q. Luo, *Nano Energy* **38**, 147 (2017)
176. L. Yuan, W. Fan, X. Yang, S. Ge, C. Xia, S.Y. Foong, R.K. Liew, S. Wang, Q. Van Le, S.S. Lam, *Compos. Commun.* **25**, 100680 (2021)

177. W. Deng, T. Yang, L. Jin, C. Yan, H. Huang, X. Chu, Z. Wang, D. Xiong, G. Tian, Y. Gao, H. Zhang, W. Yang, *Nano Energy* **55**, 516 (2019)
178. D.Y. Park, D.J. Joe, D.H. Kim, H. Park, J.H. Han, C.K. Jeong, H. Park, J.G. Park, B. Joung, K.J. Lee, *Adv. Mater.* **29**, 1702308 (2017)
179. S.-I. Jeong, E.J. Lee, G.R. Hong, Y. Jo, S.M. Jung, S.Y. Lee, Y. Choi, S. Jeong, *ACS Omega* **5**, 1956 (2020)
180. Z. He, B. Gao, T. Li, J. Liao, B. Liu, X. Liu, C. Wang, Z. Feng, Z. Gu, *ACS Sustain. Chem. Eng.* **7**, 1745 (2019)
181. N.R. Alluri, B. Saravanakumar, S.-J. Kim, *ACS Appl. Mater. Interfaces* **7**, 9831 (2015)
182. Z.L. Wang, G. Zhu, Y. Yang, S. Wang, C. Pan, *Mater. Today* **15**, 532 (2012)
183. X. Xue, S. Wang, W. Guo, Y. Zhang, Z.L. Wang, *Nano Lett.* **12**, 5048 (2012)
184. A. Ramadoss, B. Saravanakumar, S.W. Lee, Y.-S. Kim, S.J. Kim, Z.L. Wang, *ACS Nano* **9**, 4337 (2015)
185. S. Badatya, A. Kumar, C. Sharma, A.K. Srivastava, J.P. Chaurasia, M.K. Gupta, *Mater. Lett.* **290**, 129493 (2021)
186. S.K. Karan, D. Mandal, B.B. Khatua, *Nanoscale* **7**, 10655 (2015)
187. H. Su, X. Wang, C. Li, Z. Wang, Y. Wu, J. Zhang, Y. Zhang, C. Zhao, J. Wu, H. Zheng, *Nano Energy* **83**, 105809 (2021)
188. I. Chinya, A. Sasmal, A. Pal, S. Sen, *CrystEngComm* **21**, 3478 (2019)
189. S. Bairagi, S.W. Ali, *Soft Matter* **16**, 4876 (2020)
190. H.H. Singh, S. Singh, N. Khare, *Compos. Sci. Technol.* **149**, 127 (2017)
191. D. Ponnamma, M.A.A. Al-Maadeed, *Sustain. Energy Fuels* **3**, 774 (2019)
192. M. Pusty, L. Sinha, P.M. Shirage, *New J. Chem.* **43**, 284 (2019)
193. J.H. Jung, M. Lee, J.-I. Hong, Y. Ding, C.-Y. Chen, L.-J. Chou, Z.L. Wang, *ACS Nano* **5**, 10041 (2011)
194. P. Manchi, S.A. Graham, H. Patnam, N.R. Alluri, S.-J. Kim, J.S. Yu, *ACS Appl. Mater. Interfaces* **13**, 46526 (2021)
195. J. Yan, Y.G. Jeong, *ACS Appl. Mater. Interfaces* **8**, 15700 (2016)
196. H.B. Kang, J. Chang, K. Koh, L. Lin, Y.S. Cho, *ACS Appl. Mater. Interfaces* **6**, 10576 (2014)
197. J. Li, S. Chen, W. Liu, R. Fu, S. Tu, Y. Zhao, L. Dong, B. Yan, Y. Gu, *J. Phys. Chem. C* **123**, 11378 (2019)
198. Z. Zhou, Z. Zhang, Q. Zhang, H. Yang, Y. Zhu, Y. Wang, L. Chen, *ACS Appl. Mater. Interfaces* **12**, 1567 (2020)
199. H. Lu, J. Zhang, L. Yang, Y. Zhang, Y. Wu, H. Zheng, *ACS Appl. Mater. Interfaces* **14**(10), 12243–12256 (2022)
200. S. Paria, S.K. Karan, R. Bera, A.K. Das, A. Maitra, B.B. Khatua, *Ind. Eng. Chem. Res.* **55**, 10671 (2016)
201. S.-H. Shin, Y.-H. Kim, M.H. Lee, J.-Y. Jung, J.H. Seol, J. Nah, *ACS Nano* **8**, 10844 (2014)
202. M. Yao, L. Li, Y. Wang, D. Yang, L. Miao, H. Wang, M. Liu, K. Ren, H. Fan, D. Hu, *ACS Sustain. Chem. Eng.* **10**(10), 3276–3287 (2022)
203. A. Sultana, M.M. Alam, S. Garain, T.K. Sinha, T.R. Midya, D. Mandal, *ACS Appl. Mater. Interfaces* **7**, 19091 (2015)
204. S.P. Muduli, S. Veeralingam, S. Badhulika, *ACS Appl. Energy Mater.* **5**(3), 2993–3003 (2022)
205. R. Guo, Y. Guo, H. Duan, H. Li, H. Liu, *ACS Appl. Mater. Interfaces* **9**, 8271 (2017)
206. S. Bairagi, S.W. Ali, *Int. J. Energy Res.* **44**, 5545 (2020)
207. T. Wu, Y. Song, Z. Shi, D. Liu, S. Chen, C. Xiong, Q. Yang, *Nano Energy* **80**, 105541 (2021)
208. K. Shi, B. Chai, H. Zou, P. Shen, B. Sun, P. Jiang, Z. Shi, X. Huang, *Nano Energy* **80**, 105515 (2021)
209. S.-R. Kim, J.-H. Yoo, J.H. Kim, Y.S. Cho, J.-W. Park, *Nano Energy* **79**, 105445 (2021)
210. D.K. Bharti, M.K. Gupta, R. Kumar, N. Sathish, A.K. Srivastava, *Nano Energy* **73**, 104821 (2020)
211. S. Ye, C. Cheng, X. Chen, X. Chen, J. Shao, J. Zhang, H. Hu, H. Tian, X. Li, L. Ma, W. Jia, *Nano Energy* **60**, 701 (2019)
212. S.-H. Shin, Y.-H. Kim, M.H. Lee, J.-Y. Jung, J. Nah, *ACS Nano* **8**, 2766 (2014)
213. J. Shim, D.I. Son, J.S. Lee, J. Lee, G.-H. Lim, H. Cho, E. Kim, S.D. Bu, S. IM, C.K. Jeong, S. Rezvani, S.S. Park, Y.J. Park, *Nano Energy* **93**, 106886 (2022)
214. S.S. Nardekar, K. Krishnamoorthy, P. Pazhamalai, S. Sahoo, S. Jae Kim, *Nano Energy* **93**, 106869 (2022)
215. S. Azimi, A. Golabchi, A. Nekookar, S. Rabbani, M.H. Amiri, K. Asadi, M.M. Abolhasani, *Nano Energy* **83**, 105781 (2021)
216. E.J. Lee, T.Y. Kim, S.-W. Kim, S. Jeong, Y. Choi, S.Y. Lee, *Energy Environ. Sci.* **11**, 1425 (2018)
217. S.-H. Shin, Y.-H. Kim, J.-Y. Jung, M. Hyung Lee, J. Nah, *Nanotechnology* **25**, 485401 (2014)
218. S.K. Ghosh, D. Mandal, *Nano Energy* **53**, 245 (2018)
219. E. Kar, N. Bose, B. Dutta, S. Banerjee, N. Mukherjee, S. Mukherjee, *Energy Convers. Manag.* **184**, 600 (2019)
220. S. Garain, S. Jana, T.K. Sinha, D. Mandal, *ACS Appl. Mater. Interfaces* **8**, 4532 (2016)
221. T.K. Sinha, S.K. Ghosh, R. Maiti, S. Jana, B. Adhikari, D. Mandal, S.K. Ray, *ACS Appl. Mater. Interfaces* **8**, 14986 (2016)
222. X. Ren, H. Fan, Y. Zhao, Z. Liu, *ACS Appl. Mater. Interfaces* **8**, 26190 (2016)

223. K.-I. Park, M. Lee, Y. Liu, S. Moon, G.-T. Hwang, G. Zhu, J.E. Kim, S.O. Kim, D.K. Kim, Z.L. Wang, K.J. Lee, *Adv. Mater.* **24**, 2999 (2012)
224. C.K. Jeong, K.-I. Park, J. Ryu, G.-T. Hwang, K.J. Lee, *Adv. Funct. Mater.* **24**, 2620 (2014)
225. H. Sun, H. Tian, Y. Yang, D. Xie, Y.-C. Zhang, X. Liu, S. Ma, H.-M. Zhao, T.-L. Ren, *Nanoscale* **5**, 6117 (2013)
226. K.-I. Park, C.K. Jeong, J. Ryu, G.-T. Hwang, K.J. Lee, *Adv. Energy Mater.* **3**, 1539 (2013)
227. H.Y. Choi, Y.G. Jeong, *Compos. Part B Eng.* **168**, 58 (2019)
228. S. Das, A.K. Biswal, K. Parida, R.N.P. Choudhary, A. Roy, *Appl. Surf. Sci.* **428**, 356 (2018)
229. K.-I. Park, S. Bin Bae, S.H. Yang, H.I. Lee, K. Lee, S.J. Lee, *Nanoscale* **6**, 8962 (2014)
230. S. Xu, Y. Yeh, G. Poirier, M.C. McAlpine, R.A. Register, N. Yao, *Nano Lett.* **13**, 2393 (2013)
231. A. Rovisco, A. dos Santos, T. Cramer, J. Martins, R. Branquinho, H. Águas, B. Fraboni, E. Fortunato, R. Martins, R. Igreja, P. Barquinha, *ACS Appl. Mater. Interfaces* **12**, 18421 (2020)
232. B. Wu, H. Wu, J. Wu, D. Xiao, J. Zhu, S.J. Pennycook, *J. Am. Chem. Soc.* **138**(47), 15459–15464 (2016)
233. H. Ouchi, K. Nagano, S. Hayakawa, *J. Am. Ceram. Soc.* **48**(12), 630–635 (1965)

**Publisher's Note** Springer Nature remains neutral with regard to jurisdictional claims in published maps and institutional affiliations.

Springer Nature or its licensor (e.g. a society or other partner) holds exclusive rights to this article under a publishing agreement with the author(s) or other rightsholder(s); author self-archiving of the accepted manuscript version of this article is solely governed by the terms of such publishing agreement and applicable law.